2012

Synthesis, characterization, and self-assembly of porphyrins conjugated to superparamagnetic colloidal particles for enhanced photodynamic therapy

Javoris Hollingsworth
Louisiana State University and Agricultural and Mechanical College, jholl15@lsu.edu

SYNTHESIS, CHARACTERIZATION, AND SELF-ASSEMBLY OF PORPHYRINS CONJUGATED TO SUPERPARAMAGNETIC COLLOIDAL PARTICLES FOR ENHANCED PHOTODYNAMIC THERAPY

A Dissertation

Submitted to the Graduate Faculty of the
Louisiana State University and
Agricultural and Mechanical College
in partial fulfillment of the
requirements for the degree of
Doctor of Philosophy

in

The Department of Chemistry

by
Javoris Hollingsworth
B.S., Georgia Southern University, May 2007
M.S., Louisiana State University, August 2009
December 2012

To my precious daughter

ACKNOWLEDGEMENTS

First and foremost, I would like to thank God for blessing and guiding my path in life. Truly, through Him, all my dreams and aspirations were made possible. Words cannot express my debt of gratitude.

I would like to thank my research advisers, Dr. Graça M. Vicentè and Dr. Paul S. Russo, (a.k.a, "Good Cop/Bad Cop", in no particular order) for all of their support, guidance, and constant encouragement throughout my graduate school career. I appreciate you both for allowing me to explore various research ideas, which attributed to my development as an independent scientist. This experience in working with you also taught me that there is always more than one way of critically thinking when problem-solving.

Thank you to Kim Mollere, Vickie Thornton, Sherry Wilkes, and Dr. Zakiya Wilson for all of their help with my transition to graduate life. I also would like to thank Dr. Sandra McGuire for providing the necessary study tactics Thanks to Mr. Roya Hughes for the occasional words of encouragement and laughs. Also, sincere thanks to Dr. Irina Nesterova, Dr. Allison J. Richard, Dr. Derek Dorman and Andrew Weber for providing training in the analytical techniques and methods that was essential for my success in this and future projects. Thanks to Mr. Mack Carswell, Dr. Rosalie Richards, Dr. Mark Morvant, and Dr. Karen Welch for sparking my interest in chemistry.

I thank my committee members, Dr. David Spivak, Dr. Doug Gilman, and Dr. Crystal Johnson for all of the time, patience and effort you invested in me and my graduate career. Also, special thanks to all of my research group colleagues and friends for their support. You guys really were like brothers and sisters to me.

Last, but not least, I thank my family for showing so much love and patience throughout this process. Specifically, to my mother, Sandra Hollingsworth, thank you for being a strong and providing woman. To my father, Garry Hollingsworth, Sr., thank you for instilling the values of hard-work, dedication, and perseverance within me at a young age. I know you're in heaven smiling down with joy as I continue to make you proud. Thanks to my grandmother, Geraldine Thomas, for her continuous support and believing in me. Finally, I want to say thank you to my loving and amazing wife, Dr. Arlene Gordon-Hollingsworth. You have no idea how much of an inspiration you've been to me. For each of you, I am forever grateful.

TABLE OF CONTENTS

LIST OF FIGURES

LIST OF SCHEMES

LIST OF ABBREVIATIONS AND SYMBOLS

AUC = Analytical Ultracentrifugation

DLS = Dynamic Light Scattering

DCM = Dichloromethane (CH_2Cl_2)

EM = Electron Microscopy

H_2TPPS = *Meso*-Tetrakis(4-Sulfonatophenyl) Porphyrin

MS = Mass spectroscopy

m/z = Mass to charge ratio

NMR = Nuclear Magnetic Resonance

PDT = Photodynamic Therapy

SAXS = Small Angle X-ray Scattering

SEC = Size Exclusion Chromatography

SE = Sedimentation Equilibrium

SV = Sedimentation Velocity

TFA = Trifluoroacetic acid

TLC = Thin Layer Chromatography

TMS = Tetramethylsilane

TPP = 5, 10, 15, 20-tetraphenylporphyrin

XPS = X-ray Photoelectron Spectroscocopy

XRD = X-ray Diffraction

ABSTRACT

Porphyrins and their derivatives are often used as photosensitizers in photodynamic therapy (PDT), which is a noninvasive antitumor treatment. The photochemical process for PDT involves exciting a photosensitizing agent with visible light, which induces cytotoxicity in the presence of oxygen as a result of forming reactive oxygen species (ROS). The ROS are the responsible components for invoking cell death and destruction of tumors. Although this mechanism is an effective cancer therapeutic, it still has many shortcomings. One major challenge of PDT concerns improving the tumor selectivity and specificity of photosensitizers because porphyrins have nonspecific affinity to tumor cells. The discussed research introduces a potential drug delivery vehicle to enhance the efficacy of cancer therapeutics and overcome the aforementioned issues. Specifically, hybrid composite particles composed of superparamagnetic polypeptide-coated silica nanoparticles conjugated to porphyrins were designed to improve the mechanism of tumor cell destruction via controlled assembly and transport.

Along the path of developing these nanocomposites, porphyrin self-assembly was explored to understand the dynamics of porphyrins alone. A series of complementary experiments and analytical methods were used, including UV-Vis and fluorescence spectroscopy measurements, small angle X-ray scattering (SAXS), cryogenic transmission electron microscopy (cryo-TEM) and freeze-fracture transmission electron microscopy (FF-TEM). Whereas UV-Vis and fluorescence techniques enabled us to determine the type of aggregates formed, AUC and SAXS provided complementary details and information about the size of the assemblies in solution. Cryo-TEM and FF-TEM provided direct visualization of the aggregates.

CHAPTER 1 GENERAL INTRODUCTION

1.1 Research Goals & Overview

The primary goal of this research is to develop a drug delivery vehicle to enhance the efficacy of cancer therapeutics. Specifically, hybrid composite particles composed of superparamagnetic polypeptide-coated silica nanoparticles conjugated to porphyrins will be used to improve the mechanism of tumor cell destruction via controlled assembly and transport.

Currently, the two common cancer treatment methods which utilize porphyrins include: boron-neutron capture therapy[1] (BNCT) and photodynamic therapy[2-4] (PDT). The research discussed in this dissertation focuses on enhancing the latter application, where porphyrins act as photosensitizers. The photochemical process for PDT involves exciting a photosensitizing agent with visible light, which induces cytotoxicity in the presence of oxygen as a result of forming reactive oxygen species (ROS). The ROS are the responsible components for invoking cell death and destruction of tumors.[5] (See Figure 1-1)[6]

A hematoporphyrin derivative (HpD), commercially known as Photofrin®, was the first PDT drug to receive approval from the United States Food and Drug Administration (FDA). Although Photofrin® is now well established as an effective cancer therapeutic, it still has many undesirable properties. For instance, it is not prepared in pure form; instead, it is administered as a complex mixture of oligomers. Also, Photofrin® is not rapidly cleared from normal tissue after treatment. Patients typically remain photosensitive for prolong periods (up to several weeks, depending on the treated condition) following administration of the drug.

Since the clinical debut of Photofrin®, a vast number of porphyrin-based photosensitizers have been reported, but there are still ongoing challenges to overcome. One major challenge involves improving the tumor selectivity and specificity of photosensitizers because porphyrins

have nonspecific affinity to tumor cells. In an attempt to address this issue, researchers have tried to direct photosensitizers to cellular targets by conjugation to ligands that are tumor-specific.[3,7-9] A series of porphyrin-peptide conjugates have been reported[10-12] by Vicente and coworkers. Each of the designed conjugates exhibited low dark toxicity and were efficiently taken up by human carcinoma HEp2 cells. Overall, the cellular uptake, intracellular localization, and cytotoxity were dependent of the nature and sequence of the amino acid residues, as well as the hydrophobic character of the conjugate.

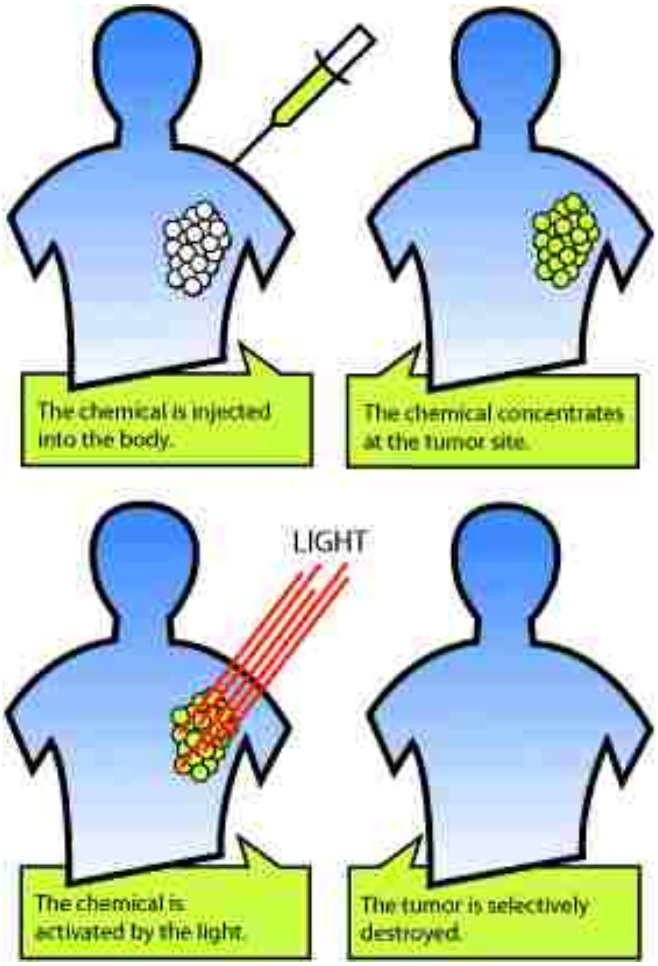

Figure 1-1 Representation of the photodynamic therapy process. Adapted from reference 6.

Aggregation is another factor to consider when developing an effective photosensitizer for PDT. Most molecules used as photosensitizers are hydrophobic and easily aggregate in aqueous media. When intracellular porphyrin aggregation occurs, the efficiency of ROS production is limited due to self-quenching effects.[13] On the other hand, aggregation facilitates the collective transport of photosensitizers to local tumor sites, minimizing incidental uptake and destruction of healthy cells. Depending on the chemical kinetics of the photosensitizing agent, the site of localization may vary, resulting in a complex array of cellular effects.[3] New approaches for counteracting these concerns include nanotechnology, which is an interdisciplinary field with applications in chemistry, material science, electronics, defense, energy and medicine.[14] Nanotechnology can also be defined as the study of the control of matter on the molecular and atomic scale. Generally, it involves structures within the limits of 100 nm and the development of materials or devices within the same size range.[3] Current nanotechnologies encompass buckyballs,[15] nanoparticles,[16] nanowires[17] and nanorods[18].

The use of platforms, such as nanoparticles, offers several significant benefits for PDT: (1) large payloads of photosensitizer can be added to the nanoparticles, and the particle surface can be modified to achieve the desired hydrophilicity for optimal plasma pharmacokinetics. (2) The attachment of targeting moieties onto the nanoparticle surface may permit increased selective delivery of the photosensitizers. (3) High levels of imaging agents can easily be combined with photosensitizers in the nanoparticles, providing an enhanced "see and treat" approach, where the placement of optical fibers is fluorescence image-guided to direct photoactivating light to subsurface tumors or to early nonclinically evident diseased tissue.[3] Moreover, the development of nanoparticles engineered for PDT can overcome many of the shortcomings of classic photosensitizers.[19-21]

Currently, various types of nanoparticles are being studied for their potential use as delivery vehicles for photosensitizers. These particles are generally categorized as biodegradable or non-biodegradable systems. For the purposes of PDT, non-biodegradable nanoparticles offer more advantages than biodegradable nanoparticles. For example, there is no time requirement for biodegradation, the photosensitizer can be protected from the environment, the particles can act as multifunctional platforms and can also be of smaller size.[21] A number of these multifunctional features, as well as many others, are illustrated in Figure 1-2.

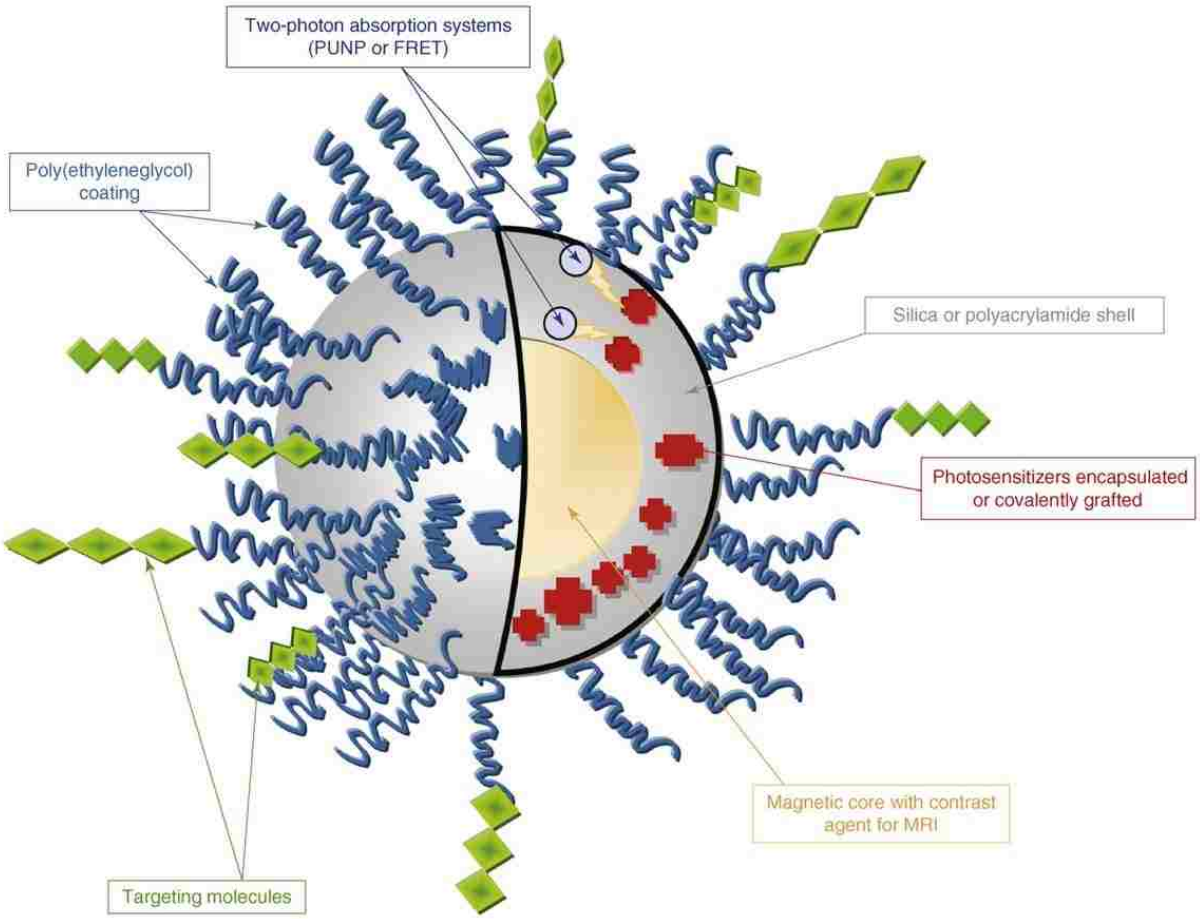

Figure 1-2 Afforded features of an ideal multifunctional nanoplatform. Abbreviations: FRET, fluorescence resonance energy transfer; MRI, magnetic resonance imaging; PUNP, photon upconverting nanoparticle. Adapted from Reference 21.

The main forms of non-degradable particles which have attracted interest are composed of gold, polyacrylamide and organically modified silica (ORMOSIL). Although polyacrylamide-based polymers can be used for the synthesis of these particles, most non-degradable systems are typically silica-based or metallic. Tang et al.[22] reported a comparative study on the encapsulation of methylene blue into three different types of sub-200 nm nanoparticles: one polyacrylamide-based and two silica-based particles. Of the two silica-based systems, one was composed of phenyltrimethoxysilane/methyltrimethoxysilane (PTMS/MTMS), whereas the other was composed of tetraethylorthosilicate (TEOS). According to their findings, polyacrylamide-based nanoparticles are small and possess a lower loading capacity than silica-based nanoparticles. Also, TEOS platforms exhibited the highest $^1O_2$ delivery per milligram of particle, which was threefold higher than that of polyacrylamide. The next highest level of $^1O_2$ delivery was displayed by PTMS/MTMS nanoparticles; approximately twofold higher than polyacrylamide.

Recently, Prasad et al.[19] developed a stable formulation of ORMOSIL nanoparticles for the encapsulation of 2-devinyl-2-(1-hexyloxyethyl) pyropheophorbide (HPPH), a hydrophobic photosensitizer which is currently undergoing clinical trials for esophageal cancer. The formulation was prepared by performing a controlled hydrolysis of triethylvinylsilane in micellar media. Based on *in vitro* experiments, the encapsulated photosensitizers showed significant levels of cell death upon photoactivation as a result of the free diffusion of molecular oxygen across the ORMOSIL matrix. However, due to the mesoporosity of these particles, a partial release of HPPH was observed during systematic circulation.[3] To overcome this issue, Prasad and coworkers later prepared a new formulation with the photosensitizers covalently-linked to the silica matrix. This modified system was obtained via the reaction of triethoxysilylaniline with the carboxylic acid-functionalized photosensitizer, followed by co-precipitation of the

ORMOSIL precursor, vinyltriethoxysilane (VTES), with the photosensitizer in a Tween 80/water micro-emulsion. Covalent attachment of the photosensitizer did not offset the photophysical properties of the system and singlet oxygen production was preserved.

In a study by Wieder and coworkers,[20] silica- and gold-based nanoparticles were compared for their potential use in PDT applications. They presumed that photosensitizers bound to the surface of gold might offer more advantages than encapsulated photosensitizers with regards to the diffusion of singlet oxygen species. In 2008, Burda et al.[23] reported the synthesis of PEGylated gold nanoparticles conjugated to phthalocyanine. Typically, it takes at least two days for the studied phthalocyanine to exhibit maximum accumulation in tumors; however, when conjugated to gold nanoparticles, maximum uptake occurred in less than two hours. Although these particles hold promise to be efficient delivery platforms, no *in vitro*/*in vivo* results have been reported with respect to PDT efficacy.

The rationale for the primary research goals and objectives is established on the basis of recent advances in nanotechnology and ongoing challenges of PDT. Provided the insight, as well as limitations of the previously described studies, a new hybrid nanoparticle was constructed with enhanced therapeutic capabilities. The use of porphyrins conjugated to superparamagnetic polypeptide-coated silica nanoparticles may provide the necessary features to overcome the current drawbacks of PDT.

Overall, the aim is the development of a controllable "on/off" switch for porphyrin aggregation. In theory, this capability will simultaneously optimize the transport and PDT efficacy of porphyrins under both, extra- and intracellular conditions, respectively. During guidance to the tumor site, porphyrin aggregation would be switched "on", minimizing interactions with healthy cells. Once directed to the site of interest, aggregation would be

switched "off" to enhance photoactivation. This will decrease the occurrence of self-quenching effects which results from aggregation. In addition, improved reactivity of the photosensitizers will decrease the required dosage for efficient $^1O_2$ production.

The feasibility of these nanoparticles to serve as drug delivery systems and biomedical devices is constituted by their biocompatibility, stability, and versatility.[24] Using polypeptide-functionalized silica particles as platforms promote these characteristics. Other potential applications for these composite nanoparticles include: responsive materials, chiral separations,[25] colloidal crystallization,[26] catalysis,[27] and biomimetic membrane supports.[28] Depending on the properties of the attached polypeptide, the particles can exhibit solubility in water or organic solvents. In addition, the polypeptide coil⇔helix transition is a useful feature for modifying the surface configuration and particle-particle interactions. In the discussed work, the objective is to coat the surface of silica cores with a biocompatible polypeptide shell, which will enhance particle solubility in a physiological environment. Such features are useful to exploit these versatile hybrids as drug delivery platforms for photosensitizers.

The inclusion of a magnetic moiety (i.e. iron oxide, which is FDA-approved) within the silica core provides an additional dimension for controlling drug transportation. In the presence of a remotely controlled high frequency magnetic field, magnetic colloidal particles assemble.[29] Upon removal of the magnetic field, the particles are capable of readily dispersing.[30] Exploiting these features can increase the reactivity of photosensitizers and minimize the required dosage. Also, magnetic guidance of the particles to target tissues (e.g., a tumor) will reduce the chance of destroying healthy tissues and eliminate associated side effects.[31] Yoon et al. reported similar core-shell particles for drug and gene delivery applications. In their study, magnetic

nanoparticles were coated with a shell of amorphous silica, which contained luminescent organic dye; biocompatible poly(ethylene glycol) was attached to the surface.

Liu et al.[32] described a procedure for the preparation of magnetic nanocomposite-bonded metalloporphyrins for biomimetic catalysis. In their approach, the metalloporphyrins were synthesized via a silanation reaction between 3-aminopropyltriethoxysilane (APTES) functionalized metalloporphyrins and silica-coated Fe_3O_4 nanoparticles. The target porphyrin species was prepared by amidation of its acyl chloride group with APTES. Herein, a facile approach[33] using "click" chemistry is introduced as an improved method of porphyrin immobilization to the surface of silica particles.

Before engineering our porphyrin-functionalized delivery vehicle, it was important to gain an understanding of the self-assembly and structural properties of porphyrins alone. In Chapter 2, a review of useful instrumentation and techniques used in the study of self-assembly *in situ* is provided. The results and data shown in that chapter comprise side projects, which also focused on the study of self-assembling systems; Chapter 3 describes findings for the aggregation of meso-tetra(4-sulfonatophenyl)porphyrin in aqueous solutions, which were determined using the techniques highlighted in Chapter 2. In Chapter 4, the synthesis and characterization of magnetic hybrid particles designed for controlled porphyrin assembly/transport is discussed.

1.2 Photodynamic Therapy (PDT)

PDT is a noninvasive clinical treatment for various diseases, including cancer and superficial tumors (e.g., lung, bladder, esophagus, melanoma). Treatment involves intravenous injection of a photosensitive drug which accumulates in the neoplastic tissues. Once the photosensitizer is excited, tumor necrosis is initiated due to the production of highly toxic singlet oxygen.

The simplified Jablonski diagram shown in Scheme 1-1 illustrates the photophysics of ROS generation during PDT sensitization. Once exposed to a particular wavelength of visible light (635-760 nm), the photosensitizer (porphyrin) transitions from a singlet ground state (P^0) to the first excited ($^1P^*$) singlet state **(1)**. The excited molecule can either return to its singlet ground state via fluorescence **(2)**, or undergo intersystem crossing **(3)** to its excited triplet state ($^3P^*$). The lifetime of the photosensitizer in the $^3P^*$ state (μs) is longer than that of the $^1P^*$ state (ns), which favors the interaction of this excited state with surrounding molecules. In the case where the photosensitizer follows the first pathway **(2)**, the tumor will fluoresce and become visible.

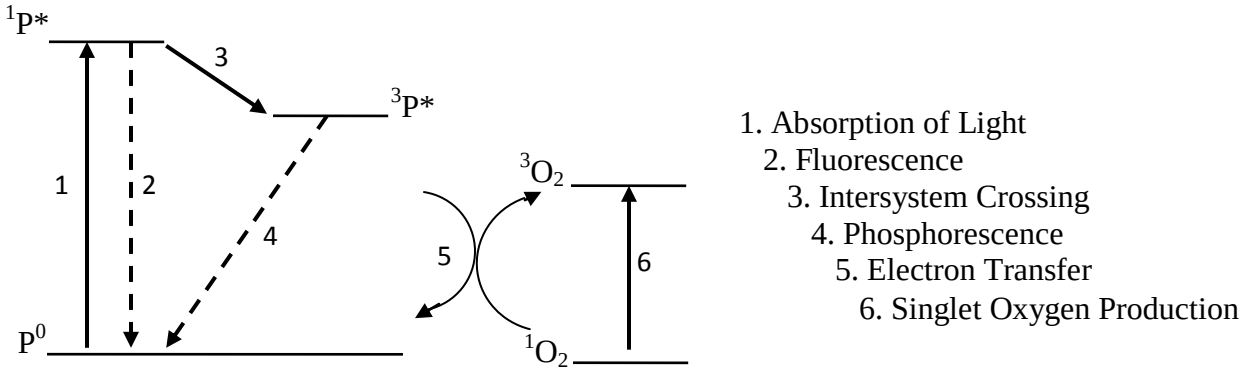

Scheme 1-1 Simplified Jablonski representation of PDT sensitization mechanism.

However, if the photosensitizer follows the second pathway **(3)**, it will subsequently undergo phosphorescence **(4)**. Cytotoxic species are generated from molecular oxygen in one of two potential ways, classified as Type I and Type II mechanisms. The Type I mechanism **(5)** involves the transfer of hydrogen atoms or electron-transfer between the excited photosensitizer and molecular oxygen, resulting in the production of ions or free radical species (peroxide anions and super oxide). In contrast, the Type II mechanism **(6)** involves the transfer of a hydrogen radical or an electron from the photosensitizer to molecular oxygen**,** which is considered the main process that occurs in PDT. The interaction of the $^3P^*$ state sensitizer with the triplet ground state

of molecular oxygen ($^3O_2$) yields highly cytotoxic singlet-state oxygen species ($^1O_2$) that is used in therapeutic treatment.[34]

Chemical sensitization with light was first observed by Raab in 1900, using acridine as the sensitizing agent for the irradiation of paramecium.[35] This reaction process was termed "photodynamic action" to distinguish it from the sensitization of photographic plates by dyes.[36] The potential of porphyrins to serve as anti-tumor agents in cancer therapeutics was recognized in the 1960s. The development of HpD provided detection and selective localization in malignant tissues.[37] In 1975, Dougherty et al. demonstrated the selective destruction of tumors with HpD upon irradiation.[38] Following this discovery, a more pure form of HpD was developed in 1983 and is commercially known today as Photofrin® (porfimer sodium). In 1995, Photofrin® received FDA approval in the United States and is now approved for use in more than 40 other countries.

1.3 Porphyrins

1.3.1 Fundamental Properties of Porphyrins

Porphyrins are tetrapyrrolic macrocycles conjoined by four methine (*meso*) carbons and possesses 22-π electrons; 18 of which are incorporated in any one delocalization pathway[39] (see Figure 1-3). Based on Hückel's (4n+2) rule, porphyrins are considered highly aromatic. These aromatic properties contribute to many of their useful applications, particularly in the field of medicine. For instance, products such as Photofrin® utilize the photochemical capabilities of porphyrins in photodynamic therapy (PDT) for the treatment of malignant tumors.[40]

Porphyrins are considered amphoteric, possessing acidic and basic properties as a result of the inner pyrrolic nitrogens. A strong base, such as alkoxide, is capable of removing the protons (pK_a ~16) from the nitrogen atoms, rendering a dianion porphyrin species. Conversely, the free pyrrolenine nitrogen atoms (pK_b ~9) can be protonated with acids, such as trifluoroacetic acid

(TFA), to form the dication species.[41] Sometimes when the tetrapyrrole is protonated or deprotonated, a color change is observed and confirms reaction. In addition, the inner protons can be replaced with various types of metals (e.g., Cu, Ni, Sn, Zn) via insertion into the macrocycle cavity using metal salts.[42-44] In contrast, metalloporphyrins can undergo demetalation upon treatment with acids. Depending on the type of metal, specific acids may be required for successful removal.[45]

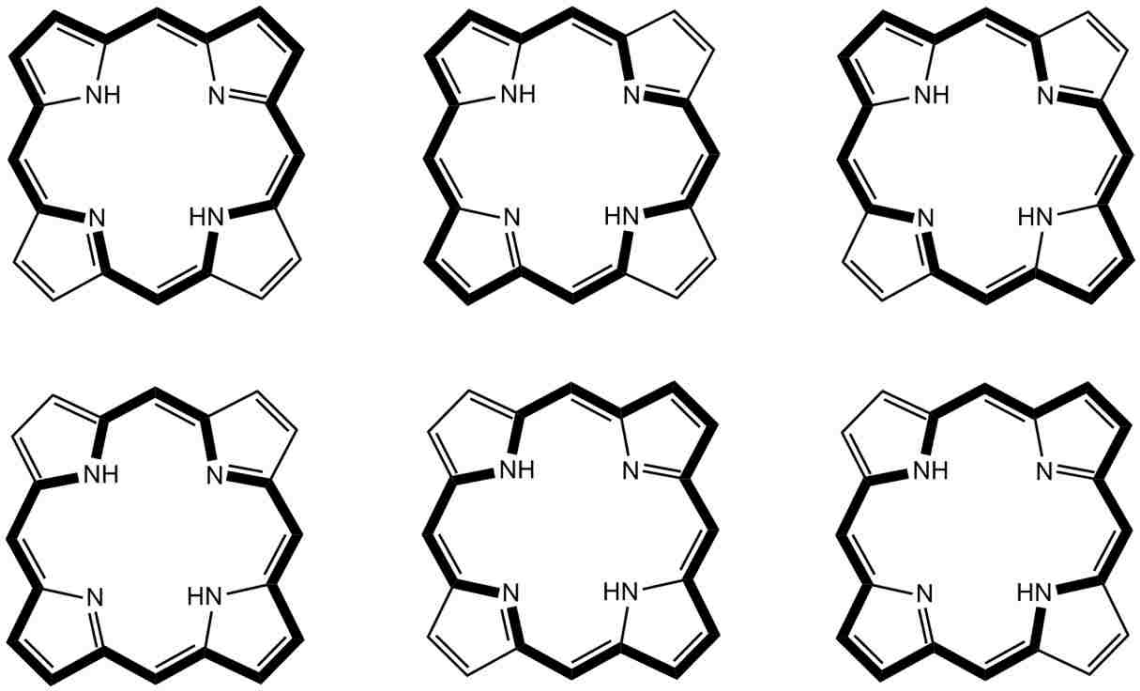

Figure 1-3 Fundamental porphyrin with 18-π electrons incorporated in six different delocalized pathways.

Excited state properties of porphyrins are the basis of their unique photochemistry. The prominent electronic transition for porphyrins is $\pi \rightarrow \pi *$ transitions which are associated with the macrocycle ring.[39] The aromatic ring current exhibits an anisotropic effect,[46] causing the shielded inner pyrrolic protons to shift upfield (-2 to -4 ppm) in the ^{1}H-NMR spectrum. In

contrast, the peripheral beta-pyrrolic and *meso* protons are deshielded and appear downfield (8-10 ppm).[47]

Typically, porphyrins exhibit a strong UV-Vis absorption band at ~420 nm, known as the Soret band.[48] Another characteristic includes four additional absorption bands, referred to as Q-bands, which are less intense and appear between 500-700 nm. Depending on the substituents and their location on the porphyrin, a shift in the bands may be observed.[49] For instance, substituents at the meso-positions of the macrocycle or at the beta-positions of the pyrroles will slightly shift the Soret and Q-bands.[39] As a result of protonation and self-aggregation, the compounds adopt new photochemical characteristics that are different from their monomeric properties. Spectroscopic techniques, such as UV-Vis and fluorescence spectroscopy, can be used to monitor the aggregation process by examining the changes in the photophysical properties (see Chapter 3 for further details).

1.3.2 A Brief History of Porphyrins

The physical properties and potential applications of porphyrins have attracted immense interest since the early 19th century. In 1818, Pelletier and Caventou were the first to isolate the green pigment of leaves and named it chlorophyll **1.1**.[50] This compound is a reduced form of porphyrin and is essential for the process of photosynthesis in plants and organisms. In 1844, Verdeil[51] recognized the relationship between chlorophyll and heme **1.2** when he observed the chemical conversion of chlorophyll to a red pigment.

Around 1867, Thudichum isolated the first porphyrin by treating cruorin (now referred to as hemoglobin) with sulfuric acid and performed an extraction using alcohol.[52] He described it as a "purple substance that fluoresced with a splendid blood-red colour."[53] Cruentine was the name given to this isolated species; however, it is well-known today as hematoporphyrin **1.3** (Figure 1-

4). In 1884, Nencki[54] successfully isolated the first pure porphyrin, hematoporphyrin hydrochloride, directly from heme.

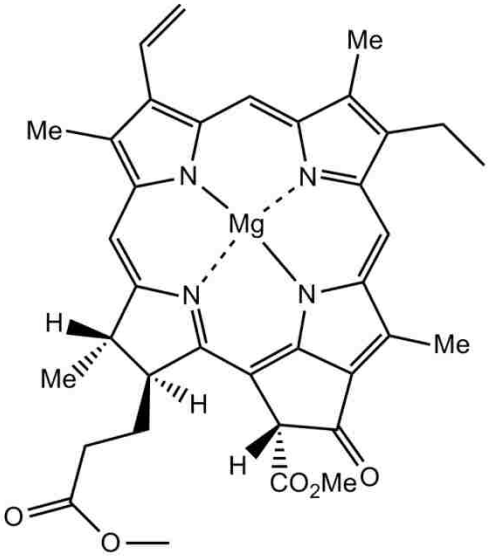

Chlorophyll-a **1.1**

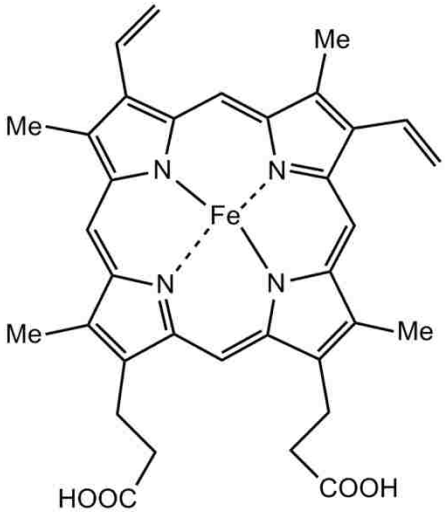

Heme **1.2**

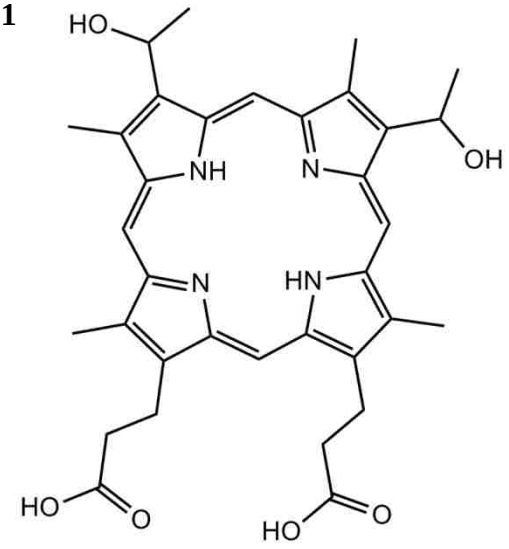

Hematoporphyrin **1.3**

Figure 1-4 Chemical structures of naturally occurring porphyrins.

Spectroscopic evidence of porphyrin was originally reported in 1883 when Soret[48] observed a strong electronic absorption band (420 nm) in the UV-Vis spectra of hemogloblin. A few decades later, the structure of porphyrin as four pyrrole groups linked by four methine bridges was proposed by Küster[55] in 1912; however, it was not widely accepted by the scientific

community. In 1913, the debate regarding this structure continued when Willstätter[56] proposed porphyrin as a tetrapyrrylethylene entity. In 1926, Fischer[57] reported the synthesis of octamethylporphyrin and type I, II, and III isomers of etioporphyrin, which confirmed the structure proposed by Küster was, indeed, correct.

1.3.3 Porphyrin Syntheses

1.3.3.1 Rothemund Method

Preparing specific porphyrin motifs requires the synthesis of porphyrin derivatives which possess functional groups at the periphery of the macrocycle.[58] In 1936, Rothemund and Menotti

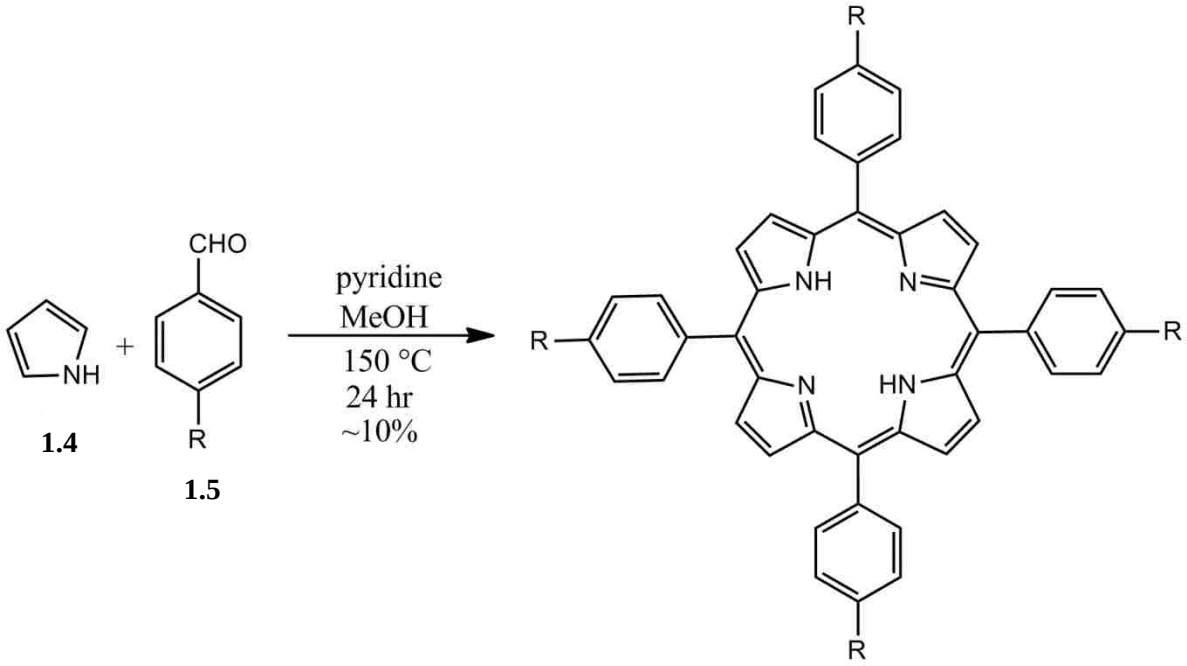

1.4 **1.5** **1.6**

Scheme 1-2 Synthesis of TPP via Rothemund method.

were the first to synthesize such a porphyrin, known as tetraphenylporphyrin (TPP) (Scheme 1-2).[59] The compound was obtained by reacting pyrrole (**1.4**) and benzaldehyde (**1.5**) in pyridine, while in a sealed tube at 150 °C for 24 hours, followed by oxidation of the resulting porphyrinogen.[60] This method produced relatively low yields (~10%) and due to the harsh reaction conditions, the range of

feasible substituted benzaldehydes was very limited. When the reaction was performed in the presence of $Zn(OAc)_2$ at high pressure, an improved yield was observed.

1.3.3.2 Alder-Longo Method

The Rothemund method was later modified by Adler and Longo under relatively milder reaction conditions. A wider range of substituents became attainable as a result of the conditions being less harsh. This new method of synthesizing TPP was also simpler than the original method. In fact, reaction rates were faster and the resulting yields were higher (20 ± 3 %).[61] (Scheme 1-3)

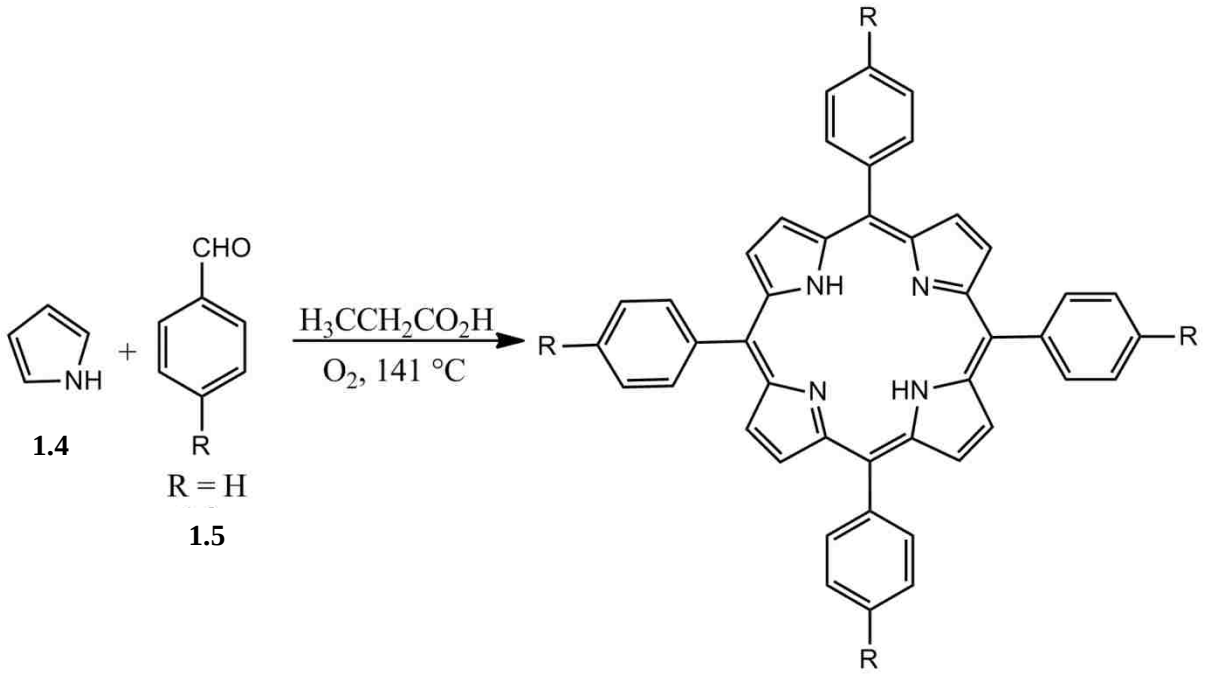

1.4 **1.5** **1.6**

Scheme 1-3 Synthesis of TPP via Adler-Longo method.

The reaction modifications involved refluxing pyrrole (**1.4**) and benzaldehyde (**1.5**) in propionic acid for 30 minutes at 141 °C. Although the Adler–Longo method provides a higher yield of TPP under comparatively milder reaction conditions, there are still some associated drawbacks. For instance, a high degree of tar is produced during the reaction which makes purification very

difficult.[62] Regardless of this issue, the Adler-Longo method is still one of the most efficient in the synthesis of TPP **1.6**, assuming the target porphyrin can be easily isolated.

1.3.3.3 Lindsey Method

In 1987, Lindsey et al. determined that TPP could actually be produced under equilibrium conditions. This synthetic strategy permits the formation of substituted porphyrins which were once unattainable using alternate routes.[62] The Lindsey method generates a colorless porphyrinogen product, and these intermediates are converted irreversibly to aromatic porphyrins upon oxidation. The procedure was developed based on pyrrole (**1.4**) and benzaldehyde (**1.5**) reacting to form the thermodynamically favored product, tetraphenylporphyrinogen (**1.7**), in a dilute solution (10^{-2} M) of dichloromethane (DCM) (Scheme 1-4).

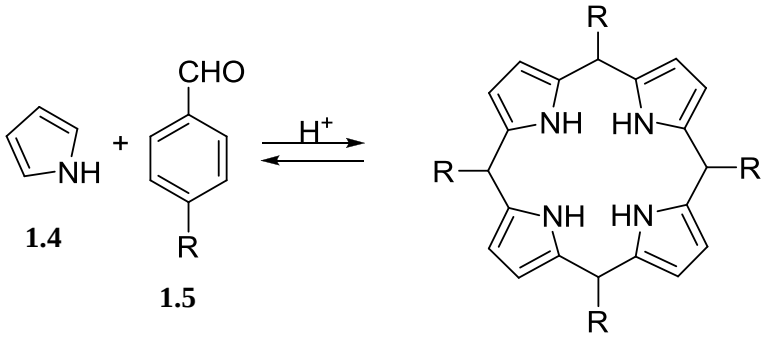

1.4 **1.5** **1.7**

Scheme 1-4 Synthesis of pyrrole (**1.4**) and benzaldehyde (**1.5**) to form thermodynamically favored tetraphenylporphyrinogen (**1.7**) at room temperature.

The Lindsey method has several factors that contribute to improved porphyrin yields. For instance, the selection of acid catalyst and oxidant, starting material concentrations, reaction time, and presence of water in the solvent can all influence the reaction.[63] The synthesis involved reacting pyrrole (**1.4**), benzaldehyde (**1.5**), and triethyl orthoacetate in a dilute solution of anhydrous DCM at equimolar concentrations (10^{-2} M) (Scheme 1-5). An aliquot of a Lewis acid

catalyst, such as $BF_3{\cdot}Et_2O$ or TFA (10^{-3} M), is added to the reaction mixture and allowed to sit at room temperature for ~1 h. Once the reaction has reached equilibrium, the oxidant can then be added to convert the porphyrinogen intermediate to porphyrin. DDQ and p-chloranil are both

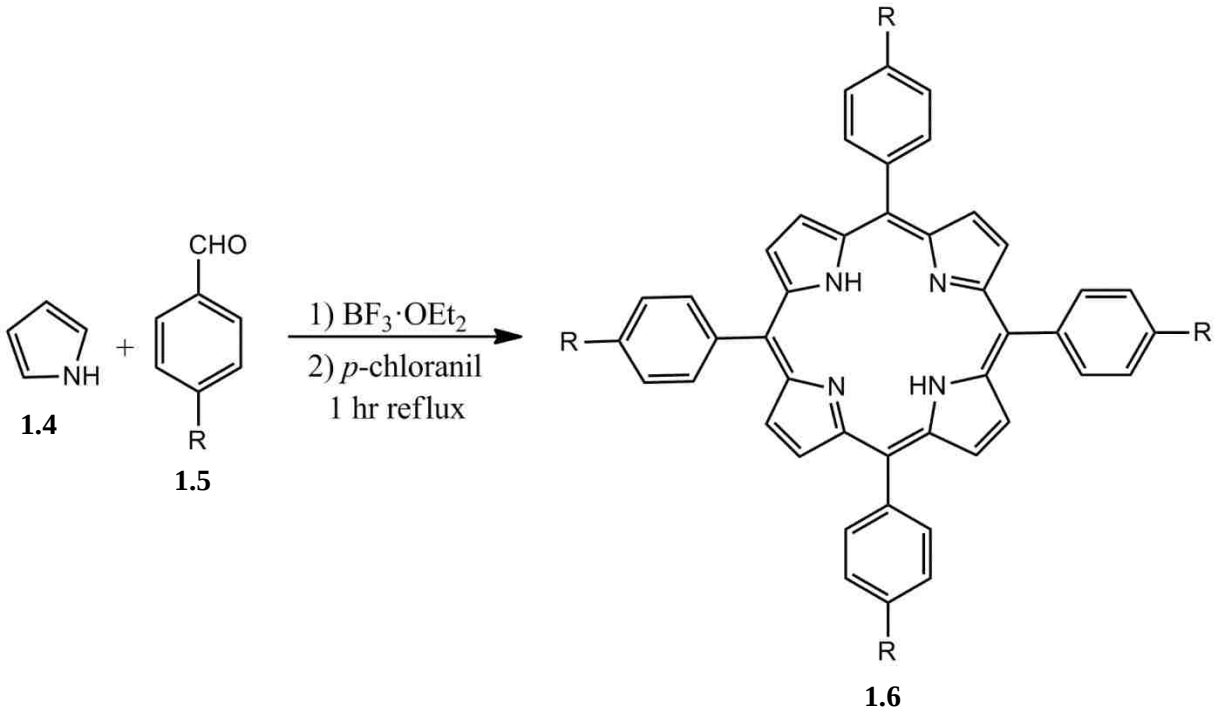

1.4 **1.5** **1.6**

Scheme 1-5 Synthesis of TPP via Lindsey method.

useful oxidants for this conversion. Adding DDQ yields an immediate conversion of the intermediate, whereas, *p*-chloranil is a milder oxidant and requires at least an hour to completely react. Though the reaction time when using *p*-chloranil is longer, it produces a higher yield of porphyrin than DDQ. Also, similar to benzene chemistry, the nucleophilicity of the pyrrole group depends on the attached functional group. For instance, if the pyrrole ring has an electron-donating group (e.g., alkyl group) present, it will more readily participate in electrophilic substitution reactions. In the case of an electron-withdrawing group (e.g., ester group) being attached to the pyrrole ring, a decrease in the reactivity will occur. Being mindful of the aforementioned factors, Lindsey strategically optimized the reaction conditions by monitoring

the yields of product at various reaction times via UV-Vis spectroscopy. As a result, the final TPP product can be obtained in much higher yields (50-55%) and more substituents are tolerated, which is a major improvement with respect to previous methods.

1.3.3.4 Asymmetrical Porphyrins from Symmetrical Porphyrins

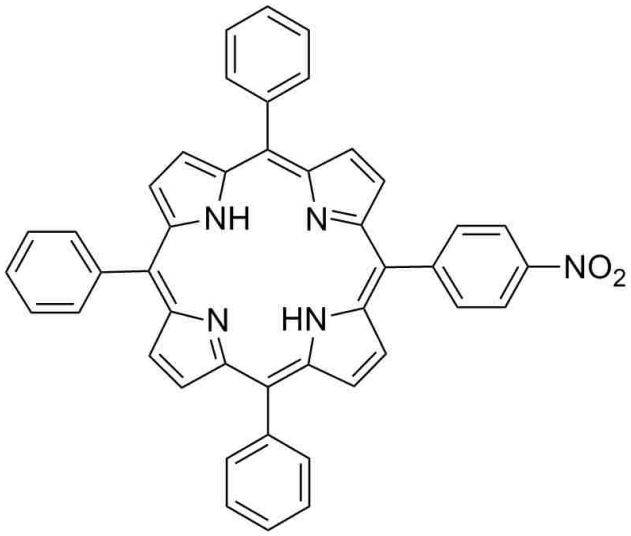

Figure 1-5 Molecular structure of mono-nitrophenylporphyrin.

Asymmetrical porphyrins can be prepared via mixed aldehyde condensation or selective functionalization of symmetrical porphyrins. The work described in this dissertation utilizes the latter method and will be the topic of discussion in this section. One of the earliest demonstrations of this procedure occurred in 1989, when Kruper et al.[64] synthesized mono-nitroporphyrin using fuming nitric acid to directly nitrate TPP (see Figure 1-5). The yields obtained using this method were moderate (46~56%), yet a vast improvement compared to previously reported studies.[65-67] Meng et al. later reported a method for obtaining relatively higher yields (~74%) under milder reaction conditions. Luguya et al.[68] devised a synthetic route using sodium nitrite in TFA, which enhanced the yield, as well as regioselectivity. The concentration of sodium nitrate and permitted reaction time are key factors which determined the

major products among various potential mixtures (e.g., mono-, di-, tri-, tetra-substituted TPP) in this reaction. Due to the absence of other tetrapyrrole byproducts, the mixtures are easily separated.

Similar to the work to be described in chapter 4, many studies exploit the single functional site as a mode for conjugating porphyrins to various peptides[7,69-73], proteins[74-76], DNA[77-79], surfaces[80-81], and other substrates. Kajiwara et al. reported the attachment of porphyrin moieties to the side chains of polyacrylamide with the aim of preparing functional polymers, which mimic a living system.[82] In our group, Sibrian-Vazquez et al.[7] developed a reaction well-suited for conjugating porphyrins to peptides. This method is utilized for the purposes of the discussed studies.

1.4 Colloidal Silica-Coated Superparamagnetic Particles

1.4.1 Colloidal Silica

Colloidal silica is a suspension of fine amorphous, nonporous, and typically spherical silica particles in the size range of ~1 nm to 1 μm.[83] Similar to atoms and molecules, these particles diffuse due to thermal motion. In comparison to other inorganic materials, silica and silicon compounds offer more beneficial properties. For instance, silica particles are easily surface-functionalized, which presents a wide range of options for chemical grafting. Also, the synthesis of these particles can yield monodispersed spheres with controllable size. In combination, colloidal silica spheres can serve as great platforms for hybrid structures.

In 1956, silica synthesis was discovered by Kolbe,[84] however, scientific interest in these nanoparticles did not flourish until the work of Stöber et al. was reported in 1968.[85] The Stöber synthesis produces well-defined monodispersed silica particles via hydrolysis of tetraethyl orthosilicate (TEOS) monomer, using ammonia as a catalyst. Generally, the solvent system for

this reaction mixture is a linear alcohol, such as ethanol, and water. Due to the partial positive charge of the silicon atom in TEOS, the Si-OEt bonds become hydrolyzed in the presence of water. A new silanol (Si-OH) bond is produced while an EtOH group is loss as a result of nucleophilic substitution. The silanol group of this molecule can then react with another TEOS monomer to form a Si-O-Si bond, yielding a dimer. As the polymerization proceeds, the hydrolyzed intermediates undergo condensation to form colloidal silica (Scheme 1-6).

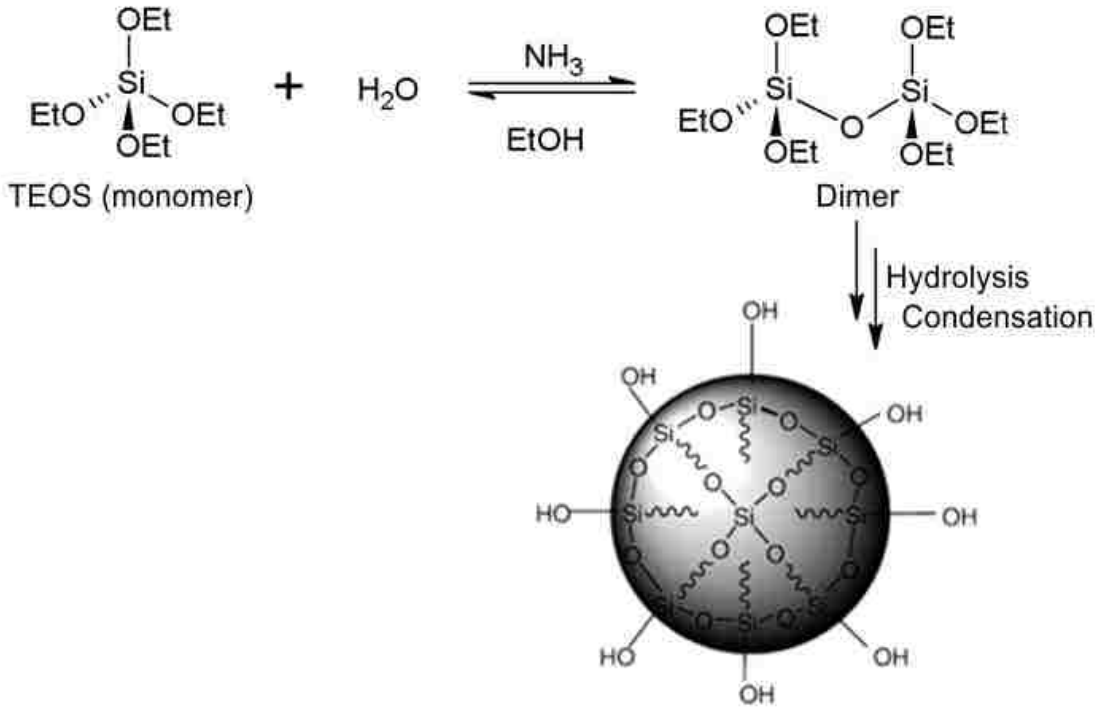

Scheme 1-6 Schematic representation of the synthesis of colloidal silica via the Stöber method.

To control the particle size, several factors can be adjusted in the reaction conditions. Typically, larger particles are produced when the concentration of water or ammonia is increased. Using alcohols of higher molecular weight can also yield larger particles, but with a broad size distribution.[86-88] An increase in temperature leads to the opposite effect and produces smaller particles. Another method used to control particle size and monodispersity involves

microemulsions.[89] A microemulsion is a thermodynamically stable dispersion which consists of two immiscible fluids (e.g., water-in-oil); surfactants are added to stabilize this system. The surfactants generate aggregates known as reverse (or inverted) micelles upon thermodynamically driven self-assembly. Among the different types of micelles, spherical reverse micelles are the most common. The central cores of these micelles act as capsules to ionic or polar molecules when added.[90] Due to the dynamic nature of the system, micelles frequently collide via Brownian motion, and then coalesce to form dimers. The dimerized micelles may exchange contents and break apart again, which results in a chemical reaction (see Figure 1-6). Because of this phenomenon, spherical reverse micelles are often exploited as "nanoreactors", providing an environment suitable for controlled nucleation and growth.[91]

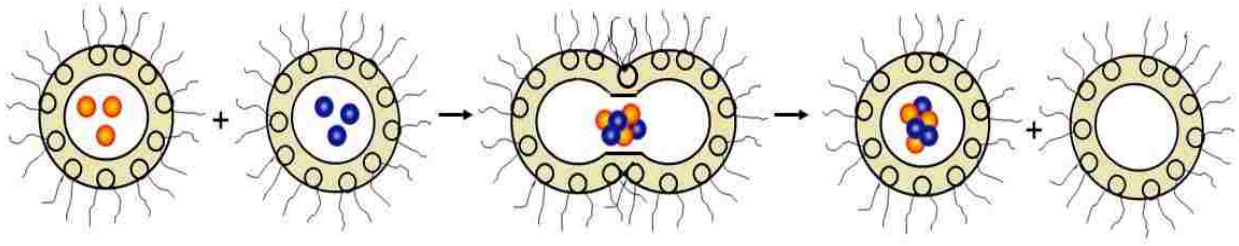

Figure 1-6 Representation of the content exchange process via the collision between spherical reverse micelles.

Magnetic inclusions within the core of silica nanoparticles can be added to provide a means of manipulating the assembly and transport of the colloidal particles. Interest in this feature is driven by the vast number of potential applications.[92-94] In terms of magnetically guided drug delivery vehicles, the most often used biocompatible material is iron oxide magnetite (Fe_3O_4).[31] It is minimally toxic and has been approved by the FDA as a magnetic resonance imaging (MRI) contrast agent.[95-97] The following section describes the properties of these particles in greater detail.

1.4.2 Fundamentals Properties of Magnetic Nanoparticles

Generally, magnetic particles are either composed of cobalt, iron, or nickel, as well as their oxidized derivatives. The nomenclature of these particles is based on the magnetic ordering of spins within the material.[98] In pure metal form, cobalt, iron, and nickel are referred to as ferromagnets, whereas their oxidized forms are ferrimagnets. Despite the naming difference, these materials show many common magnetic properties. For instance, both classes of particles are capable of storing magnetization upon removal/absence of an external magnetic field (i.e, remanence). Also, ferro- and ferrimagnetic materials have the ability to "remember" the magnetic history and retain ordering. This memory phenomenon is called hysteresis, defined as the inability of the magnetic material to relax back to zero magnetization, even after field removal.[99]

The Curie temperature of ferro/ferrimagnetic indicates the amount of energy needed to disrupt the long-range ordering in the material.[100] When heated above the Curie temperature, the spin-spin coupling within materials no longer can overcome thermal fluctuation energy, resulting in paramagnetism. A characteristic feature of paramagnetic materials is the lack of remanence and hysteresis. Therefore, in the presence and absence of an external field, paramagnetic particles can magnetize and demagnetize, respectively.

Information about the magnetic properties of a material is revealed via its hysteresis loop, which shows the correlation between the induced magnetic flux density (B) and magnetizing force (H).[99] Figure 1-7 depicts the dynamics of a classic hysteresis loop for ferromagnetic material. The starting point of magnetization "s" is noted at the origin of the plot, and the curve migrates to point "a" as a function of H. At the saturation point "a", all of the magnetic domains in the material are aligned. When the magnetic field H is reduced to zero (point "b"), the curve

reaches the point of retentivity, which indicates the remanence or level of remaining magnetism in the material. As the magnetic field *H* is reversed, the curve shifts to the point of coercivity (point "c"). At this point, enough of the domains within the material have flipped, resulting in a net magnetic flux density of zero. The material again becomes magnetically saturated at point "d", but in the opposite direction. As the reversed magnetic force reduces to zero (point "e"), the material displays residual magnetization equal to that of point "b" in the opposite direction. When the magnetization force is increased again in the positive direction, the curve moves to point "f" and the material exhibits a net flux density of zero. Lastly, the curve travels a different path as it returns back to the point of saturation "a".

A class of very small (<10 nm) metal or metal-oxide particles which display a remarkably large paramagnetic response to an external magnetic field are known as superparamagnetic nanoparticles. Regardless of whether above or below the Curie temperature, these nanoparticles maintain their paramagnetic response. This magnetic property is mainly attributed to the small size of superparamagnetic nanoparticles. The energy required to change the direction of magnetization of a particle is called the crystalline anisotropy energy and it depends on both the material properties and size. As the particle size decreases, so does the crystalline anisotropy energy, resulting in a decrease in the temperature at which the material becomes superparamagnetic.[101]

Similar to various biomedical applications (e.g., targeted drug delivery and MRI contrast enhancement), the work in this dissertation takes advantage of the highly responsive, remanence-free properties of superparamagnetic nanoparticles. These characteristics are ideal for controlled particle assembly/disassembly and serves as the driving force for enhanced photodynamic therapy.

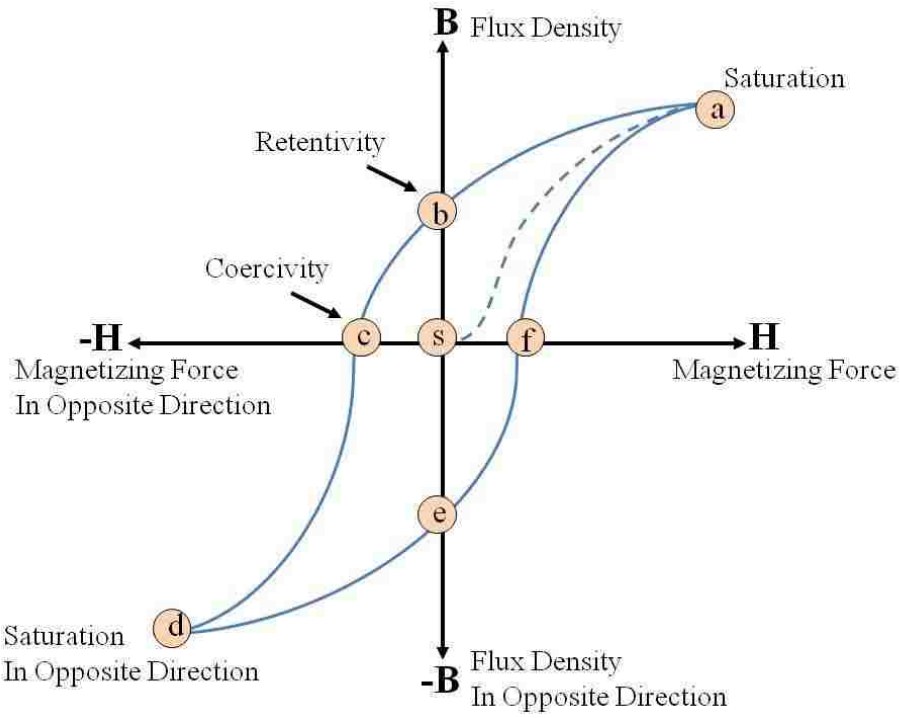

Figure 1-7 Hysteresis loop for ferromagnetic material. Magnetiziation of the particles increases as a function of applied field until saturation magnetization is reached.

1.4.3 Surface Modification & Characterization

1.4.3.1 Particle Surface Modification

Various studies have demonstrated techniques and syntheses for modifying the surface of silica,[102-109] which enhances the versatility of this nanoplatform. As a consequence, colloidal suspensions have a widespread use in applications ranging from advanced materials[110-112] to drug delivery[113-116,117] These applications also require the addition of powerful stabilizers that control the dispersion of particles in liquids.[118] Gellermann et al.[119] successfully modified the surface of spheres by silylation with silane coupling agents in efforts of improving dispersibility in organic media. Other methods of surface modification include polymer adsorption[120] and graft polymerization[121]. With respect to graft polymerization techniques, controlled radical polymerization (CRP) strategies such as atom transfer radical polymerization (ATRP),[122-124]

nitroxide-mediated polymerization (NMP),[125-126] and reversible addition-fragmentation chain transfer (RAFT)[127-128] are most commonly used for coating silica particles. Each of these approaches afford well-defined polymers with controlled molecular weight, low polydispersity, and variable functionality.[129]

1.5 Polypeptides

1.5.1 Polypeptide-Coated Particles

Due to their outstanding properties such as self-assembly and formation of liquid crystals[130], biodegradability and biocompatibility, polypeptides and their copolymers are very useful materials.[131] In addition, polypeptides have well-defined secondary structures (helices, sheets, turns) that are responsive to changes in temperature, pH, or salt.[132] Recently, Deming published work describing initiators and methods that permit polypeptide synthesis with good control of chain length, chain length distribution, and chain-end functionality.[133] These advantageous features make polypeptides excellent candidates for potential utility in nanodevices, biosensors, tissue engineering, bioseperation, biomaterials, and drug delivery.[134]

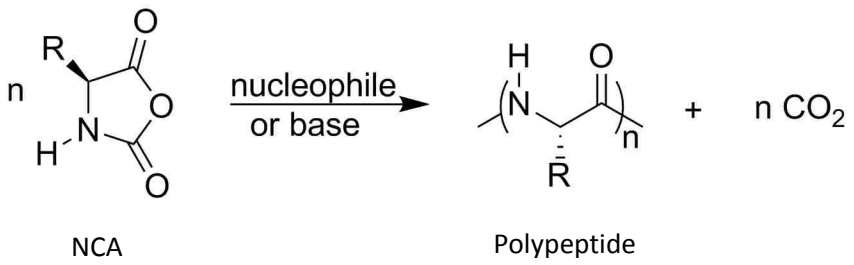

Scheme 1-7 NCA ring-opening polymerization.

In 1974, Dietz et al.[135] were among the first[136] to synthesize polypeptide-coated particles (PCPs). In our research group, Fong and Russo reported the preparation and characterization of colloidal silica coated with poly(γ-benzyl-α,L-glutamate), PBLG, a helical homopolypeptide.[137] Contrary to the aforementioned pioneers, Fong and Russo described the synthesis of silica-

polypeptide composite particles with latex-like uniformity. A few years later, Fong et al.[26] demonstrated a study on PCPs coated with poly(ε-carbobenzyloxy-L-lysine), PCBL, which displayed crystalline order not yet observed for PBLG-coated composite particles.

1.5.2 "Click" Chemistry of Polypeptides

The term "'click' chemistry" was coined by Sharpless et al.[138] to describe the Cu(I)-catalyzed cycloaddition reaction between alkyne and azide groups to form a very stable 1,2,3-triazole. This synthetic strategy gives very high yields, generate only inoffensive byproducts that can be removed by nonchromatographic methods, and is stereoselective.[139] In addition, click chemistry tolerates a variety of functional groups, and is a very rapid reaction. The reaction mechanism has a high thermodynamic driving force which contributes to its high efficiency. Overall, this synthetic approach is very practical and can be performed in various solvents, including water.

Several reports demonstrate the use of click chemistry to couple preformed polymers or biomolecules to other polymers, nucleic acids, peptides, sugars, proteins, viruses or cells. A few reports even demonstrate the use of click chemistry to produce block copolymers or homopolypeptides. However, very few reports describe the use of this reaction to couple polymers to silica nanoparticles. Recently, in our group Balamurugan et al.[33] applied click reactions to attach PSLG homopolypeptides to silica nanoparticles. In another study, Lin and coworkers[140] demonstrated the coupling of alkyne-functionalized proteins to azido-functionalized, silica-coated magnetic particles using click chemistry. Compared to random amide formation, this approach showed site-specific immobilization, as well as higher binding activity. The discussed work also utilizes this strategy to covalently attach alkyne-functionalized polypeptides to the surface of azide-functionalized, silica-coated magnetic nanoparticles.

1.6 References

(1) Martha, S.-V.; Vicente, M. G. H. Boron tumor delivery for BNCT: recent developments and perspectives. In *Boron Science*; CRC Press: Boca Raton, FL, 2011, p 209-242.

(2) Mroz, P.; Sharma, S. K.; Zhiyentayev, T.; Huang, Y.-Y.; Hamblin, M. R. Photodynamic Therapy: Photosensitizer Targeting and Delivery. In *Drug Delivery in Oncology*; Wiley-VCH Verlag GmbH & Co. KGaA: 2011, p 1569-1603.

(3) Ethirajan, M.; Chen, Y.; Joshi, P.; Pandey, R. K. The role of porphyrin chemistry in tumor imaging and photodynamic therapy. *Chem. Soc. Rev.* **2011**, *40*, 340-362.

(4) Henderson, B. W.; Dougherty, T. J. How does photodynamic therapy work? *Photochem. Photobiol.* **1992**, *55*, 145-157.

(5) Moan, J.; Peng, Q. An outline of the hundred-year history of PDT. *Anticancer Res.* **2003**, *23*, 3591-3600.

(6) BGSU; Photodynamic Therapy (PDT). http://www.photochembgsu.com/applications/therapy.html (accessed September 6 2012)

(7) Sibrian-Vazquez, M.; Jensen, T. J.; Hammer, R. P.; Vicente, M. G. H. Peptide-Mediated Cell Transport of Water Soluble Porphyrin Conjugates. *J. Med. Chem.* **2006**, *49*, 1364-1372.

(8) Manoharan, M. Oligonucleotide Conjugates as Potential Antisense Drugs with Improved Uptake, Biodistribution, Targeted Delivery, and Mechanism of Action. *Antisense Nucleic Acid Drug Dev.* **2002**, *12*, 103-128.

(9) Staneloudi, C.; Smith, K. A.; Hudson, R.; Malatesti, N.; Savoie, H.; Boyle, R. W.; Greenman, J. Development and characterization of novel photosensitizer : scFv conjugates for use in photodynamic therapy of cancer. *Immunology* **2007**, *120*, 512-517.

(10) Sibrian-Vazquez, M.; Jensen, T. J.; Fronczek, F. R.; Hammer, R. P.; Vicente, M. G. H. Synthesis and Characterization of Positively Charged Porphyrin-Peptide Conjugates. *Bioconjugate Chem.* **2005**, *16*, 852-863.

(11) Sibrian-Vazquez, M.; Hao, E.; Jensen, T. J.; Vicente, M. G. Enhanced cellular uptake with a cobaltacarborane-porphyrin-HIV-1 Tat 48-60 conjugate. *Bioconjugate Chem.* **2006**, *17*, 928-934.

(12) Sibrian-Vazquez, M.; Jensen, T. J.; Vicente, M. G. Synthesis, characterization, and metabolic stability of porphyrin-peptide conjugates bearing bifunctional signaling sequences. *J. Med. Chem.* **2008**, *51*, 2915-2923.

(13) Lambert, C. R.; Reddi, E.; Spikes, J. D.; Rodgers, M. A. J.; Jori, G. The effects of pophryin structure and aggregation state on photosensitized processes in aqueous and micellar media. *Photochem. Photobiol.* **1986**, *44*, 595-601.

(14) Hornyak, G. L.; Tibbals, H. F.; Dutta, J.; Moore, J. J. *Introduction to nanoscience and nanotechnology*; CRC Press: Boca Raton, FL, 2009.

(15) Noon, W. H.; Kong, Y.; Ma, J. Molecular dynamics analysis of a buckyball–antibody complex. *Proc. Nat. Acad. Sci. USA* **2002**, *99*, 6466-6470.

(16) Slowing, I. I.; Trewyn, B. G.; Giri, S.; Lin, V. S. Y. Mesoporous Silica Nanoparticles for Drug Delivery and Biosensing Applications. *Adv. Funct. Mater.* **2007**, *17*, 1225-1236.

(17) Fischer, K. E.; Alemán, B. J.; Tao, S. L.; Daniels, R. H.; Li, E. M.; Bünger, M. D.; Nagaraj, G.; Singh, P.; Zettl, A.; Desai, T. A. Biomimetic Nanowire Coatings for Next Generation Adhesive Drug Delivery Systems. *Nano Lett.* **2009**, *9*, 716-720.

(18) Giri, S.; Trewyn, B. G.; Stellmaker, M. P.; Lin, V. S. Y. Stimuli-Responsive Controlled-Release Delivery System Based on Mesoporous Silica Nanorods Capped with Magnetic Nanoparticles. *Angew. Chem. Int. Ed.* **2005**, *44*, 5038-5044.

(19) Roy, I.; Ohulchanskyy, T. Y.; Pudavar, H. E.; Bergey, E. J.; Oseroff, A. R.; Morgan, J.; Dougherty, T. J.; Prasad, P. N. Ceramic-Based Nanoparticles Entrapping Water-Insoluble Photosensitizing Anticancer Drugs: A Novel Drug−Carrier System for Photodynamic Therapy. *J. Am. Chem. Soc.* **2003**, *125*, 7860-7865.

(20) Wieder, M. E.; Hone, D. C.; Cook, M. J.; Handsley, M. M.; Gavrilovic, J.; Russell, D. A. Intracellular photodynamic therapy with photosensitizer-nanoparticle conjugates: cancer therapy using a 'Trojan horse'. *Photochem. Photobiol. Sci.* **2006**, *5*, 727-734.

(21) Bechet, D.; Couleaud, P.; Frochot, C.; Viriot, M.-L.; Guillemin, F.; Barberi-Heyob, M. Nanoparticles as vehicles for delivery of photodynamic therapy agents. *Trends Biotechnol.* **2008**, *26*, 612-621.

(22) Tang, W.; Xu, H.; Kopelman, R.; Philbert, M. A. Photodynamic characterization and in vitro application of methylene blue-containing nanoparticle platforms. *Photochem. Photobiol.* **2005**, *81*, 242-249.

(23) Cheng, Y.; A, C. S.; Meyers, J. D.; Panagopoulos, I.; Fei, B.; Burda, C. Highly efficient drug delivery with gold nanoparticle vectors for in vivo photodynamic therapy of cancer. *J. Am. Chem. Soc.* **2008**, *130*, 10643-10647.

(24) Hu, S.-H.; Liu, T.-Y.; Huang, H.-Y.; Liu, D.-M.; Chen, S.-Y. Magnetic-Sensitive Silica Nanospheres for Controlled Drug Release. *Langmuir* **2007**, *24*, 239-244.

(25) Edmondson, S.; Osborne, V. L.; Huck, W. T. S. Polymer brushes via surface-initiated polymerizations. *Chem. Soc. Rev.* **2004**, *33*, 14-22.

(26) Fong, B.; Turksen, S.; Russo, P. S.; Stryjewski, W. Colloidal Crystals of Silica−Homopolypeptide Composite Particles. *Langmuir* **2003**, *20*, 266-269.

(27) Zhong, C. J.; Maye, M. M. Core–Shell Assembled Nanoparticles as Catalysts. *Adv. Mater.* **2001**, *13*, 1507-1511.

(28) Troutier, A.-L.; Ladavière, C. An overview of lipid membrane supported by colloidal particles. *Adv. Colloid Interface Sci.* **2007**, *133*, 1-21.

(29) Zhang, F.; Wang, C.-C. Fabrication of One-Dimensional Iron Oxide/Silica Nanostructures with High Magnetic Sensitivity by Dipole-Directed Self-Assembly. *J. Phys. Chem. C* **2008**, *112*, 15151-15156.

(30) Liberti, P. A.; Rao, G. C.; Terstappen, L. W. M. M. In *PCT Int. Appl.* ; G01N 1/00 ed.; Organization, W. I. P., Ed.; Immunivest Corporation: USA, 2002; Vol. A1, p 66.

(31) Häfeli, U. O.; Riffle, J. S.; Harris-Shekhawat, L.; Carmichael-Baranauskas, A.; Mark, F.; Dailey, J. P.; Bardenstein, D. Cell Uptake and in Vitro Toxicity of Magnetic Nanoparticles Suitable for Drug Delivery. *Mol. Pharm.* **2009**, *6*, 1417-1428.

(32) Liu, C.-X.; Liu, Q.; Guo, C.-C.; Tan, Z. Preparation and characterization of novel magnetic nanocomposite-bonded metalloporphyrins as biomimetic nanocatalysts. *J. Porphyrins Phthalocyanines* **2010**, *14*, 825-831.

(33) Balamurugan, S. S.; Soto-Cantu, E.; Cueto, R.; Russo, P. S. Preparation of Organosoluble Silica-Polypeptide Particles by "Click" Chemistry. *Macromolecules* **2009**, *ASAP*.

(34) Samia, A. C. S.; Dayal, S.; Burda, C. Quantum Dot-based Energy Transfer: Perspectives and Potential for Applications in Photodynamic Therapy. *Photochem. Photobiol.* **2006**, *82*, 617-625.

(35) Raab, O. On the effect of fluorescent substances on infusoria. *Z. Biol.* **1900**, *39*, 524-546.

(36) Spikes, J. D.; Straight, R. Sensitized Photochemical Processes in Biological Systems. *Annu. Rev. Phys. Chem.* **1967**, *18*, 409-436.

(37) Lipson, R. L.; Baldes, E. J.; Gray, M. J. Hematoporphyrin derivative for detection and management of cancer. *Cancer* **1967**, *20*, 2255-2257.

(38) Dougherty, T. J. Photosensitizers: Therapy and Detection of Malignant Tumors. *Photochem. Photobiol.* **1987**, *45*, 879-889.

(39) Smith, K. *Porphyrins and Metalloporphyrins*; Elsevier Scientific Publishing Company: Amsterdam, 1975.

(40) Pandey, R. K.; Smith, K. M.; Dougherty, T. J. Porphyrin dimers as photosensitizers in photodynamic therapy. *J. Med. Chem.* **1990**, *33*, 2032-2038.

(41) Clarke, J. A.; Dawson, P. J.; Grigg, R.; Rochester, C. H. A spectroscopic study of the acid ionization of porphyrins. *J. Chem. Soc. Perk. Trans. 2* **1973**, 414-416.

(42) John Plater, M.; Aiken, S.; Bourhill, G. Metallated porphyrins containing lead(II), copper(II) or zinc(II). *Tetrahedron* **2002**, *58*, 2415-2422.

(43) Shen, Y.; Ryde, U. Reaction Mechanism of Porphyrin Metallation Studied by Theoretical Methods. *Chemistry – A European Journal* **2005**, *11*, 1549-1564.

(44) Shubina, T. E.; Marbach, H.; Flechtner, K.; Kretschmann, A.; Jux, N.; Buchner, F.; Steinrück, H.-P.; Clark, T.; Gottfried, J. M. Principle and Mechanism of Direct Porphyrin Metalation: Joint Experimental and Theoretical Investigation. *J. Am. Chem. Soc.* **2007**, *129*, 9476-9483.

(45) Lavallee, D. K. *The chemistry and biochemistry of N-substituted porphyrins*; VCH Publishers: Weinheim, 1987.

(46) Senge, M. O.; Smith, K. M. Structure and Confirmation of Photosynthetic Pigments and Related Compounds. 2. Nickel (II) Methyl Pryopheophorbide a–A Severely Distorted Chlorophyll Derivative*. *Photochem. Photobiol.* **1991**, *54*, 841-846.

(47) Smith, K. M.; Unsworth, J. F. Carbon-13 NMR spectra of some chlorins and other chlorophyll degradation products. *Tetrahedron* **1975**, *31*, 367-375.

(48) Soret, J. L. Recherches sur l'absorption des rayons ultra violets par diverses substances. *Arch. Sci. Phys. Nat.* **1883**, *10*, 430-485.

(49) Weiss Jr, C. The Pi electron structure and absorption spectra of chlorophylls in solution. *J. Mol. Spectrosc.* **1972**, *44*, 37-80.

(50) Pelletier, P. J.; Caventou, J. B. Sur la matière verte des feuilles. *Ann. Chim. Phys.* **1818**, *9*, 194–196.

(51) Verdeil, F. *J. Prakt. Chem.* **1844**, *33*, 478.

(52) Thudichum, J. L. W. Report on researches intended to promote an improved chemical identification of disease. *Report Med. Off. Privy. Council.* **1867**, *7*, 152-195.

(53) Thunell, S.; Floderus, Y.; Henrichson, A.; Harper, P. Porphyria in Sweden. *Physiol Res* **2006**, *55 Suppl 2*, S109-118.

(54) Nencki, M.; Sieber, N. eber das Hämatoporphyrin. *Arch. f. exper. Pathol.* **1888**, *24*, 430-446.

(55) Küster, W. Beitr/igo zur Kenntnis des Bilirubins und Haematins. *Z. Physiol. Chem.* **1912**, *82*, 463-483.

(56) Willstätter, R.; Fischer, M. *Hoppe-Seyler's Z. Physiol. Chem.* **1913**, *87*, 423-498.

(57) Fischer, H.; Klarer Synthese des Octamethylporphins, des Methyl-analogen des Ätioporphyrins. Mitteilung über Porphyrinsynthesen. *J. Liebigs Ann. Chem.* **1926**, *450*, 181.

(58) Lindsey, J. S.; Schreiman, I. C.; Hsu, H. C.; Kearney, P. C.; Marguerettaz, A. M. Rothemund and Adler-Longo reactions revisited: synthesis of tetraphenylporphyrins under equilibrium conditions. *J. Org. Chem.* **1987**, *52*, 827-836.

(59) Rothemund, P. A new porphyrin synthesis. The synthesis of porphin. *J. Am. Chem. Soc.* **1936**, *58*, 625.

(60) Rothemund, P.; Menotti, A. R. Porphyrin Studies. IV.1 The Synthesis of α,β,γ,δ-Tetraphenylporphine. *J. Am. Chem. Soc.* **1941**, *63*, 267-270.

(61) Adler, A. D.; Longo, F. R.; Finarelli, J. D.; Goldmacher, J.; Assour, J.; Korsakoff, L. A simplified synthesis for meso-tetraphenylporphine. *J. Org. Chem.* **1967**, *32*, 476-476.

(62) Lindsey, J. S.; Schreiman, I. C.; Hsu, H. C.; Kearney, P. C.; Marguerettaz, A. M. Rothemund and Adler-Longo reactions revisited: synthesis of tetraphenylporphyrins under equilibrium conditions. *J. Org. Chem.* **1987**, *52*, 827-836.

(63) Easson, M. Dissertation, Louisiana State University, 2008.

(64) Kruper, W. J.; Chamberlin, T. A.; Kochanny, M. Regiospecific aryl nitration of meso-substituted tetraarylporphyrins: a simple route to bifunctional porphyrins. *J. Org. Chem.* **2002**, *54*, 2753-2756.

(65) Hashimoto, Y.; Lee, C.-S.; Shudo, K.; Okamoto, T. Synthesis of porphyrin(Fe)-intercalators which cause DNA scission. *Tetrahedron Lett.* **1983**, *24*, 1523-1526.

(66) Hasegawa, E.; Nemoto, J.-I.; Kanayama, T.; Tsuchida, E. Syntheses and properties of vinyl monomers containing a meso-tetraphenylporphin ring and their copolymers. *Eur. Poly. J.* **1978**, *14*, 123-127.

(67) Collman, J. P.; Brauman, J. I.; Doxsee, K. M.; Halbert, T. R.; Bunnenberg, E.; Linder, R. E.; LaMar, G. N.; Del Gaudio, J.; Lang, G.; Spartalian, R. *J. Am. Chem. Soc.* **1980** *102*, 4182.

(68) Luguyaa, R.; Jaquinoda, L.; Fronczek, F. R.; Vicente, M. G. H.; Smith, K. M. Synthesis and reactions of meso-(p-nitrophenyl)porphyrins. *Tetrahedron* **2004**, *60*, 2757-2763.

(69) Sibrian-Vazquez, M.; Jensen, T. J.; Fronczek, F. R.; Hammer, R. P.; Vicente, M. G. H. Synthesis and Characterization of Positively Charged Porphyrinâˆ’Peptide Conjugates. *Bioconjugate Chem.* **2005**, *16*, 852-863.

(70) Dunetz, J. R.; Sandstrom, C.; Young, E. R.; Baker, P.; Van Name, S. A.; Cathopolous, T.; Fairman, R.; de Paula, J. C.; Akerfeldt, K. S. Self-Assembling Porphyrin-Modified Peptides. *Org. Lett.* **2005**, *7*, 2559-2561.

(71) Hasobe, T.; Kamat, P. V.; Troiani, V.; Solladie, N.; Ahn, T. K.; Kim, S. K.; Kim, D.; Kongkanand, A.; Kuwabata, S.; Fukuzumi, S. Enhancement of Light-Energy Conversion Efficiency by Multi-Porphyrin Arrays of Porphyrinâˆ’Peptide Oligomers with Fullerene Clusters. *J. Phys. Chem. B* **2004**, *109*, 19-23.

(72) Arai, T.; Inudo, M.; Ishimatsu, T.; Akamatsu, C.; Tokusaki, Y.; Sasaki, T.; Nishino, N. Self-Assembling of the Porphyrin-Linked Acyclic Penta- and Heptapeptides in Aqueous Trifluoroethanol. *J. Org. Chem.* **2003**, *68*, 5540-5549.

(73) Sibrian-Vazquez, M.; Jensen, T. J.; Vicente, M. G. H. Synthesis, Characterization, and Metabolic Stability of Porphyrinâˆ’Peptide Conjugates Bearing Bifunctional Signaling Sequences. *J. Med. Chem.* **2008**, *51*, 2915-2923.

(74) Sutton, J. M.; Clarke, O. J.; Fernandez, N.; Boyle, R. W. Porphyrin, Chlorin, and Bacteriochlorin Isothiocyanates: Useful Reagents for the Synthesis of Photoactive Bioconjugatesâ€ *Bioconjugate Chem.* **2002**, *13*, 249-263.

(75) Rahimipour, S.; Ben-Aroya, N.; Ziv, K.; Chen, A.; Fridkin, M.; Koch, Y. Receptor-mediated targeting of a photosensitizer by its conjugation to gonadotropin-releasing hormone analogues. . *J. Med. Chem.* **2003**, *46*, 3965-3974.

(76) Chaloin, L.; Bigey, P.; Loup, C.; Marin, M.; Galeotti, N.; Piechaczyk, M.; Heitz, F.; Meunier, B. Improvement of porphyrin cellular delivery and activity by conjugation to a carrier peptide. *Bioconjugate Chem.* **2001**, *12*, 691-700.

(77) Sitaula, S.; Reed, S. M. Porphyrin conjugated to DNA by a 2'-amido-2'-deoxyuridine linkage. *Bioorg. Med. Chem. Lett* **2008**, *18*, 850-855.

(78) Bouamaied, I.; Nguyen, T.; Rühl, T.; Stulz, E. Supramolecular helical porphyrin arrays using DNA as a scaffold. *Org. Biomol. Chem.* **2008**, *6*, 3888 - 3891.

(79) Balaz, M.; Li, B. C.; Steinkruger, J. D.; Ellestad, G. A.; Nakanishi, K.; Berova, N. Porphyrins conjugated to DNA as CD reporters of the salt-induced B to Z-DNA transition. *Org. Biomol. Chem.* **2006**, *4*, 1865-1867.

(80) Imahori, H.; Norieda, H.; Nishimura, Y.; Yamazaki, I.; Higuchi, K.; Kato, N.; Motohiro, T.; Yamada, H.; Tamaki, K.; Arimura, M.; Sakata, Y. Chain Length Effect on the Structure and Photoelectrochemical Properties of Self-Assembled Monolayers of Porphyrins on Gold Electrodes. *J. Phys. Chem. B* **2000**, *104*, 1253-1260.

(81) Pilloud, D. L.; Chen, X.; Dutton, P. L.; Moser, C. C. Electrochemistry of Self-Assembled Monolayers of Iron Protoporphyrin IX Attached to Modified Gold Electrodes through Thioether Linkage. *J. Phys. Chem. B* **2000**, *104*, 2868-2877.

(82) Kajiwara, A.; Aramata, K.; Nomura, S.; Morishima, Y.; Kamachi, M. Radical polymerization of 5-(4-acrylamido)phenyl-10,15,20-triphenylporphyrin. *Chemistry Letters* **1992**, *1*, 95-98.

(83) Grace, W. R. "Colloidal silica" http://www.grace.com/EngineeredMaterials/MaterialSciences/ColloidalSilica/Default.aspx November 1, 2009 2009

(84) Kolbe, G. Ph.D. Dissertation, Friedrich-Schiller-Universit, 1956.

(85) Stöber, W.; Fink, A.; Bohn, E. Controlled growth of monodisperse silica spheres in the micron size range. *Colloid Polym. Sci.* **1968**, *26*, 62-69.

(86) Bogush, G. H.; Tracy, M. A.; Zukoski Iv, C. F. Preparation of monodisperse silica particles: Control of size and mass fraction. *J. Non-Crystalline Solids* **1988**, *104*, 95-106.

(87) Nooney, R. I.; Thirunavukkarasu, D.; Chen, Y.; Josephs, R.; Ostafin, A. E. Synthesis of Nanoscale Mesoporous Silica Spheres with Controlled Particle Size. *Chem. Mater.* **2002**, *14*, 4721-4728.

(88) Yano, K.; Fukushima, Y. Particle size control of mono-dispersed super-microporous silica spheres. *J. Mater. Chem.* **2003**, *13*, 2577-2581.

(89) Yang, Y.; Jing, L.; Yu, X.; Yan, D.; Gao Coating Aqueous Quantum Dots with Silica via Reverse Microemulsion Method: Toward Size-Controllable and Robust Fluorescent Nanoparticles. *Chem. Mater.* **2007**, *19*, 4123-4128.

(90) Hyeon, T.; Lee, S. S.; Park, J.; Chung, Y.; Na, H. B. Synthesis of Highly Crystalline and Monodisperse Maghemite Nanocrystallites without a Size-Selection Process. *J. Am. Chem. Soc.* **2001**, *123*, 12798-12801.

(91) Lee, Y.; Lee, J.; Bae, C. J.; Park, J. G.; Noh, H. J.; Park, J. H.; Hyeon, T. Large-Scale Synthesis of Uniform and Crystalline Magnetite Nanoparticles Using Reverse Micelles as Nanoreactors under Reflux Conditions. *Adv. Funct. Mater.* **2005**, *15*, 503-509.

(92) Lee, D.; Cohen, R. E.; Rubner, M. F. Antibacterial Properties of Ag Nanoparticle Loaded Multilayers and Formation of Magnetically Directed Antibacterial Microparticles. *Langmuir* **2005**, *21*, 9651-9659.

(93) Cousin, F.; Cabuil, V.; Levitz, P. Magnetic Colloidal Particles as Probes for the Determination of the Structure of Laponite Suspensions. *Langmuir* **2002**, *18*, 1466-1473.

(94) Tierno, P.; Sagués, F.; Johansen, T. H.; Fischer, T. M. Colloidal transport on magnetic garnet films. *Phys. Chem. Chem. Phys.* **2009**, *11*, 9615 - 9625.

(95) Tiefenauer, L. X.; Tschirky, A.; Kühne, G.; Andres, R. Y. In vivo evaluation of magnetite nanoparticles for use as a tumor contrast agent in MRI. *J. Magn. Reson. Imaging* **1996**, *14*, 391-402.

(96) Fahlvik, A. K.; Klaveness, J.; Stark, D. D. Iron oxides as MR imaging contrast agents. *J. Magn. Reson. Imaging* **1993**, *3*, 187-194.

(97) Lu, Q. H.; Yao, K. L.; Xi, D.; Liu, Z. L.; Luo, X. P.; Ning, Q. Synthesis and characterization of composite nanoparticles comprised of gold shell and magnetic core/cores. *Journal of Magnetism and Magnetic Materials* **2006**, *301*, 44-49.

(98) Akbarzadeh, A.; Samiei, M.; Davaran, S. Magnetic nanoparticles: preparation, physical properties, and applications in biomedicine. *Nanoscale Res Lett* **2012**, *7*, 144.

(99) Fonseca, F. C.; Goya, G. F.; Jardim, R. F.; Muccillo, R.; Carreño, N. L. V.; Longo, E.; Leite, E. R. Superparamagnetism and magnetic properties of Ni nanoparticles embedded in SiO_2. *Phys. Rev. B: Condens. Matter* **2002**, *66*, 104406.

(100) Ślawska-Waniewska, A.; Gutowski, M.; Lachowicz, H. K.; Kulik, T.; Matyja, H. Superparamagnetism in a nanocrystalline Fe-based metallic glass. *Phys. Rev. B: Condens. Matter* **1992**, *46*, 14594-14597.

(101) Suzuki, M.; Fullem, S. I.; Suzuki, I. S. Scaling form of zero-field-cooled and field-cooled susceptibility in superparamagnet. *J. Magn. Magn. Mater.* **2010**, *322*, 3178-3185.

(102) Shen, R.; Camargo, P. H. C.; Xia, Y.; Yang, H. Silane-Based Poly(ethylene glycol) as a Primer for Surface Modification of Nonhydrolytically Synthesized Nanoparticles Using the StoÌˆber Method. *Langmuir* **2008**, *24*, 11189-11195.

(103) Chu, C.-C.; Ueno, N.; Imae, T. Solid-Phase Synthesis of Amphiphilic Dendron-Surface-Modified Silica Particles and Their Application Toward Water Purification. *Chem. Mater.* **2008**, *20*, 2669-2676.

(104) Wang, D.; Duan, X.; Zhang, J.; Yao, A.; Zhou, L.; Huang, W. Fabrication of superparamagnetic hydroxyapatite with highly ordered three-dimensional pores. *J. Mater. Sci.* **2009**, *44*, 4020-4025.

(105) Shin, Y.; Lee, D.; Lee, K.; Ahn, K. H.; Kim, B. Surface properties of silica nanoparticles modified with polymers for polymer nanocomposite applications. *Journal of Industrial and Engineering Chemistry* **2008**, *14*, 515-519.

(106) Chandran, S. P.; Hotha, S.; Prasad, B. L. V. Tunable surface modification of silica nanoparticles through 'click' chemistry. *Current Science* **2008**, *95*, 1327-1333.

(107) Sakly, N.; Chevalier, Y.; Ben Ouada, H.; Jaffrezic-Renault, N. Surface modification of Si/SiO2 by polymeric anion-exchanging membrane: Effect on interfacial morphology and electrochemical properties. *Materials Science and Engineering: C* **2008**, *28*, 923-931.

(108) Qiang, W.; Wang, Y.; He, P.; Xu, H.; Gu, H.; Shi, D. Synthesis of Asymmetric Inorganic/Polymer Nanocomposite Particles via Localized Substrate Surface Modification and Miniemulsion Polymerization. *Langmuir* **2008**, *24*, 606-608.

(109) Beck, C.; Härtl, W.; Hempelmann, R. Covalent Surface Functionalization and Self-Organization of Silica Nanoparticles. *Angew. Chem.* **1999**, *38*, 1297-1300.

(110) Kim, J.-H.; Bryan, W. W.; Chung, H.-W.; Park, C. Y.; Jacobson, A. J.; Lee, T. R. Gold, Palladium, and Goldâ^'Palladium Alloy Nanoshells on Silica Nanoparticle Cores. *ACS Appl. Mater. Interfaces* **2009**, *1*, 1063-1069.

(111) Kim, K.; Lee, Y. M.; Lee, H. B.; Shin, K. S. Silver-Coated Silica Beads Applicable as Core Materials of Dual-Tagging Sensors Operating via SERS and MEF. *ACS Appl. Mater. Interfaces* **2009**, *1*, 2174-2180.

(112) Kang, D. J.; Han, D. H.; Kang, D. P. Fabrication and characterization of photocurable inorganic-organic hybrid materials using organically modified colloidal-silica nanoparticles and acryl resin. *Journal of Non-Crystalline Solids* **2009**, *355*, 397-402.

(113) Eskandar, N. G.; Simovic, S.; Prestidge, C. A. Nanoparticle Coated Emulsions as Novel Dermal Delivery Vehicles. *Current Drug Delivery* **2009**, *6*, 367-373.

(114) Zhao, Y.; Trewyn, B. G.; Slowing, I. I.; Lin, V. S. Y. Mesoporous Silica Nanoparticle-Based Double Drug Delivery System for Glucose-Responsive Controlled Release of Insulin and Cyclic AMP. *J. Am. Chem. Soc.* **2009**, *131*, 8398-8400.

(115) Liu, J.; Jiang, X.; Ashley, C.; Brinker, C. J. Electrostatically Mediated Liposome Fusion and Lipid Exchange with a Nanoparticle-Supported Bilayer for Control of Surface Charge, Drug Containment, and Delivery. *J. Am. Chem. Soc.* **2009**, *131*, 7567-7569.

(116) Lu, J.; Liong, M.; Zink, Jeffrey I.; Tamanoi, F. Mesoporous Silica Nanoparticles as a Delivery System for Hydrophobic Anticancer Drugs13. *Small* **2007**, *3*, 1341-1346.

(117) Tohver, V.; Smay, J. E.; Braem, A.; Braun, P. V.; Lewis, J. A. Nanoparticle halos: A new colloid stabilization mechanism. *Proc. Nat. Acad. Sci. U.S.A.* **2001**, *98*, 8950-8954.

(118) de Laat, A. W. M.; Schoo, H. F. M. Novel poly(vinyl ether) block copolymers: Synthesis and colloidal stabilization of α-Fe2O3 in water and organic solvents. *Colloid Polym. Sci.* **1998**, *276*, 176-185.

(119) Gellermann, C.; Storch, W.; Wolter, H. Synthesis and Characterization of the Organic Surface Modifications of Monodisperse Colloidal Silica. *J. Sol.-Gel Sci. Technol.* **1997**, *8*, 173-176.

(120) Thies, C. Adsorption of styrene/butadiene copolymers and stabilization of silica dispersed in perchloroethylene. *Colloid Polym. Sci.* **1976**, *54*, 13-21.

(121) Bridger, K.; Fairhurst, D.; Vincent, B. Nonaqueous silica dispersions stabilized by terminally-grafted polystyrene chains. *Colloid Polym. Sci.* **1979**, *68*, 190-195.

(122) Wang, J.-S.; Matyjaszewski, K. Controlled/"Living" Radical Polymerization. Halogen Atom Transfer Radical Polymerization Promoted by a Cu(I)/Cu(II) Redox Process. *Macromolecules* **2002**, *28*, 7901-7910.

(123) Kato, M.; Kamigaito, M.; Sawamoto, M.; Higashimura, T. Polymerization of Methyl Methacrylate with the Carbon Tetrachloride/Dichlorotris-(triphenylphosphine)ruthenium(II)/Methylaluminum Bis(2,6-di-tert-butylphenoxide) Initiating System: Possibility of Living Radical Polymerization. *Macromolecules* **2002**, *28*, 1721-1723.

(124) Matyjaszewski, K.; Xia, J. Atom Transfer Radical Polymerization. *Chem. Rev.* **2001**, *101*, 2921-2990.

(125) Hawker, C. J.; Bosman, A. W.; Harth, E. New Polymer Synthesis by Nitroxide Mediated Living Radical Polymerizations. *Chem. Rev.* **2001**, *101*, 3661-3688.

(126) Georges, M. K.; Veregin, R. P. N.; Kazmaier, P. M.; Hamer, G. K. Narrow molecular weight resins by a free-radical polymerization process. *Macromolecules* **2002**, *26*, 2987-2988.

(127) Chiefari, J.; Chong, Y. K.; Ercole, F.; Krstina, J.; Jeffery, J.; Le, T. P. T.; Mayadunne, R. T. A.; Meijs, G. F.; Moad, C. L.; Moad, G.; Rizzardo, E.; Thang, S. H. Living Free-Radical Polymerization by Reversible Additionâˆ’Fragmentation Chain Transfer: The RAFT Process. *Macromolecules* **1998**, *31*, 5559-5562.

(128) Chong, Y. K.; Le, T. P. T.; Moad, G.; Rizzardo, E.; Thang, S. H. A More Versatile Route to Block Copolymers and Other Polymers of Complex Architecture by Living Radical Polymerization: The RAFT Process. *Macromolecules* **1999**, *32*, 2071-2074.

(129) Huang, Y.; Liu, Q.; Zhou, X.; Perrier, S. b.; Zhao, Y. Synthesis of Silica Particles Grafted with Well-Defined Living Polymeric Chains by Combination of RAFT Polymerization and Coupling Reaction. *Macromolecules* **2009**, *42*, 5509-5517.

(130) Robinson, C. Liquid-crystalline structures in polypeptide solutions. *Tetrahedron* **1961**, *13*, 219-234.

(131) Peng, Y.-L.; Lai, S.-L.; Lin, C.-C. Preparation of Polypeptide via Living Polymerization of Z-Lys-NCA Initiated by Platinum Complexes. *Macromolecules* **2008**, *41*, 3455-3459.

(132) Voet, D.; Voet, J. G. In *Biochemistry*; 2nd ed.; Wiley: New York, 1995.

(133) Deming, T. J. Polypeptide and polypeptide hybrid copolymer synthesis via NCA polymerization. In *Peptide Hybrid Polymers*; Springer Berlin / Heidelberg: 2006; Vol. 202, p 1-18.

(134) Chockalingam, K.; Blenner, M.; Banta, S. Design and application of stimulus-responsive peptide systems. *Protein Eng.* **2007**, *20*, 155-161.

(135) Dietz, V. E.; Fery, N.; Hamann, K. *Angew. Makromol. Chem.* **1974**, *35*, 115-129.

(136) Tsubokawa, N.; Kobayashi, K.; Sone, Y. Grafting of Polypeptide from Carbon Black by the Ring-Opening Polymerization of γ-Methyl l-Glutamate N-Carboxyanhydride Initiated by Amino Groups on Carbon Black Surface. *Polym. J.* **1987**, *19*, 1147-1155.

(137) Fong, B.; Russo, P. S. Organophilic Colloidal Particles with a Synthetic Polypeptide Coating. *Langmuir* **1999**, *15*, 4421-4426.

(138) Díaz, D. D.; Punna, S.; Holzer, P.; McPherson, A. K.; Sharpless, K. B.; Fokin, V. V.; Finn, M. G. Click chemistry in materials synthesis. 1. Adhesive polymers from copper-catalyzed azide-alkyne cycloaddition. *J. Polym. Sci., Part A: Polym. Chem.* **2004**, *42*, 4392-4403.

(139) Kolb, H. C.; Finn, M. G.; Sharpless, K. B. Click Chemistry: Diverse Chemical Function from a Few Good Reactions. *Angew. Chem.* **2001**, *40*, 2004-2021.

(140) Lin, P.-C.; Ueng, S.-H.; Yu, S.-C.; Jan, M.-D.; Adak, A. K.; Yu, C.-C.; Lin, C.-C. Surface Modification of Magnetic Nanoparticle via Cu(I)-Catalyzed Alkyne-azide [2 + 3] Cycloaddition. *Org. Lett.* **2007**, *9*, 2131-2134.

CHAPTER 2 CURRENT METHODS AND THEIR APPLICATIONS FOR CHARACTERIZATION OF IN SITU SELF-ASSEMBLING SYSTEMS

2.1 Introduction and General Principles

Self-assembled colloidal systems, such as micelles and liposomes, are extensively being investigated for carrier/delivery purposes to improve upon the pharmacological properties of conventional ("free") drugs. Delivery vehicles are useful in new routes of administration for poorly water-soluble substances. Also, the carrier devices may protect drugs from degradation in biological fluids, which enhances their pharmacokinetics[1]. General properties of colloidal formulations which influence their functionality include: particle size, size distribution, composition and morphology. The development of effective colloids requires the evaluation of these properties under relevant solvent conditions. Recent advances in methodology, technology and instrumentation offer the necessary tools for the analysis of colloidal dispersions and self-assembled structures with nanoscopic dimensions.

This chapter describes some of the current methods and instrumentations for characterization of solution-borne structures in their native state. The discussed techniques consist of the following: analytical ultracentrifugation (AUC), small angle X-ray scattering (SAXS), dynamic light scattering (DLS), freeze-fracture and cryogenic transmission electron microscopy (FF- and cryo-TEM). In addition, selected side projects from collaborative work are discussed to demonstrate the versatility and capabilities of these techniques; the investigated systems range from aqueous solutions of small micellar aggregates to complex gel-like materials.

2.1.1 Analytical Ultracentrifugation

Analytical Ultracentrifugation (AUC) is a powerful technique used to characterize macromolecules in solution. It can provide a wide range of information about the thermodynamic and hydrodynamic properties of solutes in the native state, and directly measures their molecular

weights.[2] AUC data is determined by sedimentation analysis which is based on thermodynamics. The thermodynamic parameters in equations that describe sedimentation behavior can all be acquired experimentally.[3]

When Nobel Prize Laureate Theodore Svedberg and co-workers developed the idea for the ultracentrifuge in 1923, it was solely intended for investigating colloidal systems.[4] However, AUC became most popular in the fields of biology and biochemistry. It was the first instrument to yield dependable molar mass values for biopolymers.[5] As technology advanced, new methods such as dynamic light scattering (DLS), size exclusion chromatography (SEC), and electron microscopy (EM) forced the AUC into extinction. In 1991, Beckman redesigned the AUC and introduced it as the Optima XL-A.[6] The new model influenced the rebirth of analytical ultracentrifugation, but the versatility of this method of characterization is seldomly exploited. AUC is a great tool for analyzing associating systems and was essential in the study of porphyrin aggregation in aqueous solution, discussed in Chapter 3.

The two basic types of AUC experiments are sedimentation velocity and sedimentation equilibrium. In principle, sedimentation equilibrium (SE) experiments are capable of providing information about the size of the individual molecules which form complexes, the size of the complex, the strength of subunit interactions and the thermodynamic nonideality of the solution.[3] Sedimentation velocity (SV) experiments can be used to study the molar mass, size distribution, and shape of macromolecules.[7] SE and SV experiments can present complementary information and most studies require the application of both techniques to obtain useful data. For the purposes of the studies herein, only SE experiments were performed and will be further discussed.

2.1.1.1 Instrumentation and Experimental Applications

Ultracentrifugation is based on the application of a centrifugal field, $\omega^2 r$, where ω represents the angular velocity and r is the distance to the axis of rotation. The angular velocity ω (s^{-1}) is $2\pi/60$ multiplied by the number of revolution per minute (rpm), and the maximal speed is 60,000 rpm in the XLA. The radial distance r in the conventional cell is typically in the range of 5.8-7.2 cm (see Figure 2-1). Ultracentrifuge cells are sector-shaped with the walls parallel to the radii of the rotor to minimize convection and prevent sedimenting particles from colliding with the walls (wall effects). It is also important for the cells to be durable and withstand the stresses of exceptionally high gravitational fields. A centrifugal force of up to 300,000 g can be achieved by the rotor system; g is the acceleration due to gravity, 9.81 $m \cdot s^{-2}$. Macromolecules that are exposed to such a great force will redistribute in solution.[8]

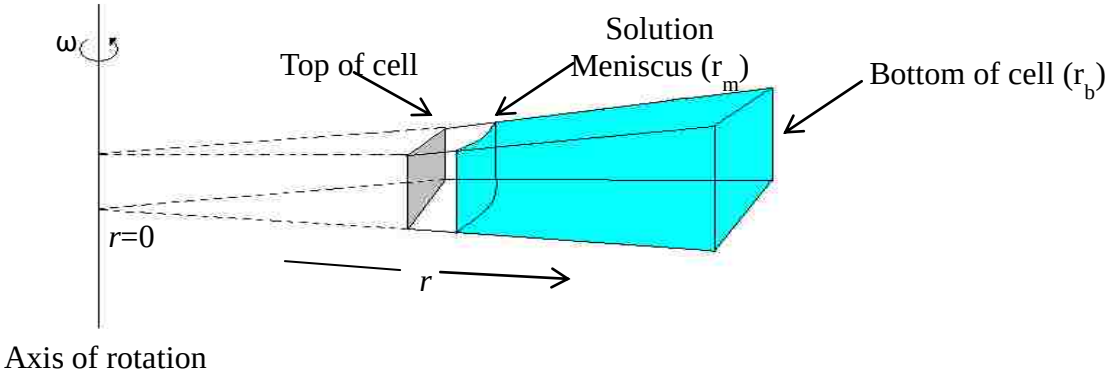

Figure 2-1 Schematic of a sector-shaped ultracentrifuge cell and its radial positions with respect to the axis of rotation corresponding to its position in the rotor.

An analytical ultracentrifuge is identical to a classic preparative ultracentrifuge with respect to their appearance. In fact, the only key component that distinguishes these instruments from one another is the optical system. An analytical device permits the measurement of particle distribution as a function of time via the determination of radial position during

ultracentrifugation.[8] The two types of optical systems used for AU are the Optima XL-A which measures absorption, and XL-I which has supplementary Rayleigh interference optics. The addition of the Rayleigh interference system affords more sensitive optical detection of concentration distributions without the requirement of chromophores.[9]

The Optima XL-A analytical ultracentrifuge uses a xenon flash lamp as the light source, which supplies a wavelength range of 190-800 nm. However, single-wavelength light is selected by a toroidally-curved diffraction grating. Light of other wavelengths are blocked and stray light is minimized by a series of absorbing filters. To account for the fluctuations in light intensity from pulse to pulse, a small amount of incident light from the diffraction grating is normalized by being reflected onto a detector located at an implicit focal point.

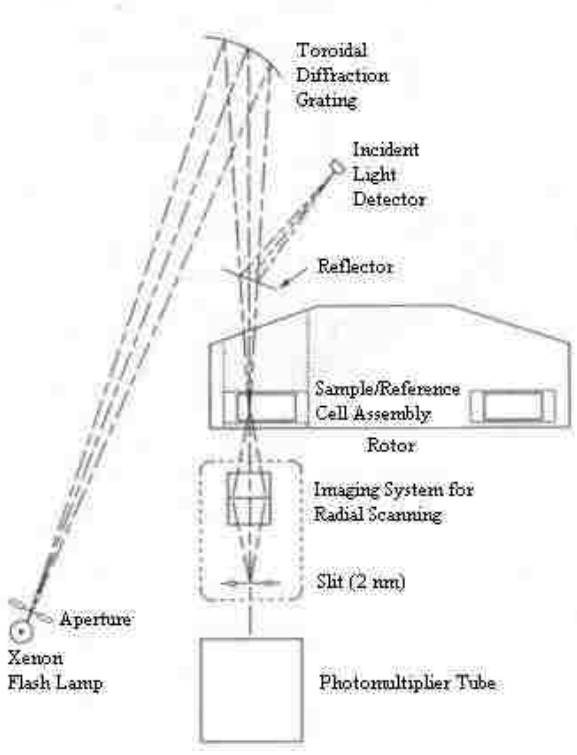

Figure 2-2 Diagram of the Beckman Optima XL-A system. Adapted from reference 10.

As the sample cell passes over the detector, monochromatic light is transmitted through the sector (sample or solvent) of interest. Regulation of the synchronized timing of the light flash (pulse) and rotor precessions is monitored by a reference magnet located in the base of the rotor. The maximum pulse rate is 100 flashes per second; one flash per ten revolutions at 60,000 rpm. The intensity of the transmitted light through the sample sector is measured with reference to the solvent by a photomultiplier tube located beneath the rotor. A lens-slit assembly travels as a unit to provide radial scans of the sectors (see Figure 2-2).[10]

2.1.1.2 Fundamental Principles

The foundation for understanding the theory of sedimentation processes in the ultracentrifuge begins with the derivation of flow (or flux) equations. These equations describe the isothermal mass transport of thermodynamic components in a centrifugal field. A simple kinetic theory approach can be applied to derive a useful flow equation for a system consisting of a homogenous solute and a solvent (binary solution). Such an approach suggests that transport of solute molecules through the solvent is the result of a centrifugal force, a buoyant force, and a diffusion force.[11] On the contrary, as the concept developed, it was noted that the kinetic theory had to be replaced by nonequilibrium (irreversible) thermodynamics in order to obtain the general and rigorous derivation of flow equations for the ultracentrifuge.[12] The simpler mechanical point of view will be described within the scope of this review.

According to Van Holde, most phenomena such as sedimentation and diffusion share a common feature: A system *not* in equilibrium migrates towards equilibrium. In route to equilibrium, it is inevitable for flow to occur. For instance, a molecule moving with a velocity Δv in time Δt across a surface s in an ultracentrifuge cell will travel a distance $\Delta x = v\Delta t$. As a result, every solute molecule within a slab of the cell returning to this distance from the surface s

will pass through s in Δt sec. The amount of molecules passing is the concentration times the slab volume, $\Delta w = Cs\Delta x$, which can also be written as $\Delta w = Csv\Delta t$ (see Figure 2.3). Hence, flow is defined as $J = \Delta w/s\Delta t$.[13] Because of this relation between flow and molecular velocity, the definition of flow can be expressed in simpler terms as

$$J_i = v_i C_i \qquad \text{Equation 2-1}$$

where flow J_i is the uniform concentration C_i of component i crossing 1 cm^2 of surface in 1 sec with a velocity v_i.

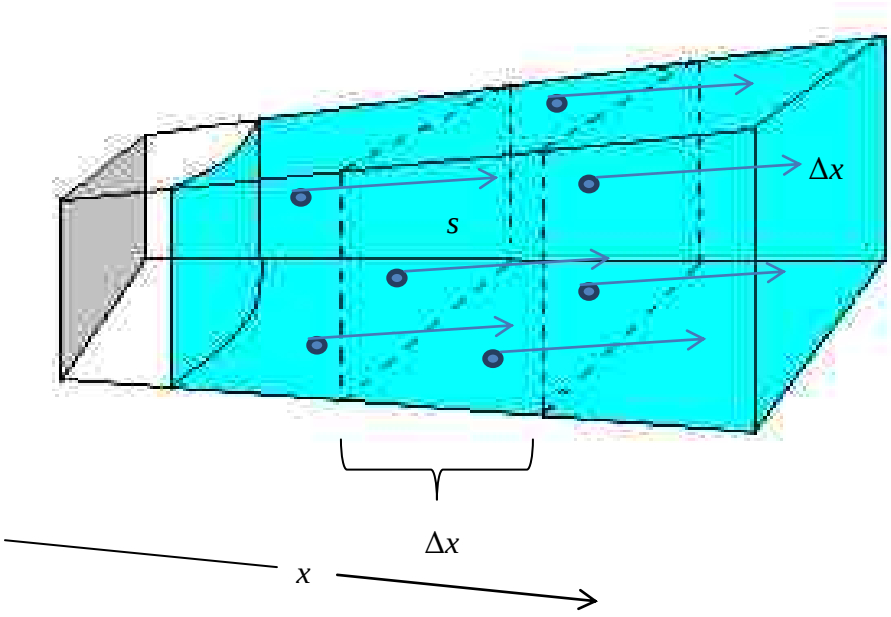

Figure 2-3 Illustration of flow and molecular transport velocity, and their relativity in an ultracentrifuge cell.

The concept of transport processes, with respect to sedimentation, is based on three forces acting on the solute molecules; centrifugal force, buoyant force, and frictional force (see Figure 2-4). For instance, a molecule in solution spinning inside a rapidly spinning rotor with an angular velocity ω, is subjected to a centrifugal force F_c. This force experienced by the molecule is proportional to its mass (m) and distance (r) from the axis of rotation. Therefore, the centrifugal force can be defined as $F_c = \omega^2 rm$. Concurrently, a counter force is produced as a result of the

molecule displacing some solution, inducing a buoyant force $F_{buoy} = -\omega^2 r m_0$; where m_0 is the mass of the displaced solution. Lastly, as the molecule flows with a velocity v as a result of the previously mentioned forces, it incurs a viscous drag from the solvent. The drag causes the molecule to resist its flow through solution. This resistance is the frictional force F_d and is expressed as $F_d = -fv$, where f is the frictional coefficient.[13]

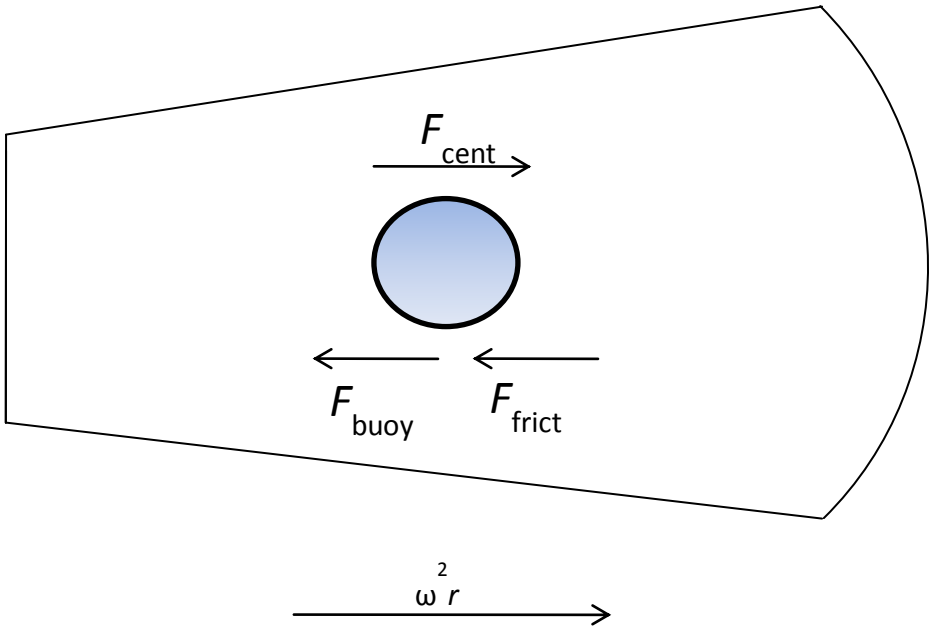

Figure 2-4 Illustration of the forces experienced by a particle inside a sector-shaped cell during subjection to a centrifugal field.

Sedimentation equilibrium experiments use an angular velocity comparable to the forces of diffusion which prevents the macromolecules from completely sedimenting to the cell bottom. This approach distributes the molecules in a stable concentration gradient along the radial dimension of the cell. Knowledge of the thermodynamic terms involved in the sedimentation transport process can be used to derive information about the molecular weights, states of aggregation, and association constants of macromolecules in solution.[14]

2.1.1.3 Determination of Average Molecular Weight

Most techniques used for obtaining molecular weights of polymeric materials are not capable of yielding accurate values when detecting heterogeneity. However, the analytical ultracentrifuge is able to overcome such a limitation. In fact, the AU is most renowned for its ability to combine measurements of sedimentation and diffusion coefficients for the determination of molecular weights. When sedimentation and diffusion reaches a state of equilibrium, in theory, apparent movement of the solute no longer occurs; it is maintained as long as the rotor speed and temperature are held constant. Based on the Lamm equation, the equilibrium concentration distribution (c_r) is a function of the buoyant molecular weight, $M(1-\bar{\nu}\rho)$; angular velocity, ω^2; and temperature, T in Kelvin.[15]

$$\frac{\ln(c_r)}{r^2} = \frac{M(1-\bar{\nu}\rho)\omega^2}{2RT} \qquad \text{Equation 2-2}$$

where M is the monomer molar mass, $\bar{\nu}$ is the partial specific volume, ρ is the density of the solvent, and R is the gas constant. As a result of the concentration distribution being dependent on the buoyant molecular weight, accurate values of the $\bar{\nu}$ and ρ are imperative for determining the molecular weight using the SE method.

For an ideal system, a ln(c_r) vs r^2 plot yields a straight line with a slope proportional to M (see Figure 2-5). In the case of an associating system, such as the self-assembly of porphyrin aggregates, the plot is not capable of yielding a straight line; requires more intense analysis. The plot tends to curve upward when the sample material undergoes aggregation. This same curvature can also occur when there is a mixture of materials of varying molecular weights or the sample experiences degradation.[16] When the plot curves downward, it indicates the solution being non-ideal. The tangents to the curve of a nonlinear ln(c_r) vs r^2 plot yields the weight-average molecular weight for the varying species at each radial position.[15]

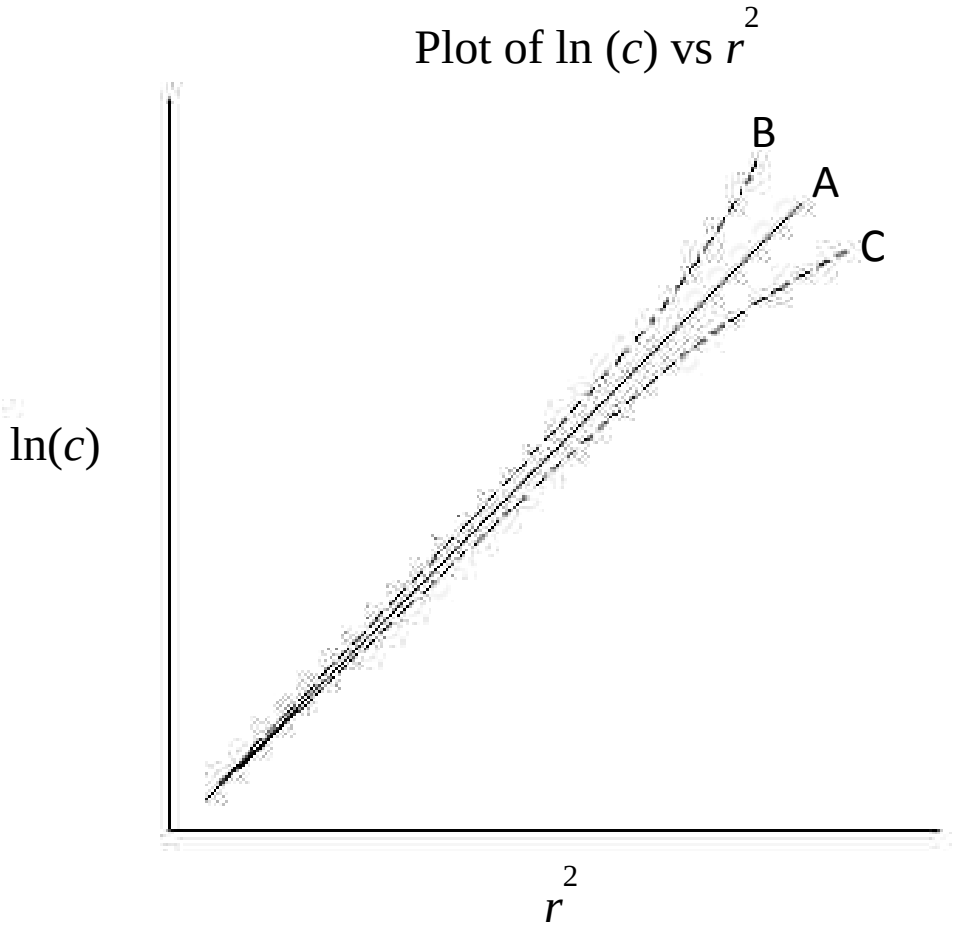

Figure 2-5 Plot of ln(c) vs r^2 showing curves from an (A) ideal solution (homogeneous); (B) polydispersed (heterogeneous) solution; and (C) non-ideal solution.

2.1.2 Small Angle X-ray Scattering (SAXS)

The aim of scattering experiments is to determine the structure and organization of "particles" dispersed in solution. In this case, the generic term "particle" refers to dispersed matter, such as colloids, macromolecules, micelles or aggregates in a solvent.[17] Small angle scattering (SAS) is a common technique for examining structures in the range of 10 Å or larger.[18] This method can render structural information directly from systems possessing density inhomogeneities. Moreover, the ability to analyze the inner structure of disordered systems is the most captivating feature of the SAS method.

The sources of radiation that can be used for SAS include light, x-rays, and neutrons. Each source has advantages and disadvantages, depending on the sample. For instance, particles in the size range of 5 to 300 Å can be explored by small angle X-ray or neutron scattering experiments, whereas light scattering is useful for particles in the range of 100 to 3000 Å.[17] However, light scattering is not capable of examining optically opaque samples and x-ray scattering exhibits difficulties in studying thick samples. Neutrons are electrically neutral particles, and therefore is capable of penetrating anything but can induce energy transfer effects due to neutrons interacting with the nucleus itself. Although these scattering techniques offer different features, each one essentially provide complementary information.[3]

X-rays are electromagnetic radiation which interacts with electric charges in matter.[4] The occupied wavelength of x-rays range from approximately 10^{-2} to 10^{2} Å. The electromagnetic radiation of X-rays used to study materials occupies the range of 0.5-2.5 Å in wavelength. This angular range contains information about the shape and size of macromolecules, characteristic distances of partially ordered materials, pore sizes, and other data.[5]

2.1.2.1 Fundamental Principles

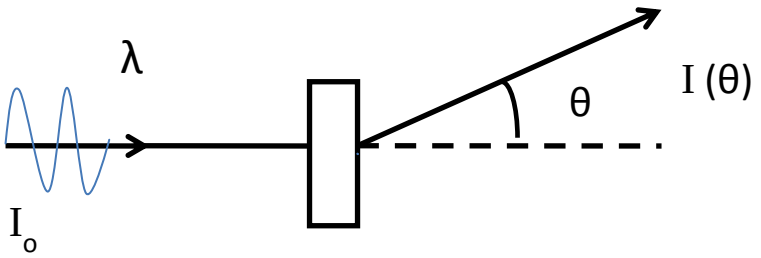

Figure 2-6 Schematic of general scattering experiment measuring the variations in intensity as a function of θ (scattering angle).

Scattering experiments involve emitting well-collimated radiation of wavelength λ through a sample and measuring the variations of the intensity as a function of the scattering angle θ.[1] (See

Figure 2-6) Upon interaction, coherent scattering patterns are generated from electron density inhomogeneities within the particle system.

The scattering vector, *q*, is the parameter that characterizes the scattering geometry and is written as

$$q = \frac{4\pi}{\lambda} \sin \frac{\theta}{2} \qquad \text{Equation 2-3}$$

where λ is the wavelength of the radiation source. The magnitude of *q* is related to the scattering angle *θ*, which is the angle between the incident beam and detector. The unit for q is inverse wavelength ($Å^{-1}$).

Scattering processes are based on a law of reciprocity. A scattering curve *I*(*q*) can be produced for a particle of any shape by Fourier inversion of the pair-distance distribution function, *p*(r), where *r* is the distance between two scattering centers inside the particle.[19] In relation to the equation $q = 2\pi/d$, scattering vector *q* corresponds to reciprocal space and is inversely proportional to the distance *d* between scattering pairs in real space. By exploiting these parameters, a plethora of structural detail and information can be obtained from the scattering curve using various plots for analysis.

2.1.2.2 Scattering of Dilute Particulate System

In the dilute particulate system, individual particles of one material are uniformly dispersed in a matrix of a second material. For adequately dilute concentrations, the individual particles are positioned far apart from each other and as a result, are uncorrelated. The scattered waves from these different particles will be incoherent. Due to the lack of phase coherence, the overall intensity is basically the sum of the intensities of independently scattered rays from individual particles.[4]

The SAXS intensity, $I(q)$, provides information about the size and shape of the particles and can be represented by

$$I(q) = k\, N_p\, P(q)\, S(q)\,, \qquad \text{Equation 2-4}$$

where k is the calibration factor, N_p is the scattering particle number density, $P(q)$ is the particle form factor, and $S(q)$ is the structure factor. For dilute systems, the structure factor is negligible ($S(q) \approx 1$) and the measured scattering cross section only depends on the particle form factor $P(q)$.[6]

When studying dilute solutions via SAXS, it is advantageous to use a strong synchrotron source. A synchrotron is capable of accelerating a beam of electrons to virtually the speed of light. The flux of x-rays emitted is far greater than that obtained with conventional x-ray tubes, which minimizes the acquisition time for any single measurement.[4]

2.1.2.3 Determination of Radius of Gyration

In terms of dilute polymer solutions, small angle x-ray scattering can be expressed as

$$\frac{KC}{I(q,C)} \approx \frac{1}{M_w}\left(1 + \frac{q^2\langle {R_g}^2\rangle}{3}\right) + 2A_2C \qquad \text{Equation 2-5}$$

where K is the instrument constant related to the electron density; C is the concentration of the polymer in solution; A_2 is the second virial coefficient; and $\langle {R_g}^2\rangle^{1/2} \equiv R_g$ is the radius of gyration. If K is known, the scattering data can be analyzed using a Zimm plot to determine R_g and A_2 by a simultaneous extrapolation to $q = 0$ and $C = 0$, respectively.[7]

The radius of gyration of a scattering body can also be estimated simply from the slope of the linear region of the Guinier plot [ln ($I(q)$) vs. q^2]; the initial slope gives $R_g^2/3$. Even if the shape of the particle is unknown or irregular, the scattering function still obeys the expression

$$I(q) = \rho_0^2 v^2 \exp\left(-\frac{1}{3}q^2R_g^2\right) \qquad \text{Equation 2-6}$$

where $I(q)$ is the independent scattering intensity by a particle; ρ_o is the average scattering length density in the particle; and υ is the particle volume. Equation 2-6 is referred to as the Guinier law. The validity of the Guinier approximation is limited to scattering angles where q is sufficiently smaller than $1/R_g$. In addition, the system must be dilute to observe independent scattering from the particles and the solvent has to be of constant density.

2.1.3 Dynamic Light Scattering (DLS)

Dynamic light scattering (DLS), also referred to as quasi-elastic light scattering (QELS) and photon correlation spectroscopy (PCS), is a non-invasive technique for measuring the size and size distribution of particles or molecules typically in the submicron range. The latest technology (e.g., faster detectors) permits the size characterization of molecules smaller than 1 nanometer.

DLS measures the light that is scattered by emulsions, dissolved (macro)molecules or colloidal dispersions; a continuous wave laser is the most common used light source. Due to the exhibited Brownian motion of suspensions, fluctuations of the scattering intensity can be observed. This random movement of particles occurs as a result of their bombardment by surrounding solvent molecules. Consequently, the constant changing particle positions cause the total scattered electric field at the detector to fluctuate in time. Implicit information regarding the structure and dynamics (e.g., position and orientation) of the molecules is found within these fluctuations. For instance, the rate at which the intensity of the scattered light fluctuates is dependent upon the size of the particles (see Figure 2-7). The Brownian motion of larger particles is slower than that of smaller particles. Therefore, the velocity of particle motion corresponds to their translational diffusion coefficient D_t. This relationship still remains ambiguous until a correlator is incorporated for the extraction of meaningful information.

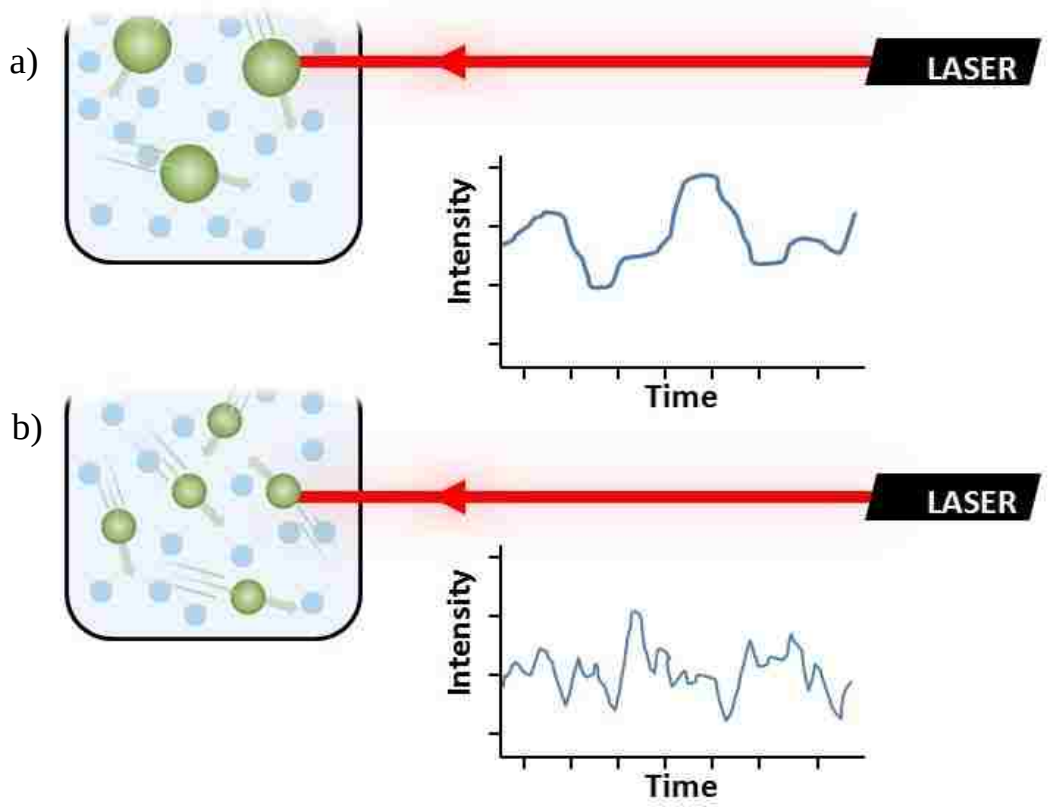

Figure 2-7 Hypothetical intensity fluctuations for (a) large and (b) small particles exhibiting Brownian motion.

A correlator is used to generate quantitative information from the aforementioned scattering intensity fluctuations. The correlation function provides a concise method for expressing the degree to which two intensity fluctuations, *I(t')* and *I(t'+ t)*, are correlated over a period of time *t*. In other words, it approximates how long a given signals stays the same. The autocorrelation function of the scattered light intensity is expressed as:

$$G^{(2)}(t) =< I(0)I(t) >= \lim_{T\to\infty} \frac{1}{2T}\int_{-T}^{T} I(t') \cdot I(t'+t)dt' \qquad \text{Equation 2-7}$$

Here, the capital *G* is an indication that the data are *not* normalized and the $^{(2)}$ superscript indicates that $G^{(2)}$ is a second-order autocorrelation function. Assuming the scattering is a random Gaussian process and homodyne ("self-beating" technique), the Siegert equation relates

the second-order autocorrelation function with the electric field autocorrelation function $g^{(1)}(t)$ as follows:

$$G^{(2)} = B(1 + f\left|g^{(1)}(t)\right|^2) \quad \text{Equation 2-8}$$

where B and f are experimental parameters. Specifically, the parameter B is a baseline, which is proportional to the square of the average scattering intensity. The component f is the coherence parameter ($0<f<1$) and it is chosen at the beginning of the experiment by adjusting optical settings (e.g., change pinhole or aperture size).

2.1.3.1 Determination of Hydrodynamic Radius

Using the following equations, one can calculate the hydrodynamic radii (R_h), as well as the mutual diffusion coefficient D_m of particles. The electric field autocorrelation function $g^{(1)}(t)$, contains information from its distribution of the relaxation rate which can give details about molecular size. In many cases, the decay is that of a single exponential and can be expressed as:

$$g^{(1)}(t) = e^{-\Gamma t} \quad \text{Equation 2-9}$$

where Γ is the decay rate. The decay rate is related to the apparent mutual diffusion coefficient by:

$$D_{app} = \frac{\Gamma}{q^2} \quad \text{Equation 2-10}$$

where q is the scattering vector, $q = (4\pi n/\lambda)\ sin(\theta/2)$, n is the refractive index of the solution and the scattering angle is 2θ. For simple translational diffusion, the apparent mutual diffusion coefficient D_m is used to reveal the apparent hydrodynamic radius, $R_{h,app}$ via the Stokes-Einstein equation:

$$Rh, app = \frac{kT}{6\pi\eta_o D_o} \quad \text{Equation 2-11}$$

where k is Boltzmann's constant, 1.38×10^{-16} g·cm^2·s^{-2}·K^{-1}, T is the temperature in Kelvin, and η_o is the solvent viscosity. The calculated hydrodynamic radius of a particle is the effective radius of an irregular shaped particle or molecule in a fluid. For a spherical object, the hydrodynamic radius is equal to the actual radius of the sphere ($R_h = R$) (see Figure 2-8). In contrast, a non-spherical object, such as a polymer chain, R_h is the radius of a hypothetical sphere with the same diffusion coefficient.

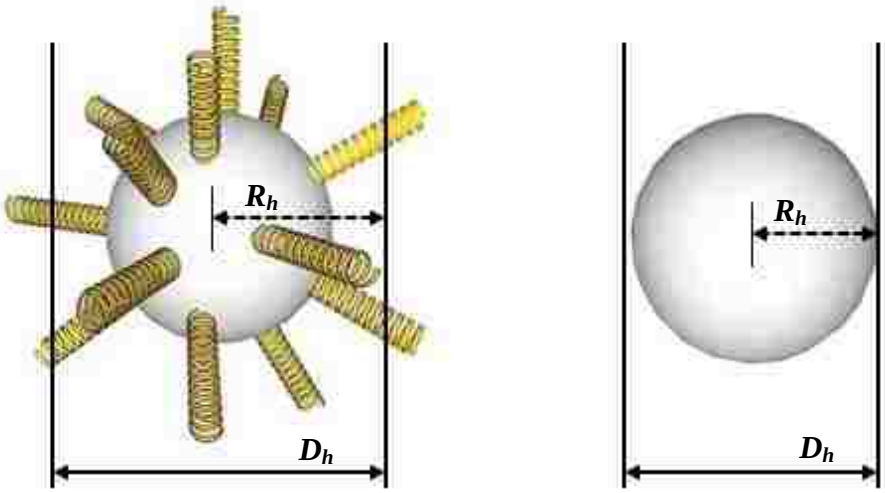

Figure 2-8 Illustration of the hydrodynamic radius R_h and diameter D_h of a polymer-coated sphere and a bare solid sphere.

2.1.3.2 Analysis of Polydispersed Systems

In many cases, samples are typically polydispersed, which requires the analysis of a distribution of Γ values. The previously discussed method of size characterization is not suitable for such systems. Two useful methods for the evaluation of polydispersed samples involve cumulant expansion and CONTIN analysis.

Cumulant expansion assumes a Guassian-like distribution of the particles, which is centered about the mean. The treatment below follows the development of Jirun Sun. From the normalized distribution function $G(\Gamma)$, one can determine the integral sum of decay curves with the following expression:

$$\left|g^{(1)}(t)\right| = \int_0^\infty G(\Gamma)e^{-\Gamma t}d\Gamma \qquad \text{Equation 2-12}$$

and $\int_0^\infty G(\Gamma)d\Gamma = 1$; therefore, the sum of exponential decay functions can be re-written as a power series expansion:

$$\left|g^{(1)}(t)\right| = \int_0^\infty G(\Gamma)e^{-\Gamma t}d\Gamma = e^{\bar{\Gamma}t}\int_0^\infty G(\Gamma)e^{-(\Gamma-\bar{\Gamma})t}d\Gamma \qquad \text{Equation 2-13}$$

$$= e^{-\bar{\Gamma}t}\int_0^\infty G(\Gamma)\left[1-(\Gamma-\bar{\Gamma})t+(\Gamma-\bar{\Gamma})^2\frac{t^2}{2!}+\cdots\right]d\Gamma \qquad \text{Equation 2-14}$$

where the mean Γ is represented by

$$\bar{\Gamma} = \int_0^\infty \Gamma G(\Gamma)d\Gamma \qquad \text{Equation 2-15}$$

The moments of the distribution are defined by

$$\mu_n = \int_0^\infty G(\Gamma)(\Gamma-\bar{\Gamma})^n d\Gamma \qquad \text{Equation 2-16}$$

$$\left|g^{(1)}(t)\right| = e^{-\bar{\Gamma}t}(1+\frac{\mu_2}{2!}t^2-\frac{\mu_3}{3!}t^3+\frac{\mu_4}{4!}t^4+\cdots) \qquad \text{Equation 2-17}$$

Using the Taylor series expansion:

$$\ln(1+x) = x-\frac{x^2}{2}+\frac{x^3}{3}-\frac{x^4}{4}+\cdots,(-1<x<1) \qquad \text{Equation 2-18}$$

Substitution of the corresponding *x* terms yields the following expression:

$$ln\left|g^{(1)}(t)\right| = -\bar{\Gamma}t+\frac{\mu_2}{2!}t^2-\frac{\mu_3}{3!}t^3+\cdots \qquad \text{Equation 2-19}$$

Here, the coefficients represent the cumulants which describe some of the Γ distribution properties. This quantity can also be used to determine the polydispersity index (PDI) with the dimensionless quotient $\mu_2/\bar{\Gamma}^2$. A monodisperse sample has a PDI of zero. If the parameter $\mu_2/\bar{\Gamma}^2$ is greater than 0.3, the sample is considered polydispersed and require another method for data analysis.

The software program CONTIN[20] offers an alternate method of analyzing data for polydispersed samples. This Fortran-based program, written in the 1980's by Stephen Provencher, performs automated inverse Laplace transforms to fit data. Using three types of

strategies, the program seeks the optimal fit. The strategies include: 1.) limit information (i.e., be content with the mean value); 2.) impose inequality constraints by prior knowledge (i.e., non-negative $G(\Gamma)$; 3.) parsimony or regularization (i.e., acquire the smoothest or simplest solution). The advantages and limitations of this application are demonstrated later in the chapter.

2.1.4 Transmission Electron Microscopy (TEM)

The rapidly growing areas of nanotechnology and (macro)-molecular self-assembly have led to a strong interest and continuous demand for nanoscopic imaging techniques. Scanning-probe techniques, such as atomic force microscopy (AFM) and scanning tunneling microscopy (STM), are important tools for imaging surface-associated structural details.[21] For the visual analysis of nanostructures *in situ*, transmission electron microscopy (TEM) is a preferred technique. Depending on the details of interest, one can choose specific sample preparation methods for TEM. For instance, the negative staining method is a procedure which uses a salt solution containing strongly electron scattering heavy metal salts (e.g. uranyl acetate) to stain the sample for enhanced contrast in the electron microscope. Once the stained sample has dried on the EM grid, it can be viewed. Due to the simplicity and minimal time-consumption of this preparation, it is the most commonly used technique. Although negative staining is the easiest routine for visual structure analyses, high resolution images are typically unattainable.[22] Also, staining as well as drying, may alter the structure and morphology of the sample. The drying of suspensions exposes structures to the surface tension of the solvent, and the retracting liquid surface tends to sweep them into clusters or agglomerates.[21] Therefore, extreme caution should be taken in the interpretation of the electron micrographs. Figure 2-9, shows TEM images of curcumin–rubusoside nanoparticles (see Section 2.3), prepared using the negative staining method.

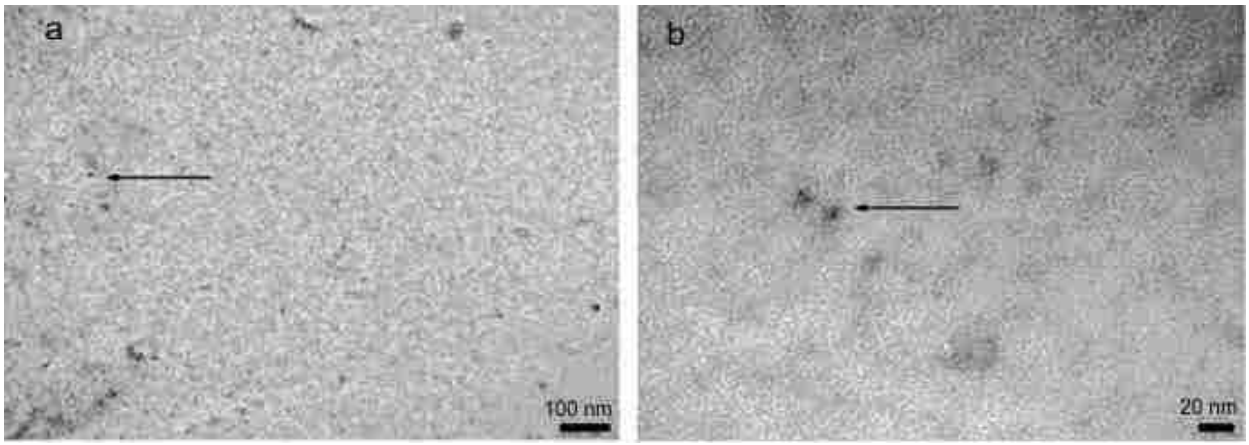

Figure 2-9 TEM images of curcumin– rubusoside nanoparticles in 10% rubusoside-solubilized curcumin water solution, negatively stained with uranyl acetate. Images were captured at (a) direct magnification 120,000×; and (b) direct magnification 400,000×. The arrow indicates one of the nanoparticles from the 10% rubusoside-solubilized curcumin water solution. Adapted from ref 22.

The following sections of this review highlights cryofixation techniques often used for the imaging of aqueous systems. The two distinct methods include freeze-fracture electron microscopy (FF-EM) and cryo- electron microscopy (cryo-EM), which are both powerful for observing the structural features of solvent-borne samples in their native environment.

2.1.4.1 Freeze-Fracture TEM

In 1950, Hall[23] and Meryman[24] introduced the combination of freezing and etching (sublimation of ice to reveal surface structures). The practice of fracturing frozen specimen was later used by Meryman and Kafig[25] in 1955. This newly developed technique attracted general interest in the 1960s, particularly when Moor et al.[26] reported remarkable TEM images of freeze-fractured yeast cells.[27] In 1961, Moor and coworkers[28] improved the freeze-fracture procedure via the use of a vacuum evaporator with a precision microtome for fracturing. The first commercially available freeze-fracture equipment was manufactured by Balzer AG Liechtenstein in 1965; this apparatus was modeled after the design of Moor.

The freeze-fracture technique is a useful method for imaging structures in solution. It is most often performed for aqueous systems; however, freeze-fracture is also applicable for other systems, assuming the solvent can be vitrified (rapidly frozen). The process only requires a drop of sample, applied to a gold planchette (stub), followed by vitrification. Under vacuum and cryogenic temperatures, the vitrified samples are fractured across a horizontal plane with a cold knife. Increasing the internal temperature of the vacuum chamber promotes etching of the fractured sample. The etching process enhances contrast as a result of more sample exposure when a small amount of the supporting matrix (vitrified solvent) is removed. The deposition of platinum (Pt), along with a reinforcement layer of carbon yields a replica of the sample that can be viewed via TEM. The Pt is typically deposited at a 45° angle to create a dark shadow, which provides the necessary contrast for image interpretation. In Figure 2-10a, the cross-section of a hypothetical frozen suspension of particles is fractured. The etched sample undergoes Pt-C deposition, as depicted in b) and forms the resulting replica c) of the fractured surface. In the TEM, areas of the replica with the most Pt deposited will block the most electrons, which cause it to appear darkest. The lighter areas have less Pt due to the protruding structures blocking the Pt during deposition, which casts a white "shadow". Distinct topographical details are revealed through these variations along the fractured plane.

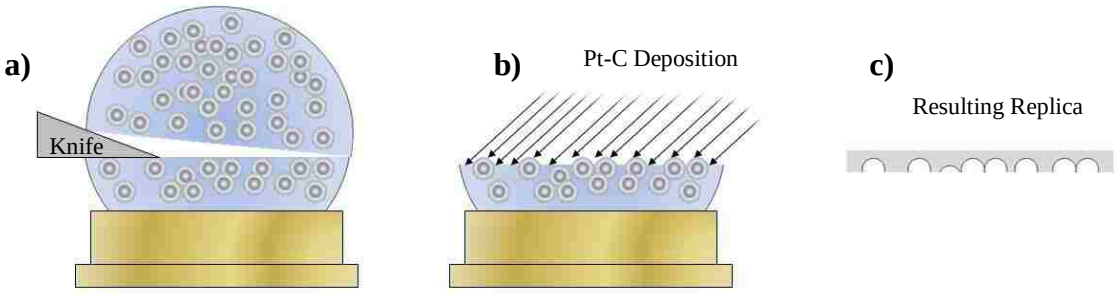

Figure 2-10 Schematic depiction of sample replication during the freeze-fracture process. a) The vitrified sample is fractured with a microtome knife, and then b) Pt-C is deposited at an angle θ of 45˚ after etching. c) The resulting sample replica is viewed in the electron microscope after washing.

The acquired replica may exhibit different types of fracture outcomes depending on the proximity of the microtome knife, with respect to the vitrified structures during fracturing. These possible outcomes include: concave fracture, convex fracture, and cross-fracture. Concave fractured objects usually appear light to dark in contrast and the shadow remains within the structure cavity. Convex fractured objects are dark to light, where the shadow often extends outside the boundaries of the structure. Cross-fractured objects are uniform in contrast and display practically no shadowing. When evaluating such replicas, it is important to know the composition and expected structure of the sample to accurately interpret the TEM image.

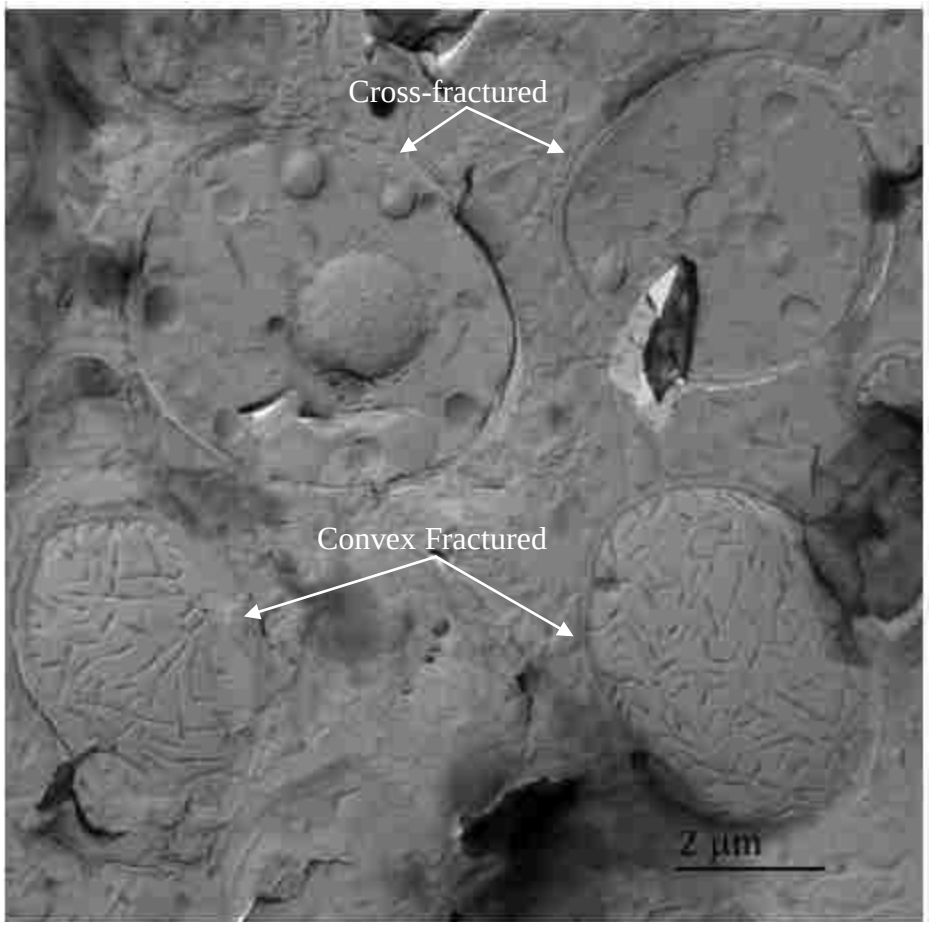

Figure 2-11 FF-TEM image of yeast cells. The two cells at the top were cross-fractured through the yeast cell while the bottom two were convex fractured through the cell wall. Adapted from reference 29.

Figure 2-11 shows an FF-TEM image of yeast cells which illustrates, both, convex and cross-fractures. Two of the cells are cross-fractured, exposing the intercellular components, and the bottom two cells are convex fractured. Clearly visible in the upper left cell is the nucleus, several vacuoles, and the cell wall of the yeast. The bottom two cells show the inner structures of the cell wall with rod-like indentions in the protoplasm face.[29] This type of intricate detail provides valuable information and is often complemented by techniques such as cryogenic-TEM.

2.1.4.2 Cryogenic TEM

Cryogenic transmission electron microscopy (cryo-TEM) specimens are prepared without chemical treatment and permits direct visualization of the sample without replication. In comparison to FF-EM, Cryo-EM has a slightly higher resolution (~2nm for periodical structures) and permits the analysis of the inner volume of various specimens.[30] Generally, a microliter drop of sample is applied to a holey carbon-coated TEM grid, blotted with filter paper and plunged quickly into liquid ethane at -183 ˚C. Blotting reduces the sample about 5000 times in volume, yielding a thin film with a thickness of approximately 100 nm. Similar to freeze-fracture, the solution (usually aqueous) is vitrified due to the fast cooling rates which occur during plunge freezing. Vitrification preserves supramolecular structures such as micelles and liposomes because the rearrangement of water molecules during ice crystal formation is mostly prevented.[31] Contrary to the freeze-fracture process during freezing, the nanostructures of interest instantly become embedded in an electron-transparent film of amorphous ice. The use of phase-contrasting imaging eliminates the need for staining agents and the aqueous specimens can be observed in their near-native hydrated state.

Cryo-TEM also permits the imaging of non-aqueous solutions; however, compared to aqueous solutions, the conditions for sample preparation and image collection are more critical.[21]

With this technique, the vitrified specimen is subsequently observed via electron microscopy at temperatures low enough to prevent recrystallization of the amorphous film. Figure 2-12 shows the specialized equipment which makes the process feasible. Using pre-cooled tools while under

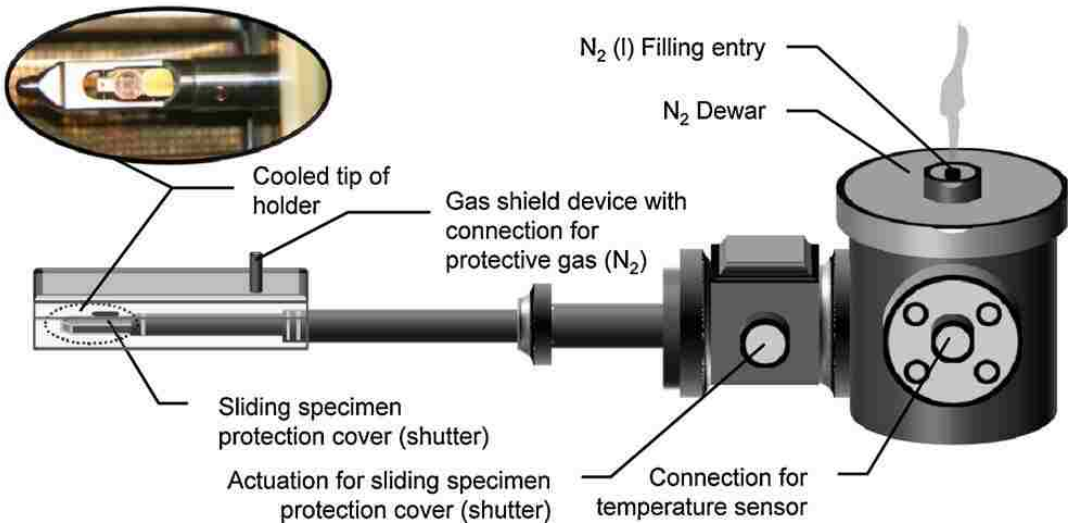

Figure 2-12 Sketch of a sample holder with integrated supplementary functions for use in cryo-TEM investigations. The photograph shows the tip of an Oxford CT-3500 cryo-holder for a Zeiss Leo 922 Omega TEM with open shutter and inserted grid. Adapted from reference 30.

cooling conditions, the TEM grid with the vitrified sample is removed from the liquid ethane storage container and immediately transferred into a cold cryo-holder inside liquid nitrogen. Subsequently, the cooled holder is quickly transferred and inserted into the electron microscope. Collectively, sample vitrification, insertion of the sample into the holder and transfer of the holder into the microscope should be done within a few minutes to avoid contamination with cubic ice or variations in temperature.[30]

The projection images of cryo-TEM can yield information about the shape and internal structure/content of a specimen. Consequently, self-assembled carrier systems (e.g., liposomes) are often investigated using this technique. Liposomes are promising drug delivery vehicles and

attractive membrane models to study transport processes[32]. Shown in Figure 2-13, is a cryo-TEM image of rhodamine dye-encapsulated liposomes. Due to the relatively high contrast of the

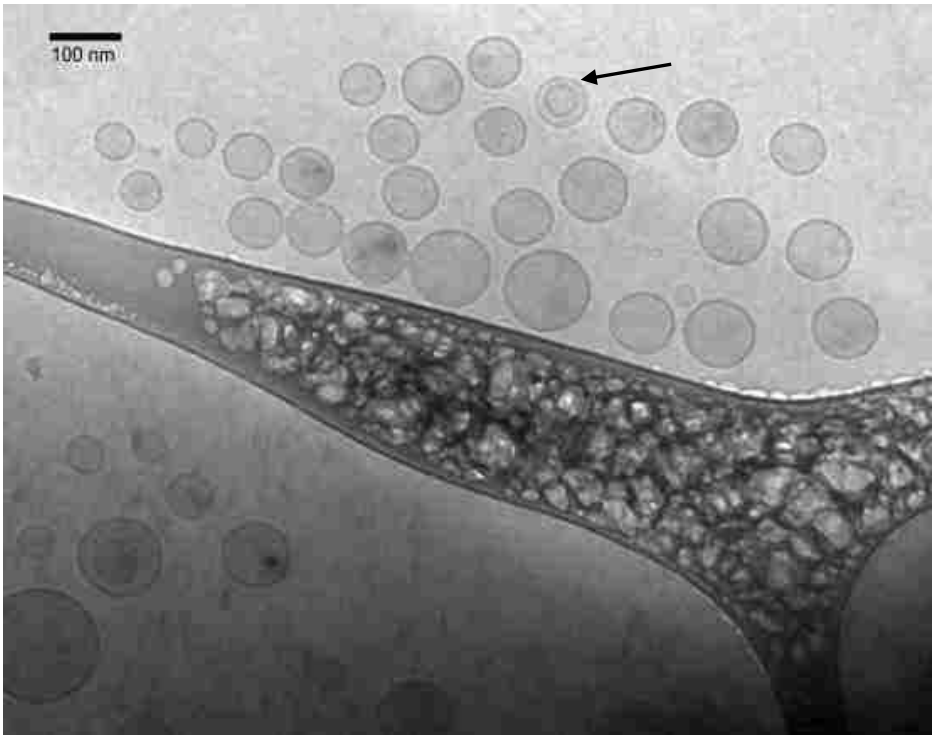

Figure 2-13 Cryo-TEM image of rodhamine dye-encapsulated liposomes. The image suggests a low loading effiency and broad size distribution. A bilamellar vesicle is indicated with an arrow. The liposome formulation was prepared by Loice Ojwang.

phospholipid bilayer, liposomes appear as characteristic ring-like structures. Therefore, the lamellarity of liposomes can be determined by cryo-TEM. For instance, preparation methods such as extrusion usually results in unilamellar vesicles, but sometimes bi- or oligolamellar vesicles are observed.[30] The arrow in Figure 2-13 indicates a bilamellar vesicle in the mixture. Similar to the studied liposomes, cryo-TEM plays a major role in the elucidation of many other *in situ* self-assembled structures, as will be seen in the following chapter.

2.2 Experimental

2.2.1 Materials and General Considerations

Acetonitrile, methanol, and water were of HPLC grade (Mallinckrodt Baker Inc., Phillipsburg, NJ). Formic acid (98%) was of HPLC grade (Sigma-Aldrich Co., St. Louis, MO). Normal saline solution was purchased from Phyto Technology Laboratories (Shawnee Mission, KS). Simulated gastric fluid and simulated intestinal fluid were purchased from RICCA Chemical Co. (Arlington, TX). Curcumin with purity of 96.4% was purchased from Chromadex Inc. (Irvine, CA) and with approximately 90% purity from Cayman Chemical (Ann Arbor, MI). Rubusoside was isolated from *Rubus suavissimus* S. Lee (Rosaceae) in our own laboratory and structurally elucidated by NMR and MS analyses. The purity of rubusoside was determined to be > 98% by HPLC-UV. Uranyl acetate was purchased from TED PELLA Inc. (Redding, CA). DMSO was of analytical grade (Fisher Scientific Inc., Fair Lawn NJ). 3-(4, 5-Dimethylthiazol-2-yl)-5-(3-carboxymethoxyphenyl)-2-(4-sulfophenyl)-2H-tetrazolium (MTS) solution and phenazine methosulfate were purchased from Promega Co. (Madison, WI).

2.2.2 Sample Preparation

2.2.2.1 Preparation of Curcumin Formulation

Appropriate amounts of rubusoside and curcumin (Cayman Chemical) were weighed into a 200-mL glass bottle in three replicates. Then, 20 mL of water was added to each bottle and vortexed slightly to form a suspension solution. The suspension was homogenized at 8,000 rpm for 10 minutes on a homogenizer (Virtis Sentry microprocessor homogenizer, Virtis Co., Gardiner, NY) to form an emulsion. The emulsion was subjected to an autoclave at 250 °F for 60 min (Tuttnauer 3870M manual autoclave, Heidolph Brinkmann LLC., EIK Grove Village, IL). All samples were kept in an incubator at 25 °C for 24 hrs. Subsequently, each was subjected to a

final step of filtration with a 0.45 μM nylon filter. All solution samples were protected from light by aluminum foil and kept at room temperature prior to HPLC and pH (pH meter, Fisher Scientific Inc., Pittsburgh, PA) analyses. The concentrations of curcumin were determined using a serial of curcumin standard solutions in methanol between 10 and 3000 μg/mL. The concentrations of rubusoside were determined using a serial of rubusoside standard solutions in water between 10 and 100 mg/mL.

2.2.2.2 Preparation of Multivalent Protein Droplets

For titrations monitored by dynamic light scattering, samples contained 170 μM $SH3_5$ (850 μM module concentration) plus PRM proteins at concentrations affording PRM:SH3 module ratios between 0 and 5. Droplets were formed in all relevant samples by centrifugation (16,000 g, 10 minutes) before analysis. For analyses of the $SH3_5$+PRM(N-WASP)$_8$ and $SH3_5$+PRM_5 droplets, DLS data were collected using a flat-bottom sample cell.

2.2.3 Dynamic Light Scattering

Particle size measurements were performed using a custom-built apparatus (Paul S. Russo and Mark Delong, Louisiana State University) equipped with a Coherent Innova 90 argon (400-800 nm) laser set to 568.2 nm. A Pacific Precision Instruments wide-range photometer/ preamplifier/ discriminator drives an ALV pulse shaper, which feeds an ALV-5000 digital autocorrelator. The samples were transferred into clean cells via 0.22 μm Durapore Membrane filters. The temperature was controlled at 25.0ºC by a circulating water bath. Each sample was run 5 times at 90º scattering angle with durations of 180s. The averaged data was analyzed with one-exponential and third-order cumulant algorithms to determine the apparent hydrodynamic diameter, D_h.

2.2.4 Transmission Electron Microscopy

2.2.4.1 Negative Staining Method

The surface morphology of the structure between curcumin and rubusoside was studied using transmission electron microscopy (TEM). An aliquot (2 μL) of 10% w/v rubusoside water solution was placed on a 400 mesh carbon-coated copper grid. The sample was allowed to stand for 15-30 sec and removed of excess solution by blotting. The samples were then negatively stained with 5% (w/v) uranyl acetate for 4 min and allowed to dry. The samples were visualized under a TEM (JEOL 100-CX, *JEOL* Inc., Peabody, MA) operated at 80 kV.

2.2.4.2 Freeze-Fracture TEM (FF-TEM)

Freeze-fracture replicas were prepared by first depositing a drop of sample onto a copper planchette (purchased from BAL-TEC). The sample was frozen by rapid immersion into a liquid Freon (SHUR/Freeze^{TM} Cryogen Spray, purchased from Triangle Biomedical Sciences) bath, then plunged in liquid nitrogen. The vitrified sample was transferred to the sample stage, which was submerged in liquid nitrogen. After transferring the sample stage into the freeze-etching chamber of the Balzers BAF-400 apparatus, the samples were fractured at a temperature of -110 °C. Once the fractured sample was allowed to etch for ~1 min., Pt–C was deposited at a 45° angle with respect to the sample surface followed by deposition of C at a 90° angle for reinforcement. The resulting replicas were washed twice in distilled water to remove the actual sample. The replicas were collected on 400 mesh Formvar-coated grids (purchased from Electron Microscopy Sciences) and allowed to dry overnight. TEM observations were performed with a JEOL JEM-100CX transmission electron microscope operated at 80 kV.

2.2.4.3 Cryogenic TEM (Cryo-TEM)

A drop (2-5 μL) of sample was deposited onto a holey carbon grid. The droplet of sample was blotted to make a thin film (<200 nm) across the grid holes and then vitrified by quickly plunging the grid in liquid ethane (~ -170 ºC). Liquid ethane was prepared by supplying a flow of ethane gas into a liquid nitrogen bath. Once in an amorphous state, the sample was then transferred to a cold stage (Oxford Instruments CT3500J) to preserve the microstructures. Using phase contrast microscopy, the prepared samples were observed on a JEOL 1200EX transmission electron microscope.

2.3 Characterization of Micelle Self-Assembly: A Novel Solubility-enhanced Curcumin Formulation for Anti-Cancer Treatment[1]

2.3.1 Background and Rationale

Curcumin (CUR; Figure 2-14) is a natural compound found in the root of *Curcuma longa* L. (Zingiberaceae), which has been widely used as a yellow pigment, a spice in the food industry, and a traditional medicine in Asia. Mounting scientific evidence indicates that CUR is a versatile bioactive compound possessing antioxidant,[33] anti-inflammatory,[34] antihyperlipidemic,[35] liver antifibrotic,[36] antiangiogenic,[37] antineoplastic, and chemoprotective properties.[38] The diverse bioactivities displayed by this single natural compound have made CUR a subject of intense and broad investigations for potential functional and medicinal foods as well as drug development for the prevention and treatment of various diseases such as colon cancer,[39] cystic fibrosis,[40] inflammatory bowel disease,[41] and HIV-infection.[42]

Although currently under investigation in human clinical trials, low bioavailability has hampered the desired therapeutic use of CUR.[43] Studies have shown that poor oral absorption

[1] Reprinted with permission from Zhang, F.; Koh, G. Y.; Jeansonne, D. P.; Hollingsworth, J.; Russo, P.S.; Vicente, G.; Stout, R. W.; Liu, Z. J. Pharm. Sci. 2011, 100, 2778-2789. Copyright ©

due to its low aqueous solubility and instability in the gastrointestinal tract may be responsible for the low bioavailability of CUR.[44,45] The development of a delivery system that can enable the administration of stable CUR in an aqueous gastrointestinal environment will significantly increase its potential for therapeutic use. Many approaches have been undertaken to improve the bioavailability of CUR. Existing pharmaceutical formulation techniques have been employed for CUR, including nanoparticle-based delivery systems,[46] liposomal delivery systems,[47] self-microemulsifying drug delivery systems,[48] gastroretentive floating drug delivery systems,[49] micelles, and phospholipid complexes.[50,51] Although each has made advancements, fundamental and practically significant improvement of oral bioavailability remains an elusive goal.

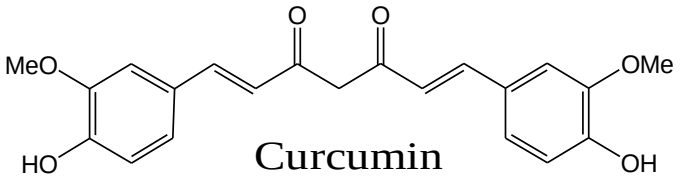

Curcumin

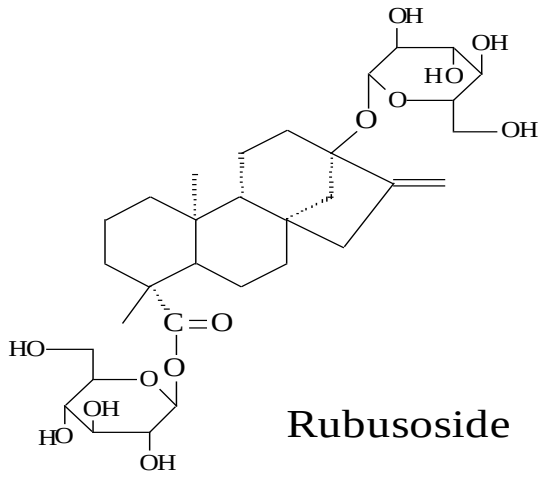

Rubusoside

Figure 2-14 Chemical structures of curcumin and rubusoside.

In a search to identify bioactive compounds from plant sources, it was discovered that some steviol glycosides such as stevioside, rebaudioside A, and rubusoside (RUB) possess solubilizing

properties. RUB (Figure 2-14), in particular, showed solubility enhancement for a wide spectrum of active natural and synthetic compounds. RUB is a commonly known natural sweetening agent and its major use is seen in food and beverage products. In this study, we developed a novel CUR formulation, in which RUB acted as a solubilizer. The RUB-solubilized CUR formulation was characterized for its solubility enhancement, loading efficiency, and resulting particle size; however, the scope of this discussion is strictly limited to the particle size determination.

2.3.2 Results and Discussion

Figure 2-15 Curcumin (CUR) water solutions in the presence of 0%, 1%, 2.5%, 5%, and 10%(w/v) rubusoside (RUB) (from left).

In the presence of 1% RUB (w/v), CUR was solubilized to 61 µg/mL. When the RUB concentration reached 10% w/v (the highest in this study), CUR was solubilized in water to 2318 µg/mL, the highest concentration achieved in this study. Visually, the RUB-solubilized CUR water solutions displayed an apparent difference in the intensity of yellow color, resulting primarily from the yellow CUR rather than from the colorless RUB (Figure 2-15). As the concentration of RUB increased and more CUR dissolved into the solution, the yellow color became more intense. Although this preliminary evidence suggested the effectiveness of the solubilizing agent, it was necessary to acquire quantitative details regarding the structural properties of the system. DLS was instrumental in providing this particular information.

Based on the linear behavior of the semilogarithmic plot shown in Figure 2-16, the particles are confirmed as monodispersed. The measured apparent D_h for the 10% CUR was 7.64 ± 0.4 nm. Although conclusive evidence about the size and dispersity of the solution was obtained from the semilogarithmic plot of the autocorrelation function, further distribution analyses (CONTIN) reaffirmed these findings (see Figure 2-17).

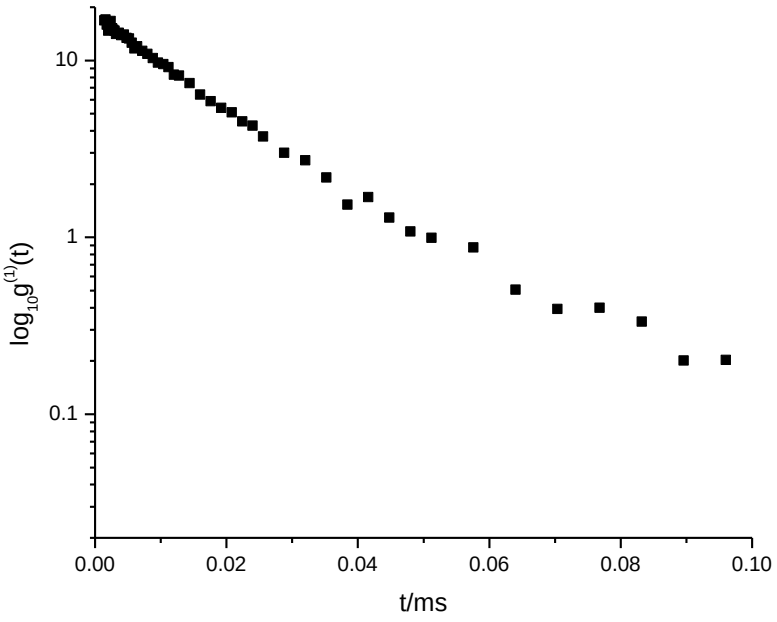

Figure 2-16 Semilogarithmic plot of normalized first-order autocorrelation function for 10% CUR solution.

The solubilization of hydrophobic curcumin by RUB was apparently driven by the formation of water-soluble nanoparticles between the two compounds, as observed and determined by TEM and DLS. RUB is an amphiphilic compound possessing both lipophilic steviol unit and hydrophilic glucose units. This property may point the formed nanoparticles to be nanomicelles because it is capable of forming micelles in water. The RUB molecule has the shape of a bolaform amphiphile—hydrophobic rings in the center with identical hydroxyl groups on each end. It is not unreasonable to suspect that the molecules can self-associate to minimize the

exposure of their central groups to water, as in other bolaform amphiphiles.[52] Because of this property, it is reasonable to suspect that CUR is encapsulated in the self-associated RUB micelles in water to avoid aqueous environments. The TEM (see Section 2.1.4) and DLS results provide only a suggestive spherical shape.

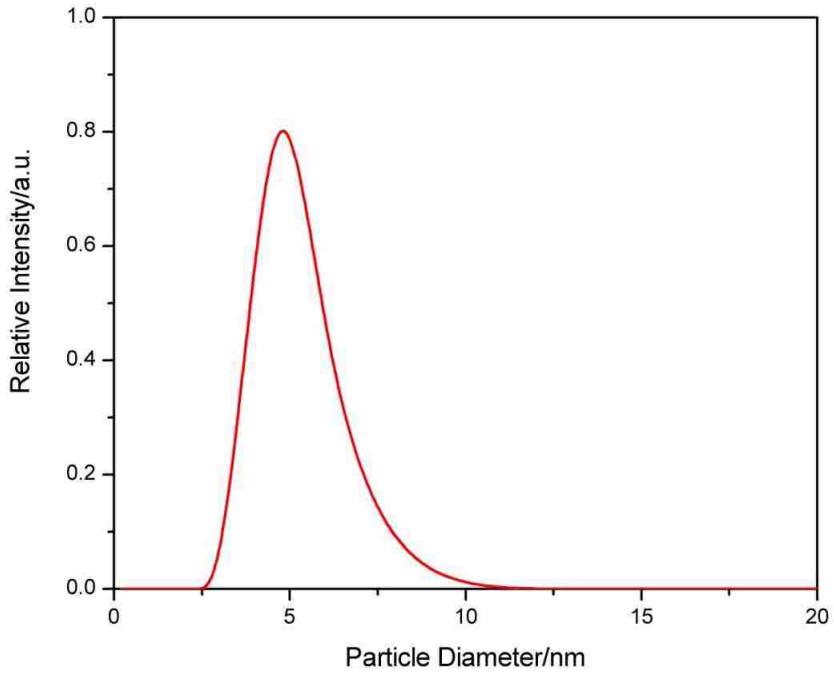

Figure 2-17 Particle size distribution of the 10% CUR solution. The narrow distribution confirms the monodispersity of the sample.

2.4 Characterization of Gel-like Systems: Sol-Gel Transition in the Assembly of Multivalent Signaling Proteins[2]

2.4.1 Background and Rationale

Covalent and non-covalent interactions between multivalent small molecules are central elements of classical polymer chemistry/physics and supramolecular chemistry[53-55]. These fields have produced theories and experimental demonstrations of sharp transitions between small

[2] Reprinted with permission from Li, P.; Banjade, S.; Cheng, H. C.; Kim, S.; Chen, B.; Guo, L.; Llaguno, M.; Hollingsworth, J. V.; King, D. S.; Banani, S. F.; Russo, P. S.; Jiang, Q. X.; Nixon, B. T.; Rosen, M. K.; *Nature* **2012**, 483, 336-340. Copyright © 2012, Nature Publishing Group.

assemblies and macroscopic polymer gels (known as sol-gel transitions) as the degree of bonding increases. The transition point (critical point) depends on physical properties of the monomeric species, including valency and affinity. The polymer can have a variety of physical forms, ranging from phase-separated liquid to crystalline solid. For non-covalent systems, phase separation can strongly influence the sol-gel transition by altering the degree of bonding[56-57]. In biology, interactions between multivalent entities are found in diverse processes, including extracellular carbohydrate-lectin binding, intracellular signaling, RNA metabolism and chromatin organization in the nucleus[58-61]. Biological multivalency has been studied most extensively in the context of extracellular ligands binding to cell surface receptors, where antibody-receptor[62] and carbohydrate-lectin[58] systems can assemble into crosslinked networks. These networks are typically precipitates[62-63], but liquid-like gels have also been described[64]. Multivalency has been much less studied in the context of intracellular molecules, which often share characteristics of high valency, modest affinity, and long, flexible connections between binding elements[65]. Here we asked whether these systems also undergo sharp transitions to polymers, and if so, what the macroscopic properties of the polymers are and how such transitions could be regulated and affect function.

The initial studies focus on the interactions between the SRC homology 3 (SH3) domain and its proline-rich motif (PRM) ligand, two widely observed modules that often appear in tandem arrays in signaling proteins[59,65]. Two classes of engineered proteins were generated: one composed of repeats of a single SH3 domain ($SH3_m$, where m = 1-5), and the other composed of repeats of a PRM ligand (PRM_n, where n = 1-5). When mixed, these proteins form into spherical liquid droplets (see Figure 2-18). Dynamic light scattering (DLS) was used to monitor the phase transitions of the multivalent proteins upon assembly.

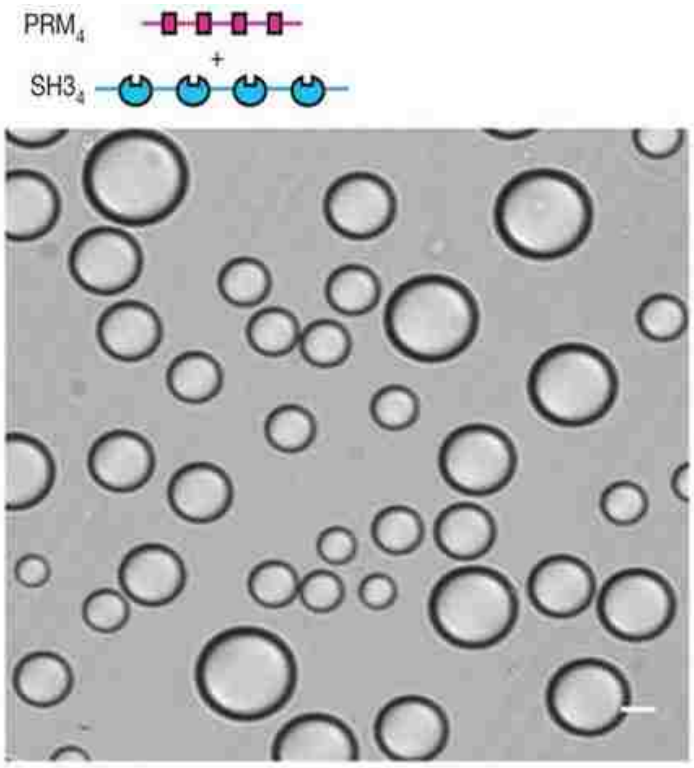

Figure 2-18 Liquid droplets observed by differential interference contrast microscopy when 300 μM $SH3_4$ and 300 μM PRM_4 were mixed. Scale bars, 20 μm. Adapted from reference 66.

2.4.2 Results and Discussion

DLS analyses of the droplet phases created by mixing $SH3_5$ and PRM_n showed multiphase intensity autocorrelation curves with a complex distribution of relaxation times (spanning 0.2-20 msec or longer) which were evaluated using CONTIN (see Figure 2-19). The decay rates and amplitudes from the CONTIN analyses were further investigated as a function of scattering angle (Figure 2-20). Some of these relaxation times nonlinearly scale with the square of scattering angle (q^2). The wide range of timescales, the presence of long-timescale processes and the q^2-independence of some of these processes are typical of polymer solutions in the semi-dilute range but are highly atypical of discrete molecular species[67]. These findings, as well as results from other techniques (SAXS, cryo-TEM, optical and fluorescence microscopy) in this study,

indicated that the observed phase separation was driven by the assembly of the multivalent proteins into large species.

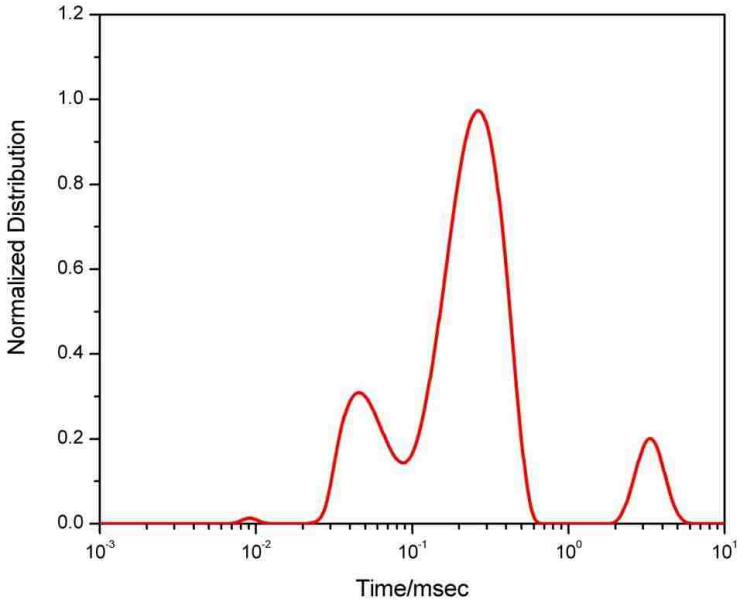

Figure 2-19 Decay time distribution of the autocorrelation function at 90˚ scattering angle for multimodal droplet phase.

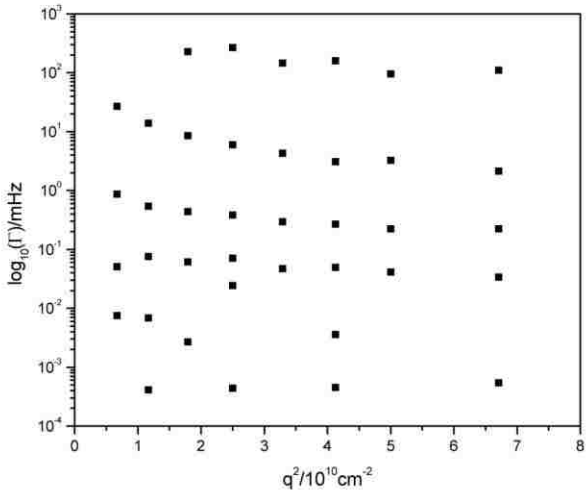

Figure 2-20 The Γ values given by CONTIN at each scattering angle for the complex droplet phase. Several modes are present, corresponding to the multiple decay modes.

2.5 Conclusions

Characterization techniques, including AUC, SAXS, DLS, FF-TEM and cryo-TEM permit the evaluation of solution-borne colloidal particles and self-assembled structures in their native solvated state. As a result, a vast number of potential drug delivery systems, (e.g., liposomes, lipid emulsions, micelles, etc.) can be developed or improved upon. Each technique provides different but complementary information about the physical properties of (macro-)molecules in solution.

In the presented reports, the versatile capabilities of DLS were demonstrated in the analysis of two distinct sample types, which included micellar aggregates and gel-like protein assemblies. The determined particle size and size-distribution of the RUB-solubilized CUR formulation confirmed solubility enhancement. The measured particle size was in agreement with the acquired TEM micrographs that suggest the particles are micelles. In the study concerning multivalent protein assembly, DLS was used to monitor the resulting phase transitions. The observed scattering behavior, determined via CONTIN analysis, was typical of polymer solutions in the semi-dilute range. These results indicated the phase separation was driven by the assembly of the multivalent proteins into large species.

In the next chapter, the previously discussed characterization techniques are employed to understand the self-assembly of porphyrins in aqueous solution. This preliminary exercise is an important segue into the development of porphyrins conjugated to colloidal particles for controlled assembly.

2.6 References

(1) Allen, T. M.; Cullis, P. R. Drug Delivery Systems: Entering the Mainstream. *Science* **2004**, *303*, 1818-1822.

(2) Svedberg, T.; Pedersen, K. O.; Bauer, J. H. *The ultracentrifuge*; The Clarendon Press: Oxford, 1940,

(3) Ralston, G. B. *Introduction to Analytical Ultracentrifugation*; Beckman Instruments, Inc: Palo Alto. Calif, 1993,

(4) Svedberg, T.; Rinde, H. The Ultra-centrifuge, A new instrument for the determination of size and distribution of size of particle in amicroscopic colloids. *J. Am. Chem. Soc.* **1924**, *46*, 2677-2693.

(5) Schachman, H. K. *Ultracentrifugation in biochemistry*; Academic Press: New York, 1959,

(6) Maechtle, W.; Börger, L. *Analytical Ultracentrifugation of Polymers and Nanoparticles*; Springer: New York, 2006,

(7) Stafford, W. F. Boundary analysis in sedimentation transport experiments: A procedure for obtaining sedimentation coefficient distributions using the time derivative of the concentration profile. *Anal. Biochem.* **1992**, *203*, 295-301.

(8) Ebel, C. Analytical ultracentrifugation: State of the art and perspectives. In *Protein Structures: Methods in Protein Structure and Stability Analysis*; Nova Science Publishers: New York, 2007, p 229-260.

(9) Byron, O.; Harding, S. E. New developments in analytical ultracentrifugation and related macromolecular modelling techniques. *Eur Biophys J* **1997**, *25*, 305-306.

(10) Furst, A. *Overview of Sedimentation Velocity for the Optima XL-A Analytical Ultracentrifugation, Technical Information DS-819*; Beckman Instruments, Inc.: Palo Alto, CA, 1991,

(11) Fujita, H. *Foundations of ultracentrifugal analysis*, *Chemical Analysis*; Wiley-Interscience: New York, 1975; Vol. 42,

(12) Hooyman, G. J. "Thermodynamics of irreversible processes in rotating systems," Thesis. *University of Leiden, Leiden,* **1955**.

(13) Van Holde, K. E.; Johnson, W. C.; Ho, P. S. *Principles Of Physical Biochemistry*; Pearson/Prentice Hall: Upper Saddle, N.J., 2006,

(14) Richard, A. J. Solution conformations and structural thermodynamics of Type I DNA polymerases from escherichia coli and thermus aquaticus.Dissertation, Louisiana State University, 2008.

(15) McRorie, D. K.; Voelker, P. J. *Self-associating Systems in the Analytical Ultracentrifuge*; Beckman Instruments: Palo Alto, CA, 1993,

(16) Chervenka, C. H. *A manual of methods for the analytical ultracentrifuge*; Spinco Division of Beckman Instruments: Palo Alto, CA, 1969,

(17) Lindner, P.; Zemb, T. *Neutron, X-Ray and Light Scattering : Introduction to an Investigative Tool for Colloidal and Polymeric Systems*; Elsevier Science Publishers B.V.: Bombannes, 1990,

(18) Stribeck, N. *X-Ray Scattering of Soft Matter*; Springer: Berlin Heidelberg, 2007,

(19) Shrestha, L. K.; Glatter, O.; Aramaki, K. Structure of nonionic surfactant (glycerol alpha-monomyristate) micelles in organic solvents: a SAXS study. *J. Phys. Chem. B* **2009**, *113*, 6290-6298.

(20) Provencher, S. W. A constrained regularization method for inverting data represented by linear algebraic or integral equations. *Comput. Phys. Commun.* **1982**, *27*, 213-227.

(21) Friedrich, H.; Frederik, P. M.; de With, G.; Sommerdijk, N. A. J. M. Imaging of Self-Assembled Structures: Interpretation of TEM and Cryo-TEM Images. *Angew. Chem. Int. Ed.* **2010**, *49*, 7850-7858.

(22) Zhang, F.; Koh, G. Y.; Jeansonne, D. P.; Hollingsworth, J.; Russo, P. S.; Vicente, G.; Stout, R. W.; Liu, Z. A novel solubility-enhanced curcumin formulation showing stability and maintenance of anticancer activity. *J. Pharm. Sci.* **2011**, *100*, 2778-2789.

(23) Hall, C. E. A Low Temperature Replica Method for Electron Microscopy. *J. Appl. Phys.* **1950**, *21*, 61-62.

(24) Meryman, H. T. Replication of frozen liquids by vacuum evaporation *J. Appl. Phys.* **1950**, *21*.

(25) Meryman, H. T.; Kafig, E. *The Study of Frozen Specimens, Ice Crystals and Ice Crystal Growth by Electron Microscopy*; Naval Medical Research Institute: Bethesda, MD, 1955, 529-544.

(26) Moor, H.; Mühlethaler, K. Fine structure in frozen-etched yeast cells. *J. Cell Biol.* **1963**, *17*, 609-628.

(27) Meyer, H. W.; Richter, W. Freeze-fracture studies on lipids and membranes. *Micron* **2001**, *32*, 615-644.

(28) Moor, H.; Muhlethaler, K.; Waldner, H.; Frey-Wyssling, A. A new freezing-ultramicrotome. *J. Biophys. Biochem. Cytol.* **1961**, *10*, 1-13.

(29) Dorman, D. A study of the interactions of lipid bilayers and dendrimers using small angle X-ray scattering and freeze fracture transmission electron microscopy.Dissertation, Louisiana State University, 2010.

(30) Kuntsche, J.; Horst, J. C.; Bunjes, H. Cryogenic transmission electron microscopy (cryo-TEM) for studying the morphology of colloidal drug delivery systems. *Int. J. Pharm.* **2011**, *417*, 120-137.

(31) Vinson, P. K.; Bellare, J. R.; Davis, H. T.; Miller, W. G.; Scriven, L. E. Direct imaging of surfactant micelles, vesicles, discs, and ripple phase structures by cryo-transmission electron microscopy. *J. Colloid Interface Sci.* **1991**, *142*, 74-91.

(32) Abraham, S. A.; Edwards, K.; Karlsson, G.; Hudon, N.; Mayer, L. D.; Bally, M. B. An evaluation of transmembrane ion gradient-mediated encapsulation of topotecan within liposomes. *J. Control. Rel.* **2004**, *96*, 449-461.

(33) Shukla, P. K.; Khanna, V. K.; Khan, M. Y.; Srimal, R. C. Protective effect of curcumin against lead neurotoxicity in rat. *Hum Exp Toxicol* **2003**, *22*, 653-658.

(34) Abe, Y.; Hashimoto, S.; Horie, T. Curcumin inhibition of inflammatory cytokine production by human peripheral blood monocytes and alveolar macrophages. *Pharmacol Res* **1999**, *39*, 41-47.

(35) Pari, L.; Murugan, P. Antihyperlipidemic effect of curcumin and tetrahydrocurcumin in experimental type 2 diabetic rats. *Ren Fail* **2007**, *29*, 881-889.

(36) Kang, Q.; Chen, A. Curcumin suppresses expression of low-density lipoprotein (LDL) receptor, leading to the inhibition of LDL-induced activation of hepatic stellate cells. *Br J Pharmacol* **2009**, *157*, 1354-1367.

(37) Liu, D.; Schwimer, J.; Liu, Z.; Woltering, E. A.; Greenway, F. L. Antiangiogenic effect of curcumin in pure versus in extract forms *Pharmaceut Biol* **2008**, *46*, 677-682.

(38) Duvoix, A.; Blasius, R.; Delhalle, S.; Schnekenburger, M.; Morceau, F.; Henry, E.; Dicato, M.; Diederich, M. Chemopreventive and therapeutic effects of curcumin. *Cancer Lett* **2005**, *223*, 181-190.

(39) Johnson, J. J.; Mukhtar, H. Curcumin for chemoprevention of colon cancer. *Cancer Lett* **2007**, *255*, 170-181.

(40) Egan, M. E.; Pearson, M.; Weiner, S. A.; Rajendran, V.; Rubin, D.; Glockner-Pagel, J.; Canny, S.; Du, K.; Lukacs, G. L.; Caplan, M. J. Curcumin, a major constituent of turmeric, corrects cystic fibrosis defects. *Science* **2004**, *304*, 600-602.

(41) Hanai, H.; Sugimoto, K. Curcumin has bright prospects for the treatment of inflammatory bowel disease. *Curr Pharm Des* **2009**, *15*, 2087-2094.

(42) Jordan, W. C.; Drew, C. R. Curcumin--a natural herb with anti-HIV activity. *J Natl Med Assoc* **1996**, *88*, 333.

(43) Hatcher, H.; Planalp, R.; Cho, J.; Torti, F. M.; Torti, S. V. Curcumin: from ancient medicine to current clinical trials. *Cell Mol Life Sci* **2008**, *65*, 1631-1652.

(44) Anand, P.; Kunnumakkara, A. B.; Newman, R. A.; Aggarwal, B. B. Bioavailability of curcumin: problems and promises. *Mol Pharm* **2007**, *4*, 807-818.

(45) Kidd, P. M. Bioavailability and activity of phytosome complexes from botanical polyphenols: the silymarin, curcumin, green tea, and grape seed extracts. *Altern Med Rev* **2009**, *14*, 226-246.

(46) Bisht, S.; Feldmann, G.; Soni, S.; Ravi, R.; Karikar, C.; Maitra, A. Polymeric nanoparticle-encapsulated curcumin ("nanocurcumin"): a novel strategy for human cancer therapy. *J Nanobiotechnology* **2007**, *5*, 3.

(47) Li, L.; Braiteh, F. S.; Kurzrock, R. Liposome-encapsulated curcumin: in vitro and in vivo effects on proliferation, apoptosis, signaling, and angiogenesis. *Cancer* **2005**, *104*, 1322-1331.

(48) Cui, J.; Yu, B.; Zhao, Y.; Zhu, W.; Li, H.; Lou, H.; Zhai, G. Enhancement of oral absorption of curcumin by self-microemulsifying drug delivery systems. *Int J Pharm* **2009**, *371*, 148-155.

(49) Shishu; Gupta, N.; Aggarwal, N. Bioavailability enhancement and targeting of stomach tumors using gastro-retentive floating drug delivery system of curcumin--"a technical note". *AAPS PharmSciTech* **2008**, *9*, 810-813.

(50) Liu, A.; Lou, H.; Zhao, L.; Fan, P. Validated LC/MS/MS assay for curcumin and tetrahydrocurcumin in rat plasma and application to pharmacokinetic study of phospholipid complex of curcumin. *J. Pharm. Biomed. Anal.* **2006**, *40*, 720-727.

(51) Ma, Z.; Shayeganpour, A.; Brocks, D. R.; Lavasanifar, A.; Samuel, J. High-performance liquid chromatography analysis of curcumin in rat plasma: application to pharmacokinetics of polymeric micellar formulation of curcumin. *Biomed. Chromatogr.* **2007**, *21*, 546-552.

(52) Claussen, R. C.; Rabatic, B. M.; Stupp, S. I. Aqueous self-assembly of unsymmetric Peptide bolaamphiphiles into nanofibers with hydrophilic cores and surfaces. *J Am Chem Soc* **2003**, *125*, 12680-12681.

(53) Flory, P. J. *Principles of Polymer Chemistry*; Cornell University Press: Ithaca, 1953,

(54) Cohen, R. J.; Benedek, G. B. Equilibrium and Kinetic Theory of Polymerization and the Sol-Gel Transition. *J. Phys. Chem.* **1982**, *86*, 3696-3714.

(55) Lehn, J.-M. Supramolecular Polymer Chemistry--Scope and Perspectives. *Polym. Int.* **2002**, *51*, 825-839.

(56) Tanaka, F. *Polymer Physics: Applications to Molecular Association and Thermoreversible Gelation*; Cambridge University Press: Cambridge, UK, 2011,

(57) Semenov, A. N.; Rubinstein, M. Thermoreversible gelation in solutions of associative polymers. 1. Statics. *Macromolecules* **1998**, *31*, 1373-1385.

(58) Brewer, C. F.; Miceli, M. C.; Baum, L. G. Clusters, bundles, arrays and lattices: novel mechanisms for lectin-saccharide-mediated cellular interactions. *Curr Opin Struct Biol* **2002**, *12*, 616-623.

(59) Pawson, T.; Nash, P. Assembly of cell regulatory systems through protein interaction domains. *Science* **2003**, *300*, 445-452.

(60) Lunde, B. M.; Moore, C.; Varani, G. RNA-binding proteins: modular design for efficient function. *Nat Rev Mol Cell Biol* **2007**, *8*, 479-490.

(61) Ruthenburg, A. J.; Li, H.; Patel, D. J.; Allis, C. D. Multivalent engagement of chromatin modifications by linked binding modules. *Nat Rev Mol Cell Biol* **2007**, *8*, 983-994.

(62) Goldberg, R. A theory of antibody-antigen reactions. I. Theory for reactions of multivalent antigen with bivalent and univalent antibody. *J Am Chem Soc* **1952**, *74*, 5715-5725.

(63) Dam, T. K.; Oscarson, S.; Roy, R.; Das, S. K.; Page, D.; Macaluso, F.; Brewer, C. F. Thermodynamic, kinetic, and electron microscopy studies of concanavalin A and Dioclea grandiflora lectin cross-linked with synthetic divalent carbohydrates. *J Biol Chem* **2005**, *280*, 8640-8646.

(64) Sisu, C.; Baron, A. J.; Branderhorst, H. M.; Connell, S. D.; Weijers, C. A.; de Vries, R.; Hayes, E. D.; Pukin, A. V.; Gilbert, M.; Pieters, R. J.; Zuilhof, H.; Visser, G. M.; Turnbull, W. B. The influence of ligand valency on aggregation mechanisms for inhibiting bacterial toxins. *Chembiochem* **2009**, *10*, 329-337.

(65) Jin, J.; Xie, X.; Chen, C.; Park, J. G.; Stark, C.; James, D. A.; Olhovsky, M.; Linding, R.; Mao, Y.; Pawson, T. Eukaryotic protein domains as functional units of cellular evolution. *Sci. Signal.* **2009**, *2*, 76.

(66) Li, P.; Banjade, S.; Cheng, H. C.; Kim, S.; Chen, B.; Guo, L.; Llaguno, M.; Hollingsworth, J. V.; King, D. S.; Banani, S. F.; Russo, P. S.; Jiang, Q. X.; Nixon, B. T.; Rosen, M. K. Phase transitions in the assembly of multivalent signalling proteins. *Nature* **2012**, *483*, 336-340.

(67) Li, J.; Ngai, T.; Wu, C. The Slow Relaxation Mode: From Solutions to Gel Networks. *Polym. J.* **2010**, *42*, 609-625.

CHAPTER 3 CHARACTERIZATION OF THE SELF-ASSEMBLY OF MESO-TETRA(4-SULFONATOPHENYL)PORPHYRIN (H_2TPPS^{4-}) IN AQUEOUS SOLUTIONS[3]

3.1 Introduction

Self-assembly is a prominent, naturally occurring phenomenon which involves the automatic formation of dimers and higher oligomers of various and often complex structures. Interest in understanding assembly processes has grown enormously over the past decade as a result of the important potential applications in various nanomaterials, such as molecular switches, fluorescent sensors, photonic wires and catalysts.[1-3] Furthermore, self-assembly is exhibited in multiple ways within living cells; thus, knowledge of the driving mechanism or mechanisms and properties may provide insight into the nature of life.[4] Characterizing aggregates and their self-associative behavior serves as the basis for resolving many of the intricacies of the assembly process.

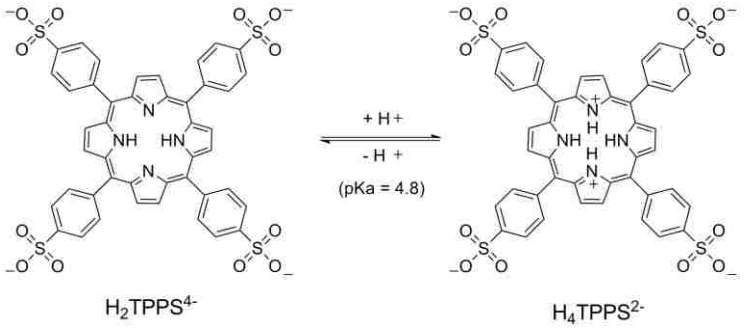

Scheme 3-1 Molecular structure of *meso*-tetra(4-sulfonatophenyl)porphyrin (H_2TPPS^{4-}) and its di-anionic species, H_4TPPS^{2-}, upon protonation of the nitrogen atoms ($pK_a \approx 4.8$) at the macrocycle core.

Several water-soluble porphyrins have been considered model systems for indigenous porphyrin derivatives in the physiological state.[5] Such macrocycles can self-assemble spontaneously into

[3] Reprinted with permission from Hollingsworth, J.V.; Richard, A.J.; Vicente, M.G.H.; Russo, P.S. *Biomacromolecules* **2012**, 13(1) 60-72. Copyright © 2012, American Chemical Society.

aggregates through non-covalent interactions (e.g. hydrogen-bonding, hydrophobic and electrostatic), depending on their electronic and steric properties. As a result, and also due to their rich photochemical, spectroscopic and electrochemical properties, the self-assembly of porphyrinoids, mainly porphyrins, chlorins and phthalocyanines, has been widely investigated.[6-13] *Meso*-tetra(4-sulfonatophenyl)porphyrin (H_2TPPS^{4-}) is among the most commonly studied porphyrins due to its water solubility and commercial availability. H_2TPPS^{4-} is a tetra-anionic porphyrin that forms the di-anionic species, H_4TPPS^{2-}, upon protonation of the nitrogen atoms ($pK_a \approx 4.8$) within the macrocycle core (Scheme 3-1). The formation of highly ordered aggregates of H_4TPPS^{2-} at low pH values has been previously observed,[11-12] and may be thought of as the result of the intermolecular electrostatic attractions between the positively charged core and the negatively charged periphery. Specific types of aggregates may form as a result of this ionic self-assembly, the main two being H- and J-type (Figure 3-1). H-aggregates, so named because of their spectral band blueshift (hypsochromic) with respect to the absorption band of the monomer, correspond to the face-to-face stacking of the monomeric species. In contrast, J-aggregates (named after their discoverer, Scheibe Jelly) are edge-by-edge or side-to-side assemblies that produce bathochromic (red) shifts.[13] Metal-free porphyrins, such as H_2TPPS^{4-}, are known to form aggregates in aqueous solutions, but despite several studies,[14-19] the characterization type, number of monomers involved, aggregate size and morphology remain controversial and are not fully understood across a variety of external conditions and solution preparation protocols. Porphyrin self-assembly remains an active area of research because the structure and photophysical properties of aggregates ultimately determine their usefulness and applications, for example as organic semiconductors for nanometer-scale photovoltaic cells, artificial light-harvesting systems, nonlinear optic materials and in photodynamic therapy

(PDT).[5,20-22] The development of quantitative analytical and imaging techniques has facilitated the characterization of aggregation phenomena; in turn, this should make it easier to understand and eventually manipulate porphyrin assembly. A variety of factors are known to influence porphyrin aggregation in aqueous solutions, including concentration, temperature, pH, ionic strength, metal ions and their counter anions. In addition, porphyrin aggregation has been studied in the presence of polypeptides,[23] proteins,[24] nucleic acids,[25] surfactants,[26] PAMAM dendrimers,[27] cyclodextrins,[28] carbon[29] and noncarbon[30] nanotubes, ionic liquids[31], and other media, as well as in organic solvents.[32] The characterization of the resulting materials using a variety of complementary analytical techniques is beneficial to this area of research; for example, in the optimization of the topical delivery of H_2TPPS^{4-} for enhanced skin penetration and PDT, which has been investigated as a function of pH and ionic strength.[33]

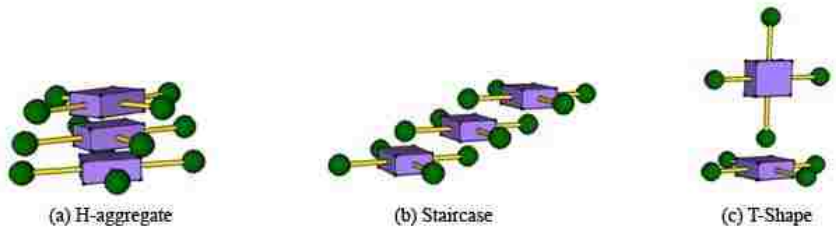

Figure 3-1 Structural models for (a) H- and (b, c) J-type aggregates.

In the present study, we investigated the self-associative behavior and morphology of H_2TPPS^{4-} aggregates in aqueous solutions at μM concentrations as functions of solution preparation protocol, pH, time, and ionic strength. The net result of previous studies is that H_4TPPS^{2-} forms tube-like structures, although not much is known about the mechanism of this occurrence. Two open questions are: when does the process begin and what specific conditions are necessary? In the present work, analytical ultracentrifugation (AUC) provides, for the first time, information about the self-assembly at μM concentration. In order to connect these results

to previous studies, a series of complementary experiments and analytical methods were used, including UV-Vis and fluorescence spectroscopy measurements, small angle X-ray scattering (SAXS), cryogenic transmission electron microscopy (cryo-TEM) and freeze-fracture transmission electron microscopy (FF-TEM). Whereas UV-Vis and fluorescence techniques enabled us to determine the type of aggregates formed—either J or H—AUC and SAXS provided complementary details and information about the size of the assemblies in solution. Cryo-TEM and FF-TEM provided direct visualization of the aggregates. Furthermore, we modeled the main aggregate species formed at low pH using DAMMIF,[34] a computational program that performs *ab initio* shape determination using SAXS data. Porphyrin aggregation has not been previously studied using all the above techniques in a single investigation. In particular, AUC is a staple method of physical biochemistry commonly used to study protein complexes[35] but which has also been applied in the investigation of synthetic systems.[36-38] A wide range of information about the thermodynamic and hydrodynamic properties of solutes in the native state can be attained via AUC, along with absolute measurements of their molecular weights. The aim of the present study was to characterize the morphology and self-associative properties of H_2TPPS^{4-} aggregates in aqueous solutions, in such a way as to permit a comparison with previously published reports, while providing new insight and findings.

3.2 Experimental

3.2.1 Materials and General Considerations

Meso-tetra(4-sulfonatophenyl) porphyrin (H_2TPPS^{4-}) was obtained as the tetra sodium salt from Frontier Scientific. All other solvents and reagents were obtained from Sigma-Aldrich and used without further purification. The pH of the buffer solutions was measured with a Fisher Scientific AR10 pH meter. The stock phosphate buffer solution (PB) was prepared by mixing

Na_2HPO_4 in deionized water to yield 0.1 M solution, followed by drop-wise addition of H_3PO_4 while monitoring with a pH meter to obtain targeted levels.

3.2.2 Sample Preparation

Because solution preparation protocol is important in studies of self-assembling systems, four distinct methods of sample preparation were used to optimize the various measurements. Many of the applied analytical techniques require low concentrations, and the very dilute (micromolar) concentration regime has special importance in this study. Methods 1, 2 and 3 are designed to prepare dilute solutions. Method 1 refers to the direct addition of porphyrin to the buffer. Micromolar solutions of H_2TPPS^{4-} were prepared directly by dissolving the appropriate amount of solid in PB (0.1 M) at the desired low concentration. Direct addition was also used for the ionic strength-dependent studies, which used relatively low-NaCl concentrations (0 mM – 200 mM). Method 2 refers to the preparation of solutions at a relatively high porphyrin concentration (2 mM) followed, after a period of 24 h, by dilution to the μM range. The 24-h incubation time induces further aggregation compared to Method 1, aiding in the investigation of concentration-dependent species. Method 3 was necessary for the high-ionic strength (1 M–10 M NaCl) studies and refers to the pre-dissolution of porphyrin (3 mM) in DMSO, followed by dilution (2 mM) in NaCl (35 mM–10 M)/PB (0.1 M) at pH 4. DMSO was used to ensure complete solubilization at high-NaCl concentrations; this is important to combat precipitation. The mixture was allowed 24 h to aggregate and was then further diluted to 2.5 μM concentration using stock NaCl/PB solution. Lastly, preparation method 4 refers to the direct addition of porphyrin at high (mM) concentration and was only used for the small angle X-ray scattering studies. Unless otherwise stated, method 1 was used.

3.2.3 UV-Vis and Fluorescence

UV-Vis spectra were collected by means of a Pharmacia Biotech Ultrospec 4000 spectrophotometer in the range of 350-700 nm at room temperature with a 1.0 cm × 1.0 cm quartz cuvette. 0.1 M PB was used to prepare the porphyrin solutions and the pH values were achieved by adding ortho-phosphoric acid 85% and measuring the pH with a Fisher Scientific AR10 pH meter. Fluorescence spectra were acquired with a Horiba Fluorolog Spectrofluorometer at room temperature in the emission range of 400-850 nm using an excitation wavelength matching the absorption maxima of 420 nm (preparation method 1) or 490 nm (preparation methods 2 and 3).

3.2.4 Analytical Ultracentrifugation (AUC)

Sedimentation equilibrium experiments were conducted using a Beckman Optima XL-A analytical ultracentrifuge. Epon charcoal-filled double-sector cells were assembled then loaded with 125 μl of solvent (0.1 M PB) in reference sector and 110 μl of 3.0 μM porphyrin in PB solution at pH 4 and 9 in the sample sector. The cell assembly was inserted into a four-hole rotor and the temperature inside the chamber was allowed to equilibrate at 20 °C while under vacuum. The most strongly absorbed wavelength from the preliminary wavelength scan of the samples was 424 nm. Sedimentation equilibrium was attained at 45,000 rpm over a time span of 24 h. The partial specific volume was acquired using the *ab initio* calculation method of Durchschlag and Zipper.[39] All data were analyzed using the Origin Equilibrium software program provided by Beckman.

3.2.5 Small Angle X-ray Scattering (SAXS)

SAXS experiments were performed on synchrotron beamline 6a at the Louisiana State University Center for Advanced Microstructures and Devices (CAMD), Baton Rouge, Louisiana.

Radiation generated at 8.00 keV (1.550 Å) illuminated porphyrin samples held at room temperature. Diffraction from silver behenate was used to establish the sample-to-detector distance. Samples (5-20 mM H_2TPPS^{4-} in 0.1 M PB at pH 4 and 9—i.e., 5% to 20% by weight) were injected and sealed in 1.0 mm capillaries (purchased from Charles Supper Co., special glass 10-SG). Azimuthally averaged data from the two-dimensional multiwire proportional counter (Molecular Metronics) were normalized for average transmitted intensity and corrected for buffer background using the SAXSGUI program (available from Rigaku) and analyzed using Irena 2 package[40] (Jan Ilavsky, Advanced Photon Source, Argonne National Laboratory) written for the IGOR Pro software program (WaveMetrics, Inc.). The proposed aggregate models were constructed based on the SAXS curves of the porphyrin at pH 4, which were fitted using Irena 2 to determine the pair distance distribution function, $P(r)$. The $P(r)$ data can also be obtained using the data manipulation program, Primus,[41] which is available in the ATSAS software package (http://www.embl-hamburg.de/biosaxs/software.html). The GNOM output of these data was used in the DAMMIF program (Franke and Svergun, European Molecular Biology Laboratory) to perform an *ab initio* shape determination. Default settings and parameters were applied for all computed models, and 12 independent reconstructions were averaged using the DAMAVER program[42] (Svergun and Petoukhov, European Molecular Biology Laboratory, and Institute of Crystallography) to achieve the most persistent shape features of the bead models. The many parameters for operation of these programs are described further in the Results and Discussion section, because information derived from simpler fitting procedures is used.

3.2.6 Freeze-Fracture Transmission Electron Microscopy (FF-TEM)

Freeze-fracture samples were prepared by first depositing a drop of sample (1 mM H_2TPPS^{4-} at pH 4, 48 hrs after solution preparation) onto a copper planchette (purchased from BAL-TEC).

The sample was frozen by rapid immersion into a liquid Freon (SHUR/Freeze^{TM} Cryogen Spray, purchased from Triangle Biomedical Sciences) bath, then stored in liquid nitrogen. The vitrified sample was transferred to the sample stage, which was submerged in liquid nitrogen. After transferring the sample stage into the freeze-etching chamber of the Balzers BAF-400 apparatus, the samples were fractured at a temperature of -110 °C. Once the fractured sample was allowed to etch for ~1 min., Pt–C was deposited at a 45° angle with respect to the sample surface followed by deposition of C at a 90° angle for reinforcement. The resulting replicas were washed in water repeatedly to remove the actual sample. The replicas were collected on 300 mesh Formvar-coated grids (purchased from Electron Microscopy Sciences) and allowed to dry overnight. TEM observations were performed with a JEOL JEM-100CX transmission electron microscope operated at 80 kV.

3.2.7 Cryogenic Transmission Electron Microscopy (Cryo-TEM)

This work was performed at Tulane University. A drop (2-5 μL) of 1 mM H_4TPPS^{2-} in 0.1 M PB at pH 4 was deposited onto a holey carbon grid. The droplet of sample was blotted to make a thin film (<200 nm) across the grid holes and then vitrified by quickly plunging the grid in liquid ethane (~ -170 ºC). Liquid ethane was prepared by supplying a flow of ethane gas into a liquid nitrogen bath. Once in an amorphous state, the sample was then transferred to a cold stage (Oxford Instruments CT3500J) to preserve the microstructures. Using phase contrast microscopy, the prepared samples were observed on a JEOL 1200EX transmission electron microscope.

3.3 Results and Discussion

3.3.1 UV-Vis and Fluorescence

Porphyrins have characteristic UV-Vis and fluorescence spectra; changes in the absorption and emission bands indicate changes in the porphyrin chromophore and/or its environment. UV-Vis and fluorescence spectroscopic measurements were used to determine the type of porphyrin aggregates formed in aqueous solutions, as a function of time (up to 1 month), pH (4-9) and ionic strength (0-10 M NaCl). We investigated changes in the absorption and emission bands of H_2TPPS^{4-} solutions at μM concentrations, within the pH range 4 to 9, which includes the reported pK_a for H_2TPPS^{4-} (4.8) and biologically relevant pH values. The results are shown in Figure 3-2. Only two distinct Soret bands were observed in the absorption spectra, at 418 nm (neutral and basic solutions) and 440 nm (pH 4 solution) within 30 min after solution preparation. At pH 5, both these absorptions were present, indicating the presence of at least two distinct species (Figure 3-2d). A shoulder at ~412 nm was also detected; this band corresponds to the absorption of the monomeric free-base species, as previously reported.[43] H-aggregates exhibit a spectral band blueshift (hypsochromic) with respect to the absorption band of the monomer, corresponding to the face-to-face stacking of the monomeric species. It is postulated that the shoulder at 406 nm is due to H-dimers of the free-base species, H_2TPPS^{4-}, while the band at 424 nm corresponds to H-dimers of the diacid species, H_4TPPS.[2-44] In contrast, J-aggregates are edge-by-edge or side-to-side assemblies that produce bathochromic (red) shifts. The bathochromic shifts observed for the Soret bands, along with the observed decrease of their extinction coefficients with time (Figure 3-2e), suggest the formation of J-type aggregates that were present 30 min after solution preparation (Figure 3-2d). In solutions at pH < 4.8 (i.e. at pH 4), the porphyrin exists in its diacid form, H_4TPPS^{2-}, due to protonation of the core nitrogens (see

Scheme 3-1). This is known[44] to cause a red shift of the Soret band and deep changes in the etio-type Q bands of the porphyrin monomer due to the change in symmetry, to long wavelengths and relatively broad bands at > 530 nm.

The results indicate that unprotonated porphyrin H_2TPPS^{4-} aggregates in aqueous solutions; i.e. the molecules overcome electrostatic repulsion, presumably via attractive hydrogen bonding and hydrophobic interactions. On the other hand, the zwitterionic nature of the diacid H_4TPPS^{2-} species (positively-charged core and negative charge at the macrocycle periphery) potentially forms larger and more stable J-aggregates via strong electrostatic interactions, in addition to hydrogen bonding and hydrophobic forces. Aggregation typically causes quenching of the porphyrin fluorescence, as well as a decrease of the Soret extinction coefficient, as observed in Figure 3-2b,e. The emission intensity for all porphyrin solutions at each pH value investigated decreased as time increased, indicating self-quenching effects due to aggregate formation.

The specific sample preparation protocol also defines the observed self-assembly phenomena and variations in spectral features. In the previously mentioned spectra (Figure 3-2a,b,d,e) the samples were made as low-concentration (μm) solutions directly (preparation Method 1). For the data shown in Figure 3-2c,f and 3-3b,d, stock porphyrin solutions at their respective pH level were prepared at a higher concentration (2 mM), incubated for 24 h and diluted to μM concentrations (preparation Method 2). The reasoning for this procedure was to further induce self-assembly, which is evident in the UV-Vis spectra via the emergence of an absorption band at 490 nm for pH 4 solutions. Previous studies[45] which report observing this band attribute it to J-aggregation of H_4TPPS^{2-}. Further details about this species are discussed later.

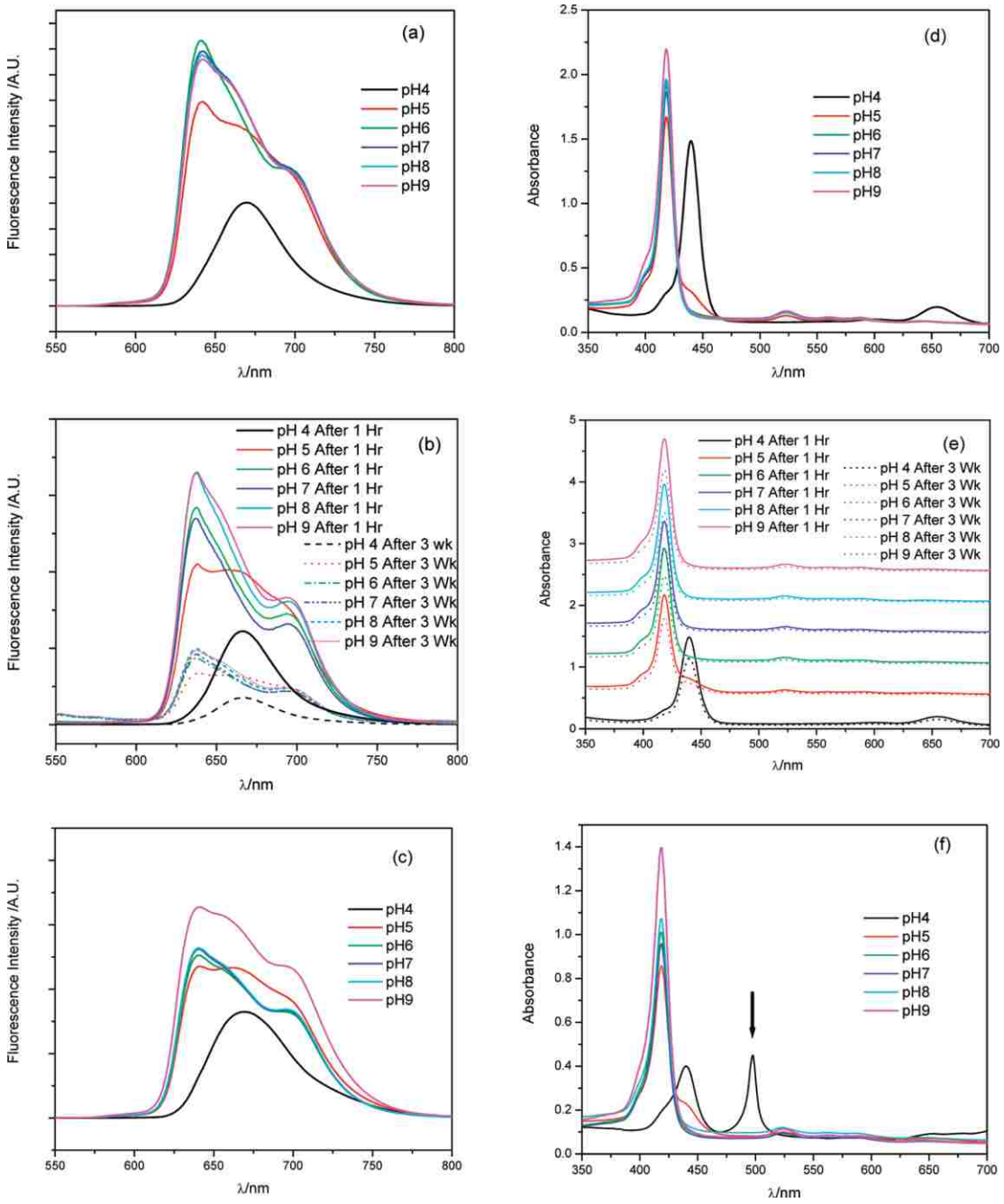

Figure 3-2 Fluorescence (left) and absorption (right) spectra of (a,d) 3.0 µM H_2TPPS^{4-} in 0.1 M PB at pH 4 (–),5 (–), 6 (–), 7 (–),8 (–), and 9 (–) acquired within 30 minutes after preparation, (b,e) 7.2 µM H_2TPPS^{4-} in 0.1 M PB at pH 4 (–),5 (–), 6 (–), 7 (–),8 (–), and 9 (–) acquired 1 hr (solid lines) and 3 week (dashed lines), respectively, after preparation (Note: in panel e, the absorption data are offset along the *y*-axis for clarity); and (c,f) 2.5 µM H_2TPPS^{4-} in 0.1 M PB at pH 4 (–),5 (–), 6 (–), 7 (–),8 (–), and 9 (–) acquired within 10 minutes after preparation. The arrow notes the new absorption band at 490 nm, resulting from preparation method 2.

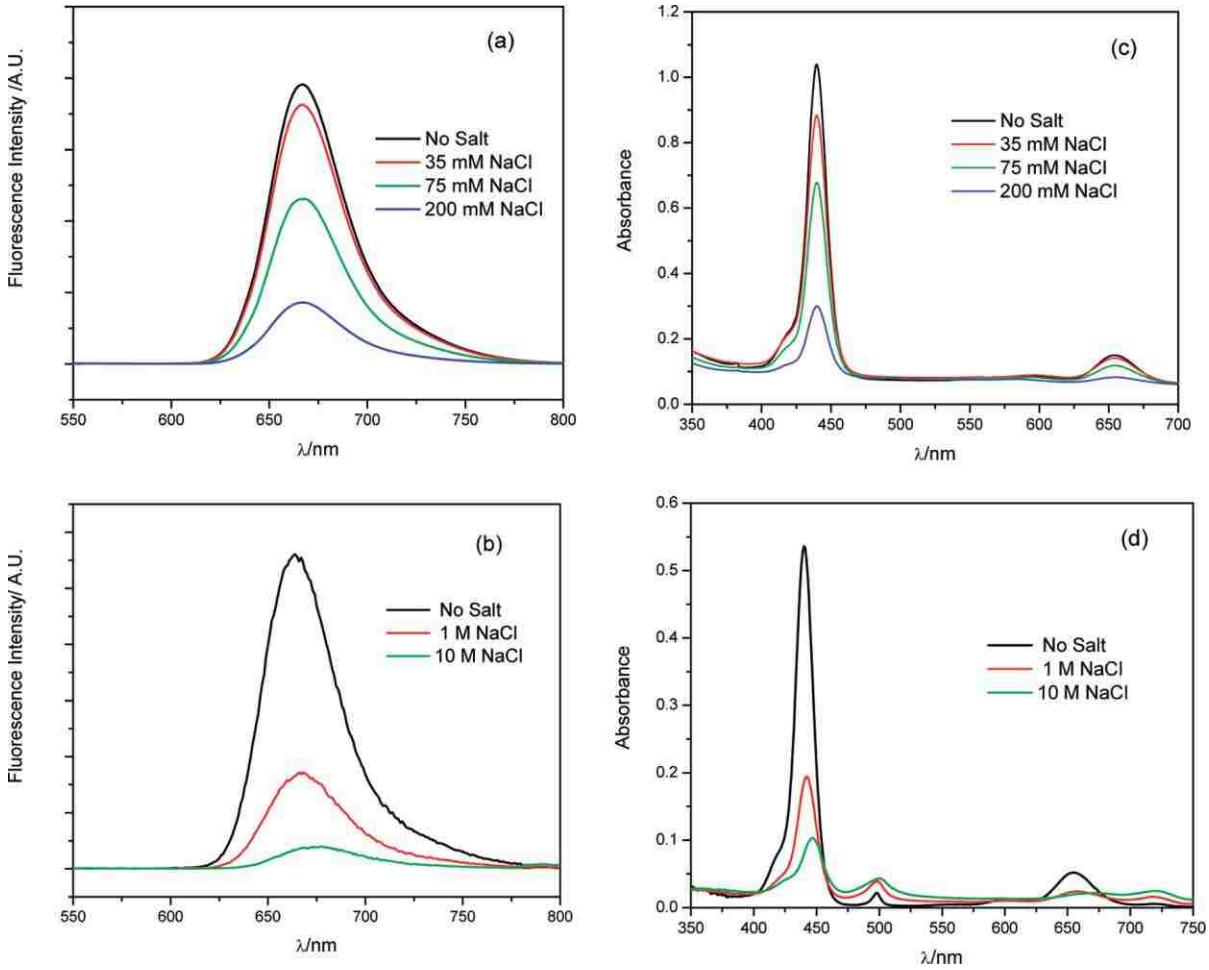

Figure 3-3 Fluorescence (left) and absorption (right) spectra of (a,c) 3.2 µM H_4TPPS^{2-} in 0.1 M PB at pH 4 with 0 mM (–),35 mM (–),75 mM (–), and 200 mM (–) NaCl using preparation Method 1; (b,d) 2.5 µM H_4TPPS^{2-} in 0.1 M PB at pH 4 with 0 M (–), 1 M (–), and 10 M (–) NaCl using preparation Method 3.

Using similar sample preparation variations, ionic strength studies were performed to note the effect on the aggregation process at pH 4. The intensity of the fluorescence emission and Soret band decreased significantly upon addition of NaCl, and this effect was more pronounced with increasing concentration of NaCl (Figure 3-3); for high-ionic strength (1 M to 10 M NaCl), H_2TPPS^{4-} was pre-dissolved in DMSO to ensure complete solubilization (preparation Method 3). These results suggest that addition of NaCl induces further self-assembly with formation of micron-sized aggregates, eventually leading to precipitation, which was clearly visible in the

porphyrin solutions prepared in 10 M NaCl/PB at pH 4. Previous studies suggest that the addition of NaCl induces aggregation [46-49] and our results support the notion.

3.3.2 Small Angle X-ray Scattering (SAXS)

Earlier workers have suggested an extended cylindrical structure for the aggregates.[45,50-52] The use of scattering methods to characterize large fibrillar structures is fraught with challenges. One might begin with dynamic and static light scattering (DLS/SLS), owing to the precision of these methods. Such experiments were indeed attempted, but were significantly influenced by the porphyrin fluorescence. SAXS was selected in lieu of resonance light scattering experiments applied by others to ameliorate this problem for porphyrin macrocycles.[47-49,53-55] This decision was also motivated by the fact that DLS of extended structures at finite concentrations is not a trivial problem, even in the absence of the fluorescence, due to thermodynamic and hydrodynamic interactions which begin at very low concentrations for extended objects.[56] As noted by others,[57-59] SAXS measurements provide a good way forward, but perhaps even ultrasmall-angle X-ray scattering would prove insufficient to characterize the largest sizes present in fully formed aggregates. Our SAXS experiments were conducted at moderate spatial frequencies, $0.003\ \text{Å}^{-1} < q < 0.160\ \text{Å}^{-1}$, where $q = 4\pi\sin(\theta/2)/\lambda$ and θ is the scattering angle, in order to ascertain the nanometer-scale structural features of the aggregates reported in the only other SAXS study of the independent self-assembly of meso-tetra(4-sulfonatophenyl) porphyrin.[52] The use of high porphyrin concentrations (5-20 mM) is justified in this limit, which is fortuitous because SAXS does not enjoy the high sensitivity of UV-Vis and fluorescence spectroscopy. In addition to providing a point of contact with Ref. 52, scattering envelopes were evaluated for the effect of concentration, pH, time and ionic strength on aggregate formation.

The analysis begins with qualitative inspection of the scattering envelopes (Figure 3-4a). Oscillations within the scattering curves of the porphyrin solution at pH 4 are present at both 5 mM and 20 mM, as seen in Figure 3-4a. The only significant difference was in the scattering intensity. According to these results, the structure of the aggregates formed at pH 4 appears to be independent of the solution concentration. For the pH 9 solutions, there are no scattering features regardless of concentration, further suggesting the inhibition of large aggregate formation at high pH levels, and its independence of concentration.

The scattering envelopes evolve over time. Shown in Figure 3-4b are SAXS curves of the porphyrin solutions at pH 4 and 9, acquired 1, 3, and 4 days after solution preparation. The oscillation peaks became better defined gradually with time for the porphyrin solution at pH 4, while the curves remained almost unchanged for the solution at pH 9. These results suggest the diacid porphyrin species (i.e. H_4TPPS^{2-}) which exists at pH 4 diffuses and anneals into larger aggregates. To test whether this was indeed the case, SAXS envelopes for the porphyrin solution at pH 4 acquired either at 24 h or 2 weeks after preparation were obtained (Figure 3-5).

With time, the oscillations in the scattering curves become more defined and sharper, which indicates either a gain of order within the aggregate architecture, an increase in the size of the aggregates, or both. It lies beyond the scope of the present study to distinguish between these possibilities. The sharpening seems to occur at the expense of high-q amorphous scattering ($q >$ ~0.1 $Å^{-1}$), as if free, small molecules are becoming incorporated into the larger structure. The close match of data in the range $0.01 < q/Å^{-1} < 0.03$ would seem to suggest refinement of structures at constant size, but we do not have data (e.g., from static light scattering or ultra-small angle X-ray scattering) at still lower q values appropriate for the large structures observed in the next section. Earlier in the self-assembly process (less than 24 h), a mixture of different growing

aggregates and monomeric porphyrin units may account for the observed disorder; gradually, these form better-defined structures. Formation of the stabilized micron-sized and highly ordered aggregated species becomes more apparent as time passes.

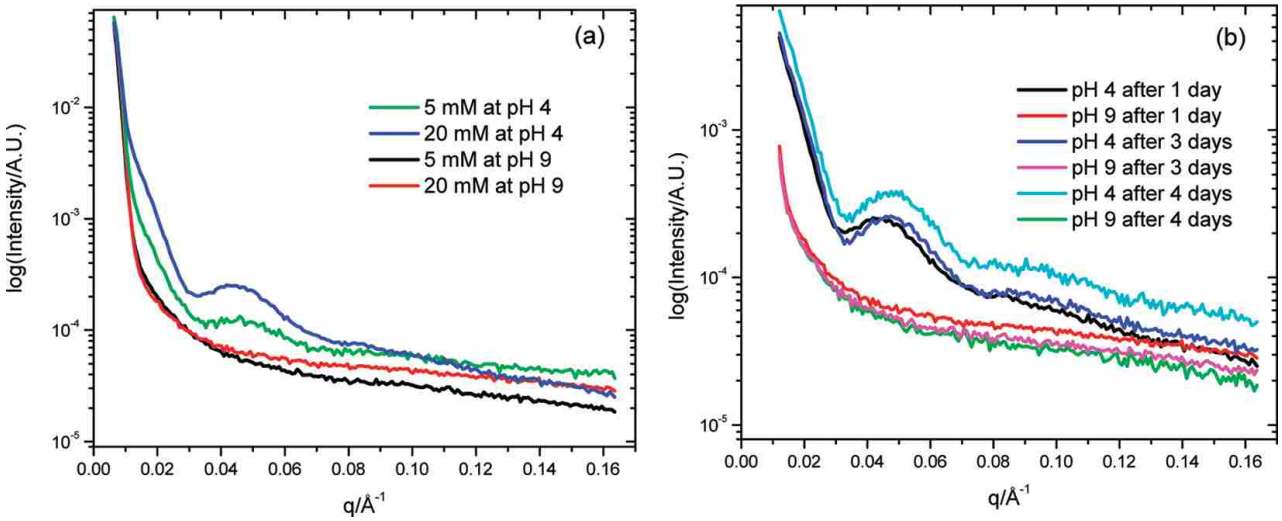

Figure 3-4 SAXS data of (a) 5 mM H_4TPPS^{2-} at pH 4 and H_2TPPS^{4-} at pH 9, and 20 mM H_2TPPS at pH 4 and pH 9 acquired 1 day after preparation. Similarities within the profiles of the scattering curves of each respective pH, as a function of concentration, suggest the structural features of the aggregates to be independent of concentration. (b) SAXS data of 20 mM H_4TPPS^{2-} at pH 4 acquired 1 day, 3 days, and 4 days after preparation. The amplitude and definition of two oscillation peaks increase as a function of time for pH 4 but the curves practically remain unchanged for pH 9 solution.

The oscillation peaks within the *q*-range of interest diminish as a function of increasing ionic strength, as shown in Figure 3-6. At high ionic strengths, the scattering curves for the pH 4 solution appear featureless, similar to those obtained for the pH 9 solutions, due to formation of large, randomly ordered porphyrin aggregates.[60] In contrast, at low ionic strength and pH 4, the porphyrins still form ordered aggregates.

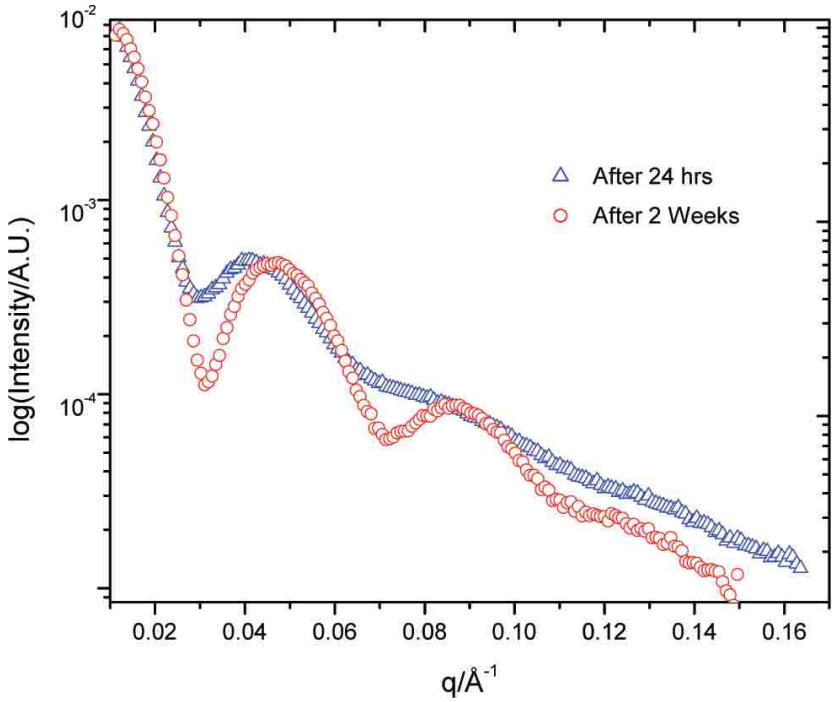

Figure 3-5 SAXS data of 20 mM H_4TPPS^{2-} at pH 4.0 acquired 24 hrs (Δ) and 2 weeks (○) after preparation using Method 4.

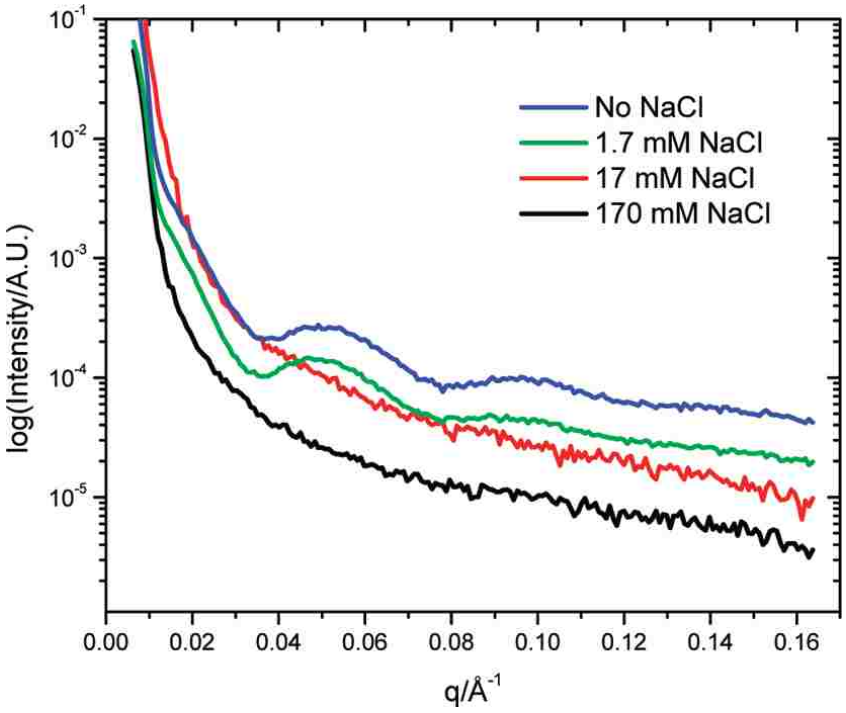

Figure 3-6 SAXS data for 10 mM H_4TPPS^{2-} at pH 4 with 0 mM, 1.7 mM, 17 mM, and 170 mM NaCl acquired 24 hrs after preparation using Method 4.

The quantitative evaluation of the SAXS results begins with traditional linearization schemes. The apparent R_g for the porphyrin aggregates according to the Guinier plot (Figure 3-7a) analysis is 130 ± 3 Å, which is consistent with the value reported by Gandini et al.[52] Due to the very large size of the aggregates and the chosen q-range, this value may under-represent the true size of aged fibrils. Because fibrillar structures are suspected, it is appropriate to consider a 2-D Guinier law,[61] which states that for long rods, the intensity is expected to obey $I(q) = I(q=0) \times q^{-1} e^{-q^2 R_{gc}^2/2}$ where R_{gc} is the *cross-sectional* radius of gyration:

$$R_{gc} = \left[\frac{\int_0^\infty \rho(s) s^2 ds}{\int_0^\infty \rho(s) ds} \right]^{1/2} . \qquad \text{Equation 3-1}$$

In this expression, $\rho(s)$ is the mass/area density in the cross-section. For a uniform disk of radius R, $R_{gc} = R/2$ while for a thin ring of radius R, $R_{gc} = R$. As revealed by the semilogarithmic representation of Figure 3-7b, a porphyrin sample at pH 4 does obey this relation at sufficiently high values of q, and $R_{gc} = 97 \pm 4$ Å. Also shown as an inset is a Casassa-Holtzer representation, $q \cdot I(q)$ vs q.[62-63] This type of plot is often used to estimate the persistence length of semiflexible filaments as $2\pi/q_{max}$, where q_{max} is the peak maximum.[64] In the present case, a persistence length of ~500 Å is estimated. This value is regarded as tentative, for two reasons. First, the porphyrin aggregates are not uniform in length; and, second, additional data at lower q would be desirable.

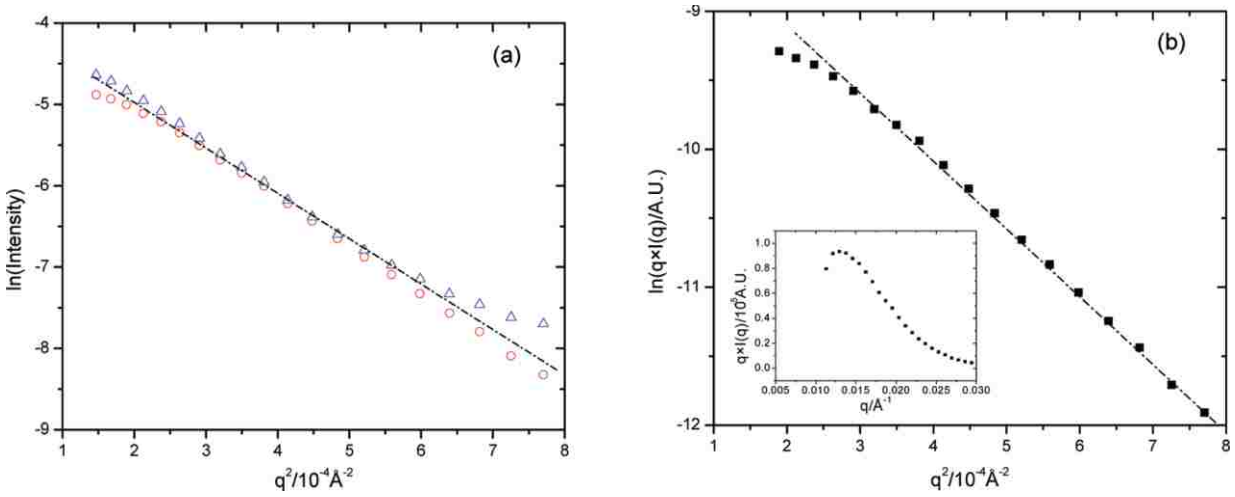

Figure 3-7 (a) Low-q Data of Figure 3-5 plotted in Guinier representation q for 20 mM H_4TPPS^{2-} at pH 4.0 24 hrs (Δ) and 2 weeks (○). The linear fit of the data corresponds to R_g = 130 ± 3 Å; (b) a two-dimensional Guinier representation yields a cross-sectional radius of gyration of R_{gc} of ~97 ± 4 Å. The inset is a Casassa-Holtzer representation ($qI(q)$ vs q) for the same SAXS data; see text.

The simple analysis afforded by traditional linearization schemes is broadly consistent with slightly extended, small assemblies of modest stiffness. For more detailed information about the shape of the aggregates at pH 4, the pair distance distribution function $P(r)$ was determined using the Irena 2 program.[40] The $P(r)$ data were then imported into the simulated annealing program DAMMIF, which applies the *ab initio* bead modeling method; see Figure 3-8a. For data in the measured q-range, it is expected that length polydispersity of the aggregates will have little effect on the outcome of the simulated annealing model. Two distinct sets of run commands were used for the DAMMIF program. In the first, bead models were generated using strictly default settings, assuming the structure is unknown. For the second set, known parameters near those obtained from the 2-D Guinier and Casassa-Holtzer plot analyses were used for a cylindrical search volume; see Figure 3-9. These results are combined with the following parameters as input to the program DAMMIF: inner radius = 70Å; outer radius = 120Å; height = 500Å; number of dummy atoms = 100,000; looseness penalty weight = 0; and, all other parameters set

to default. Both sets provided a hollow structure. The geometry obtained from the averaged simulations (Figure 3-8b) are consistent with the aggregate model proposed by Gandini et al.[52] in which 26 porphyrin macrocycles are arranged in a flat ring, then stacked to make a tube. The ring occupy number $n = 26$ can be obtained by solving

$$n \times 19\ \text{Å} \cong \text{tube circumference} \cong \pi \times 160\ \text{Å} \qquad \text{Equation 3-2}$$

where 19Å is the long dimension of a porphyrin macrocycle and 160Å is a fair estimate of the distance between the centers of two macrocycles located directly across from each other in the tube, taken as the maximum in the pair distance function (Figure 8a). The turning angle along the ring (i.e., the angle subtended by each macrocycle) is 360°/26 = 14°. The first (left) approximation in Eq. 2 is justified by the small difference between the sum of n chord lengths and the true circumference for such a small angle. The selection of 160 Å is somewhat arbitrary; if the diameter from 2D Guinier analysis, 194 ± 8Å, were used instead, then $n \cong 32$. Also, if partial macrocycle overlap occurs, as in the staircase model shown in Figure 1b, n would increase. Further discussion of partial overlap is deferred to Sec. 3.5 in connection with a possible model for the dilute solution aggregates.

The loss of scattering features as salt is added (Figure 3-6), along with SAXS results for the data acquired 24 h and 2 weeks after solution preparation by Method 4 (Figure 3-5), provide further insight about the structural properties. Together, these findings suggest that the cylinders can perfect their structures over time to a degree that depends on added salt, in agreement with the UV-Vis and fluorescence results above (Figure 3-3) and with previous investigations.[47] At sufficiently high concentrations, salt, aging, or both can lead to amorphous clusters that precipitate from solution. Indeed, this technique has been used for many years in porphyrin

extractions from aqueous media (brine) into organic phases by decreasing macrocycle solubility in the aqueous layer.

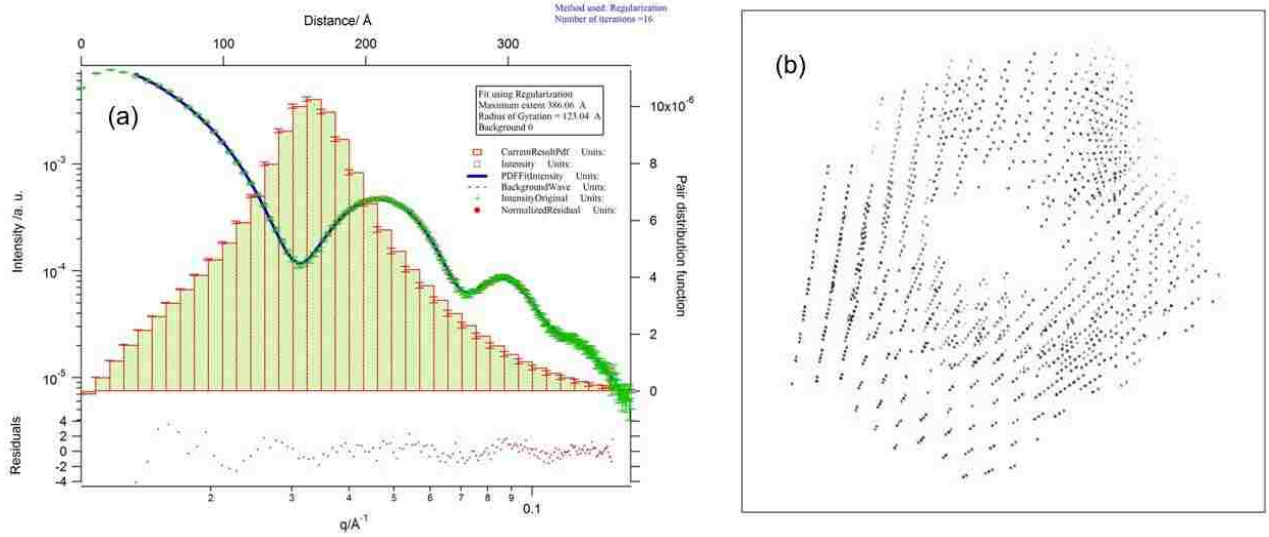

Figure 3-8 (a) Pair distance distribution function of 20 mM H_4TPPS^{2-}, generated from fitted small angle scattering data. (b) Simulated bead model of aggregates using the DAMMIF program. The indicated shape is a hollow cylinder.

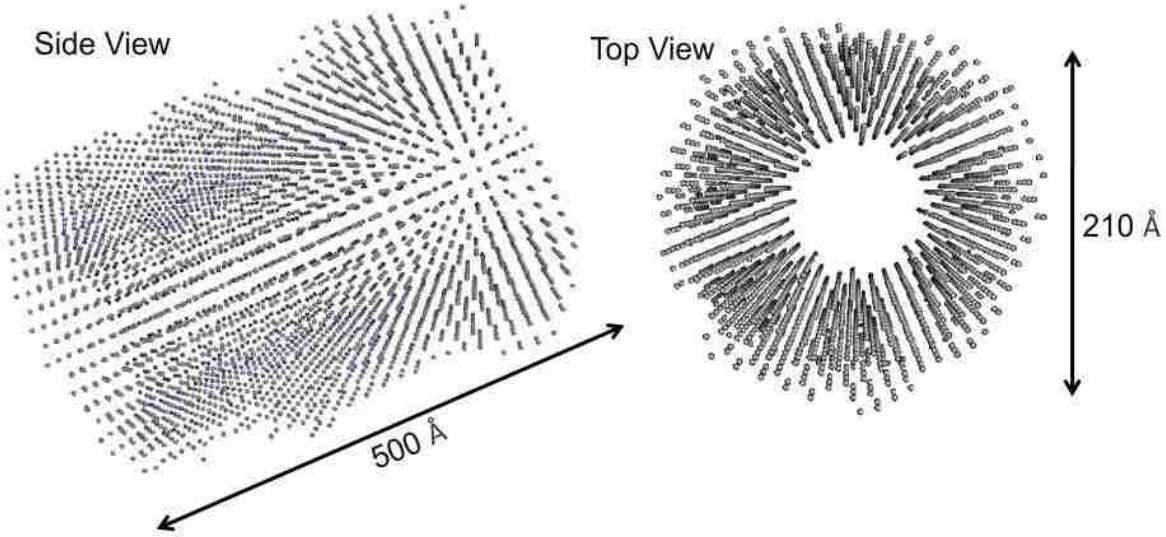

Figure 3-9 DAMMIF model derived using specified parameters.

After analyzing the data acquired from CAMD, more SAXS studies were conducted on synchrotron beamline 1-4 at the Stanford Synchrotron Radiation Research Lightsource (SRRL). As a result of the high flux of X-rays produced by this system, aggregation from lower porphyrin concentrations were detected. Figure 3-10 shows the scattering profile of 4 mM and 2 mM H_4TPPS^{2-}, which exhibits the same oscillations as the previous SAXS results. In an attempt to observe the limits of aggregate formation, a 9 μM solution of H_4TPPS^{2} at pH 4 was studied (see Figure 3-11). The dilute sample showed almost no scattering features. In the low-*q* regime, the scattering intensity from the buffer appeared higher than the sample. This occurrence may indicate the off-centering of the sample or inconsistencies in the sample cell thickness in comparison to that of the solvent cell.

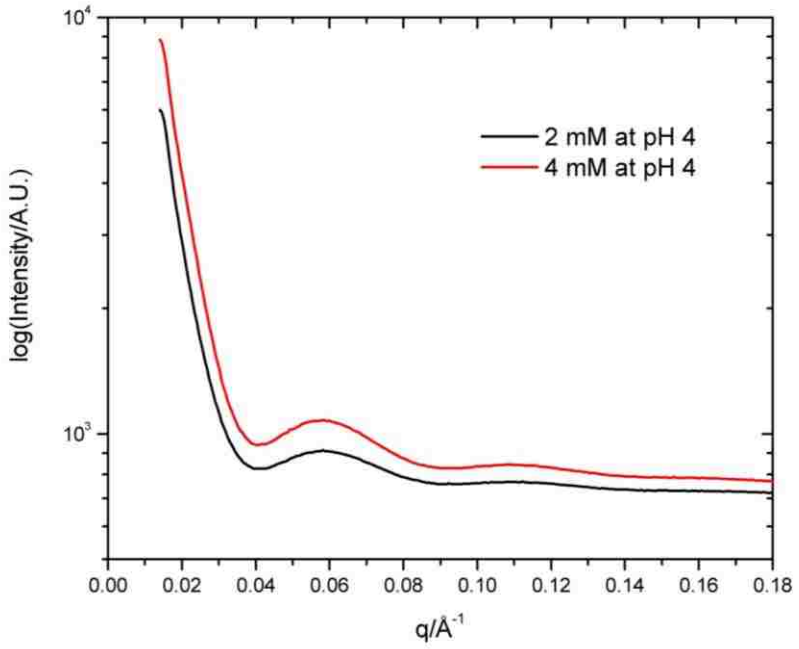

Figure 3-10 SAXS data for 2 mM (—) and 4 mM (—) H_4TPPS^{2-} at pH 4, acquired 24 hrs after preparation using Method 4.

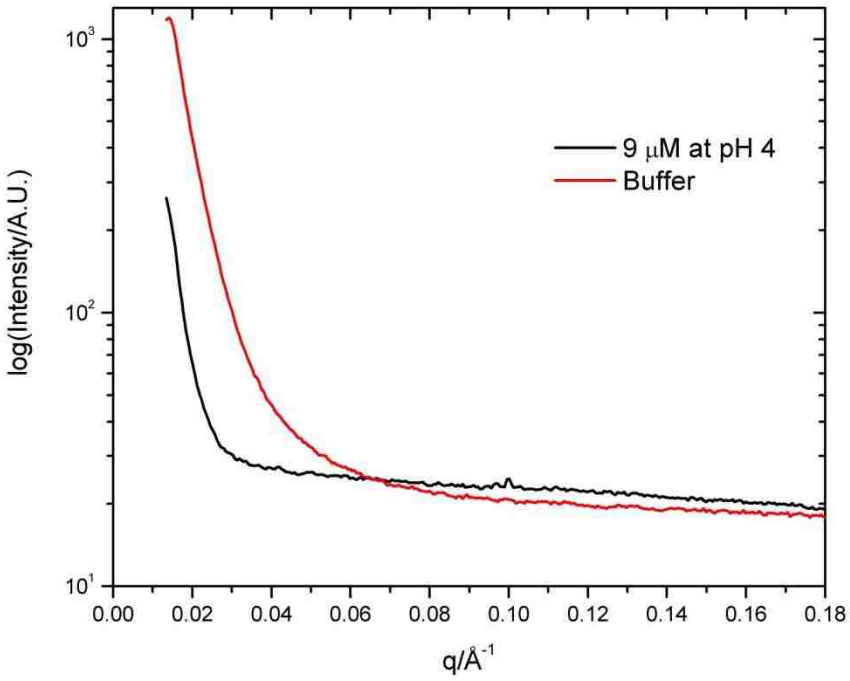

Figure 3-11 SAXS data for 9 μM H_4TPPS^{2-} at pH 4 (—) and buffer solution (—), acquired 24 hrs after preparation using Method 4.

3.3.3 Analytical Ultracentrifugation (AUC)

The UV-Vis, fluorescence, and SAXS results are largely in agreement with earlier reports, so it is appropriate to examine the details about the aggregate size at lower concentrations by AUC sedimentation equilibrium experiments. The absorbance vs. radius plot (equilibrium gradient) was transformed into a $M_{w,app}$ *vs.* concentration plot. This plot gives the slope ($M_{w,app}$) of a segment of data points (typically 10-40) in a ln(c) vs. r^2 plot across the radial path one data point at a time. Data obtained from this transformation provide information concerning the associative order of the system. For an associating system, the plot curves upward as the concentration increases. In addition, patterns in the residuals from the best-fit curves provide insight into the associative behavior. Residual patterns also confirmed the initial assumptions gathered from the $M_{w,app}$ vs. concentration plots.

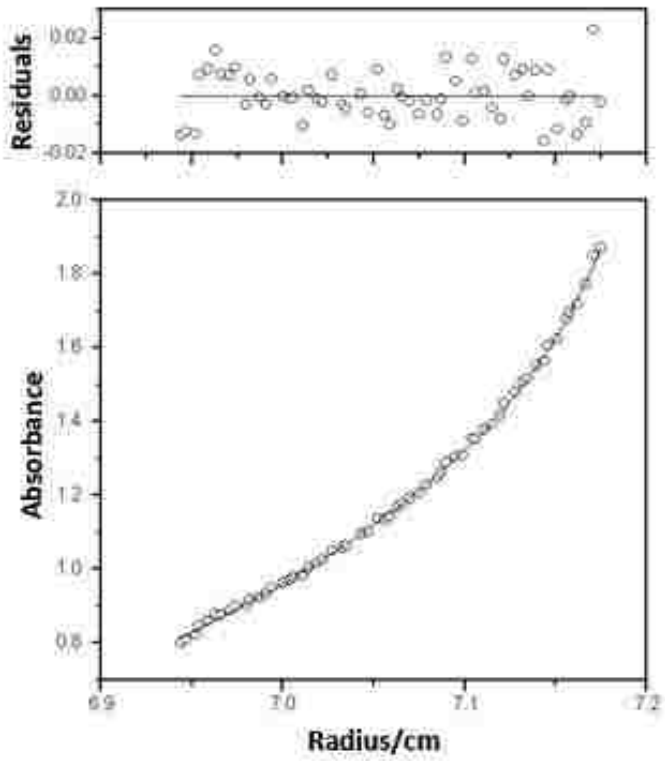

Figure 3-12 Representative sedimentation equilibrium data for pH 4 solution of 5.0 μM H_4TPPS^{2-}. The rotor speed was 45,000 RPM. Similar experiments were performed for H_2TPPS^{4-} in solution at pH 9.

According to the best fit model (Ideal 2 in the Beckman software), the average molecular weights for the H_4TPPS^{2-} aggregates formed at 3.0 μM and pH 4, one week after solution preparation, were Mw_1=25,400 ± 3,150 g·mol^{-1} and Mw_2=3,000 ± 75 g·mol^{-1} for components 1 and 2, respectively (Figure 3-12). The molar mass of a meso-tetra(4-sulfonatophenyl) porphyrin unit is 1022.9 g·mol^{-1}. Component 1 is therefore attributed to the formation of large aggregates containing ~25 ± 3 monomers, whereas component 2 suggests the co-existence of porphyrin trimers in this solution. In addition, the molecular weight of the aggregates (M_{w1}=25,400 ± 3,150 g·mol^{-1}) obtained by AUC is consistent with the SAXS results yielding the proposed aggregate structure bearing 26 porphyrin units in the cross-section. The existence at low concentrations of discrete structures with a mass that matches one layer of the "stacked ring" structure suggested by SAXS is intriguing and possibly coincidental, but the SAXS data (whether ours or those of

Gandini et al.) could as easily be explained by a helical array of units, as in tobacco mosaic virus.[52,65] Before the ring model is accepted on the basis of AUC and SAXS data, it should be mentioned that neither technique has the ability to rule out a "split washer" structure, in which one end of a broken ring lies a bit higher or lower than the opposite end. Such a structure, when stacked, yields a helix. Although these analytical techniques provided the same self-consistent picture, their required concentration for detection is very different (μm vs. mM), emphasizing the sensitivity of analytical ultracentrifugation with absorption detection. More importantly, this observation reveals the existence of 26-membered porphyrin units, even at dilute concentrations where the 490 nm absorption band is not present. Thus, relatively small J-aggregates exhibiting a very slight bathochromic shift exist among dimers and trimers which collectively account for the broad absorption band at ~430 nm (see section 3.2). Pasternack and co-workers reported[50] these species by resonance light scattering, and determined that the absorption band at 430 nm was due to either a monomer or a small aggregate. Our results reaffirm their findings, but also provide more quantitative details about the observed species.

Data obtained at pH 9 fit well to a model that assumed single component behavior (Ideal 1). Due to the weaker intermolecular interactions at pH 9 (consisting mainly of hydrogen bonding and hydrophobic forces), mostly small dimers were identified using this technique. The calculated average molecular weight of the dimers was $M_w = 2{,}700 \pm 50$ g·mol^{-1}. A plot of $M_{w,app}$ *vs.* concentration was generated to test for the presence of a single specie (Figure 3-13). For materials exhibiting single particle, ideal solute behavior, $M_{w,app}$ does not vary with concentration, however, the obtained plot systematically varies. This observation suggests that self-assembly is indeed occurring at pH 9, which could not be diagnosed using UV-Vis and fluorescence emission data. Previous reports assume that this porphyrin exists mainly in the

monomeric form at neutral and basic pH values. Our results show for the first time that even at high pH values water-soluble porphyrins can exist as dimers rather than monomers, in order to maximize hydrophobic and hydrogen bond interactions which overcome the electrostatic repulsion between the negatively charged groups at the porphyrin periphery. Indeed, we have recently reported [66] that an octa-anionic boronated porphyrin has strong tendency for aggregation in aqueous solutions at neutral pH, in the absence of NaCl.

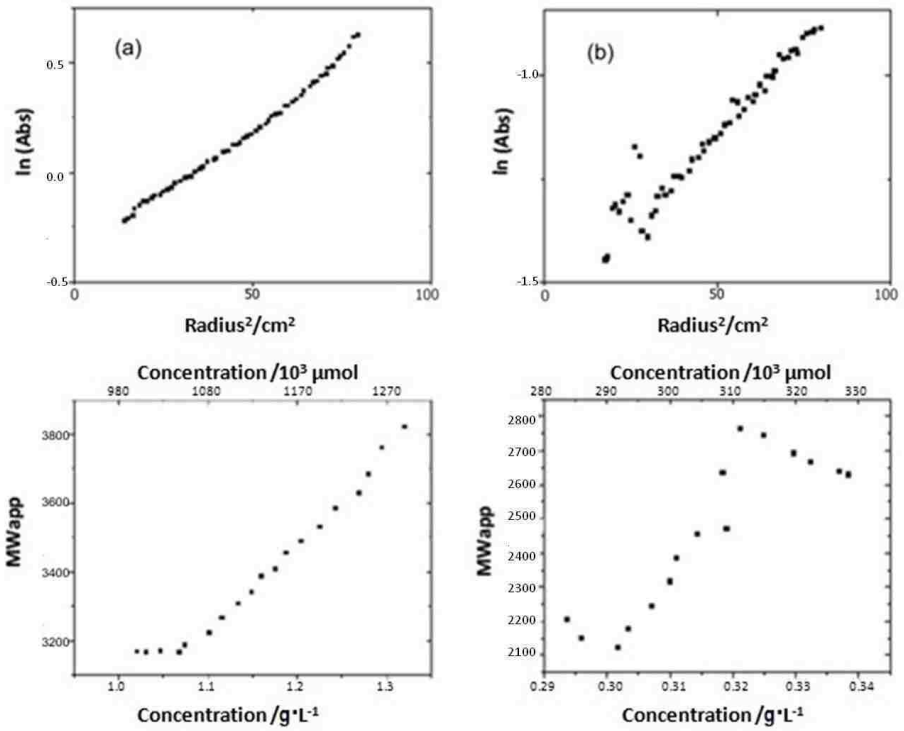

Figure 3-13 $M_{w,app}$ vs concentration plots of (a) H_2TPPS^{4-} in pH 4 solution and (b) H_2TPPS^{2-} in pH 9 solution. The self-association behavior is denoted by the curve of the ln(*c*) *vs.* r^2 and $M_{w,app}$ *vs.* concentration plots.

The species which absorbs at 490 nm was also studied using AUC. Samples were prepared by dilution of a high concentration (2 mM) stock solution of H_4TPPS^{2-}, and several attempts were made to determine the self-associative behavior and molecular weight. After observing the complete sedimentation of this species, even at the lowest rotor speed (1000 RPM), it was confirmed that the entities were too large to characterize using the available instrumentation.

Based on this, it was concluded that the species exhibiting 490 nm absorption is a long (micron-sized) cylindrical J-aggregate.[45,50]

3.3.4 Cryo and Freeze-Fracture Transmission Electron Microscopy

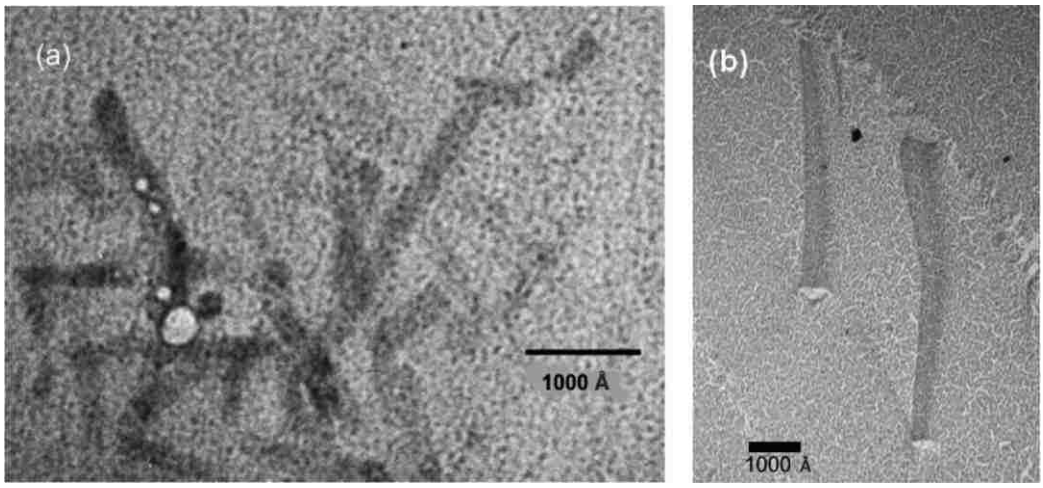

Figure 3-14 (a) Cryo- TEM and (b) FF-TEM image of rod-shaped aggregates of H_4TPPS^{2-} at pH 4.

Further examination of the size and shape of the porphyrin aggregates in their native environment at pH 4 was performed by TEM. Figure 3-14a shows a typical cryo-TEM image, which reveals and confirms the formation of rod-shaped aggregates, as previously observed by Vlaming et al. using cryo-electron microscopy.[67] Multiple rods are shown in the image, and the diameters all appear consistent in size. The average measured diameter of 62 rod-shaped aggregates was 190 ± 20Å. This is remarkably close to the cross-sectional diameter determined by 2D Guinier analysis of the SAXS data, 2 × 97Å = 194Å, as would be expected for a ring-shaped cross-section where most of the scattering elements are at the edge. The contour length of the filamentous structures varied from nanometers to the micrometers. Figure 3-14b shows a TEM image of the replicas of two hollow, cylindrical aggregates prepared by the freeze-fracture-etch method. Some variation in diameters is expected for hollow cylinders, as the fracture plane may be tilted with respect to the cylindrical axis. The replication process may alter dimensions,

too, but these images do confirm the presence of stiff cylinders. The linearity of the objects in cryo-TEM and their replicas in FF-TEM suggests that estimated persistence length from SAXS should be regarded as a lower bound. In combination with the molecular weight obtained by AUC, these observations suggest the formation of hollow cylindrical (tubular) aggregates containing 25-26 macrocycles in diameter, as a result of their stacking.

3.3.5 Plausible Aggregate Architectures

Based on the cyro-TEM and FF-TEM results, as well as the fluorescence, AUC and SAXS data, we drew plausible representations of porphyrin J-aggregates in tubular form (Figure 15) and prior to tube formation (Figure 16). Figure 13 for tubes resembles the flat ring model of Gandini et al.;[52] in which the macrocycles lie flat to create one layer of the tube. In our simplified representation, it is easy to see how macrocycles can experience zwitterionic and stacking interactions with molecules in adjacent layers, which is consistent with the fluorescence spectroscopy. Our results cannot distinguish this model from that of Vlaming et al.[67] These authors proposed partial overlap of the porphyrin molecules in two dimensions, resulting in a planar sheet. As a result of the overlap, which provides the stabilizing interactions without actually stacking layers, each macrocycle is tilted out of the plane by a small angle, $\theta \sim 20°$. To account for cylinder formation, the authors propose that the planar sheet is rolled; thus, the macrocycle lies on the surface of the cylinder. By contrast, in the model of Gandini et al., the plane of each macrocycle lies parallel to the cross-section of the cylinder. It is also not possible to rule out a hybrid of the two models in which macrocycles join to form a ring, but with tilting and partial overlap. This is effectively the staircase model (Figure 1b) wrapped into a ring (or split washer). Stacking these rings (washers) could still yield a tube (helical tube). The ring occupancy number would then be obtained by solving

$$n \times f \times 19\ \text{Å} \cong \text{tube circumference} \cong \pi \times 160\ \text{Å} \qquad \text{Equation 3-3}$$

where f is a parameter ($0 < f < 1$) reflecting the degree to which one macrocycle overlaps another. Figure 1b is drawn with $f \cong 0.5$, meaning that a negatively charged sulfate group on one porphyrin group is located near the tetrapyrrole center of a neighboring macrocycle. Overlap profoundly affects the ring occupancy number; for example, $n \cong 50$ if $f \cong 0.5$.

The situation is even less certain for the dilute solution aggregates. Equilibrium AUC provides vital information on the mass of the assemblies, but not their shape. Micali et al.,[68] who studied porphyrin aggregation by light scattering while taking care to exclude fluorescent light, reported a transition from fractal aggregates to rods. At pH 4, our AUC results instead show assemblies made from 25 ± 3 macrocycles. A single flat ring such as shown at the top of Figure 13 could account for the mass, but not for the fluorescence spectroscopy results, which demand J-type stacking. The tilted ring hybrid model described in the preceding paragraph is consistent with all our data, but structures of lower symmetry are easily imagined. In dilute solutions, the ring motif is merely a suggestion from the SAXS observations at higher concentrations. Placing 26 macrocycles into that ring is consistent with the AUC result (25 ± 3) but choosing 26 instead of another number in the experimental range again borrows from the nominal SAXS value at higher concentrations. If a 26-member ring is correct, and if an overlap parameter $f \cong 0.5$ is selected on the basis that such values enhance zwitterionic and stacking interactions, then a circumference of ~250Å is expected, corresponding to a predicted diameter of ~80Å. Measurement of such a particle at the concentrations required is non-trivial.

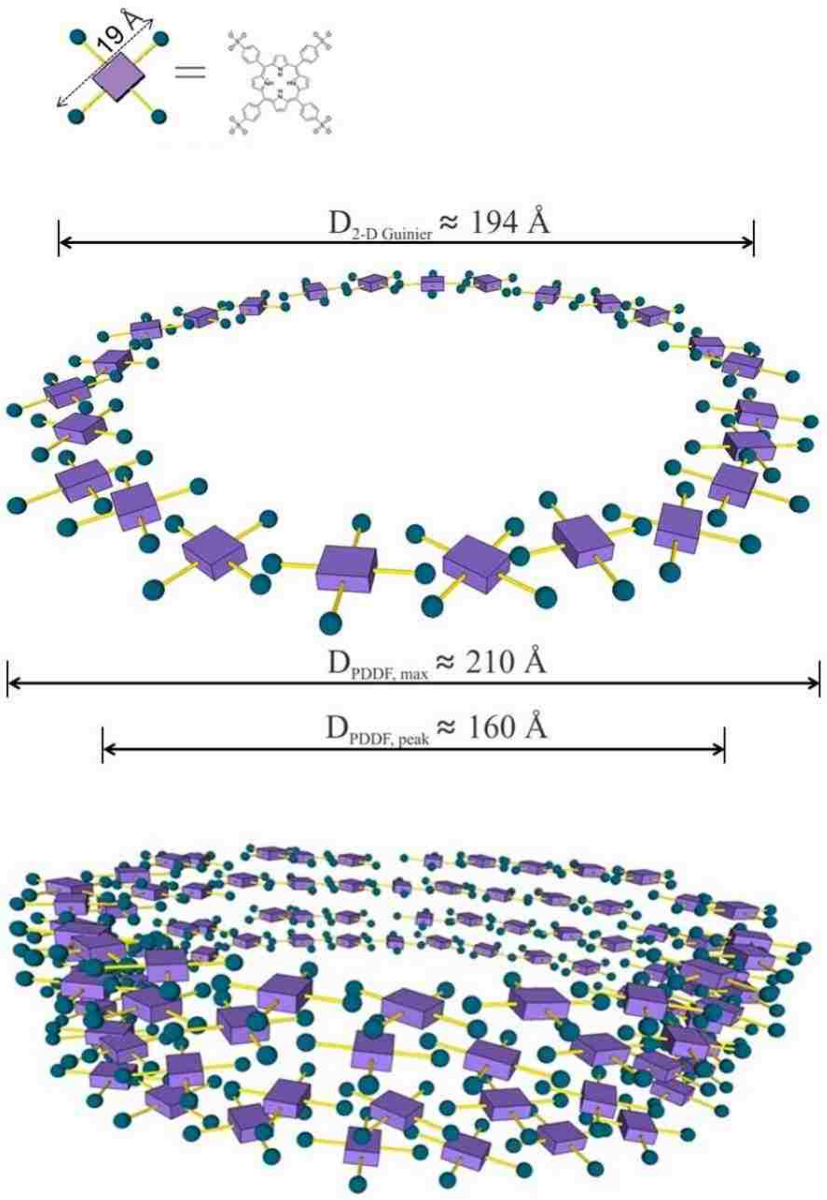

Figure 3-15 Stacked flat ring model of proposed structure of rod-like tubules formed at pH ≤ 4.

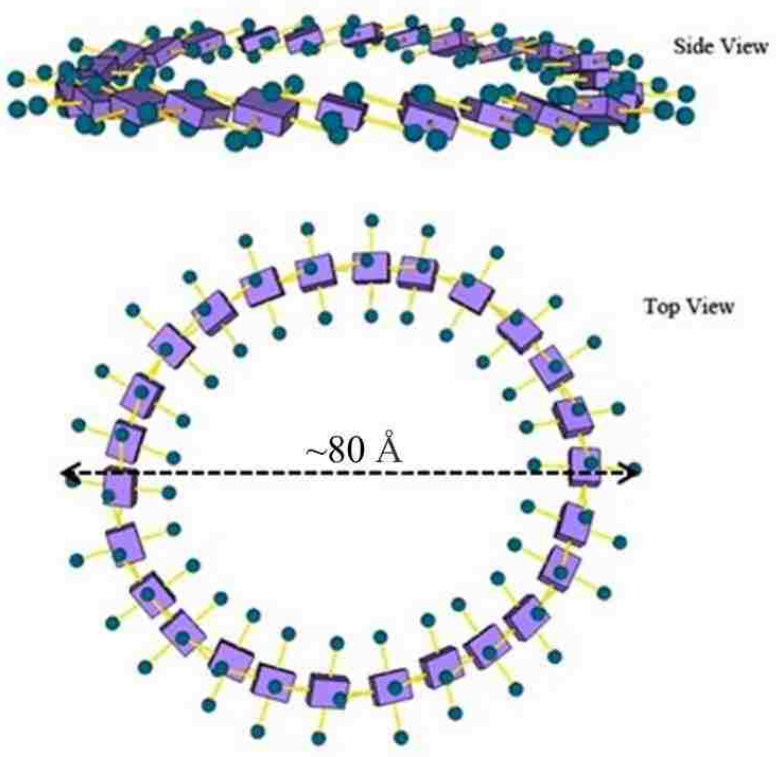

Figure 3-16 One possible model (of many) for the elemental aggregate species in dilute solutions for H_4TPPS^{2-} at pH ≤ 4. The porphyrin rings are tilted out of the plane of the ring and partially overlap with their immediate neighbors.

3.4 Conclusions

A series of complementary experiments and analytical methods was used to characterize porphyrin aggregates in aqueous solutions, as functions of concentration, solution pH, time, and ionic strength. UV-Vis and fluorescence spectra showed that H_2TPPS^{4-} forms J-type aggregates in dilute aqueous solutions, mainly dimers and trimers at neutral and basic solutions, and larger aggregates with 25 ± 3 porphyrin units at low pH values (pH 4), based on AUC data. The aggregate mass from AUC is consistent with a 26-member ring in which the macrocycles are tilted with respect to the plane of the ring, but other structures permitting stacking interactions are not excluded. The porphyrin is able to overcome electrostatic repulsion, even at high pH, forming aggregates as a result of electrostatic, hydrogen bonding and hydrophobic interactions.

In the absence of added NaCl (or at low ionic strength) and at low pH, the main aggregate species in aqueous solution is a particularly stable 26-unit structure. As the concentration is raised, the porphyrin molecules form hollow cylinders, as visualized by FF-TEM and modeled using DAMMIF for the SAXS data. Our results for tubular structures are consistent with those of Gandini et al., but we are unable to distinguish between that structure and the one suggested by Vlaming et al. It is not yet possible to rigorously exclude helix formation. With time and/or at high NaCl concentration, the aggregates grow, forming amorphous clusters that precipitate out of solution. Indeed, this technique has been used for many years in porphyrin extractions from aqueous media (using brine) and into organic phases, by decreasing their solubility in the aqueous layer. This study provides the basis for improved understanding of the self-assembly process of water-soluble porphyrins, and a foundation for investigation of more complex but related systems for specific applications, such as cancer therapeutics. Especially appealing avenues for further investigation include simulation to address the degree of overlap among the porphyrin molecules and possible helix formation, and high-sensitivity, low-noise methods for structure determination at very low concentrations.

3.5 Acknowledgements

This research was partially funded by NIH R01 CA098902 and by NSF DMR-1005707. We thank Dr. Irina Nesterova, Dr. Derek Dorman and Mr. Andrew Weber for providing training in the analytical techniques and methods that were essential to this work. We thank Drs. Olga Borkhsenious, William Henk, Xiaochu Wu, and Jibao He for assistance in acquiring and interpreting TEM images. Data used in this publication were collected at the Small Angle X-ray Scattering (SAXS) beam line at the Center for Advanced Microstructures and Devices (CAMD). This beam line was constructed with partial funding from NSF DGE-9987603.

3.6 References

(1) Fendler, J. H. Chemical Self-assembly for Electronic Applications. *Chem. Mater.* **2001**, *13*, 3196-3210.

(2) Sun, S. Recent Advances in Chemical Synthesis, Self-Assembly, and Applications of FePt Nanoparticles. *Adv. Mater.* **2006**, *18*, 393-403.

(3) Bensaude-Vincent, B. Self-Assembly, Self-Organization: Nanotechnology and Vitalism. *NanoEthics* **2009**, *3*, 31-42.

(4) Whitesides, G. M.; Grzybowski, B. Self-Assembly at All Scales. *Science* **2002**, *295*, 2418-2421.

(5) de Miguel, G., Martín-Romero MT, Pérez-Morales M, Muñoz E, Camacho L Controlling the molecular organization of porphyrins by hosting in amphiphilic matrix. *J. Porphyrins Phthalocyanines* **2009**, *13*, 597-605.

(6) Lauceri, R.; De Napoli, M.; Mammana, A.; Nardis, S.; Romeo, A.; Purrello, R. Hierarchical self-assembly of water-soluble porphyrins. *Synth. Met.* **2004**, *147*, 49-55.

(7) Kiba, T.; Suzuki, H.; Hosokawa, K.; Kobayashi, H.; Baba, S.; Kakuchi, T.; Sato, S.-i. Supramolecular J-Aggregate Assembly of a Covalently Linked Zinc Porphyrin−β-cyclodextrin Conjugate in a Water/Ethanol Binary Mixture. *J. Phys. Chem. B* **2009**, *113*, 11560-11563.

(8) Santiago PS; Gandini SCM; Moreira LM; Tabak M Interaction of cationic water-soluble meso-tetrakis(4-N-methylpyridiniumyl)porphyrin (TMPyP) with ionic and nonionic micelles: aggregation and binding. *J. Porphyrins Phthalocyanines* **2008**, *12*, 942-952.

(9) Santra, S.; Mukherjee, T. K.; Babel, N.; Gupta, I.; Datta, A.; Ravikanth, M. Synthesis, aggregation and photoinduced electron transfer processes of cationic water-soluble 21-thia and 21-oxaporphyrins. *J. Photochem. Photobiol. A* **2008**, *193*, 166-177.

(10) Collini, E.; Ferrante, C.; Bozio, R. Influence of Excitonic Interactions on the Transient Absorption and Two-Photon Absorption Spectra of Porphyrin J-Aggregates in the NIR Region. *J. Phys. Chem. C* **2007**, *111*, 18636-18645.

(11) Andrade, S. M.; Costa, S. M. B. Ordered Self-assembly of Protonated Porphyrin Induced by the Aqueous Environment of Biomimetic Systems. *Ann. N.Y. Acad. Sci.* **2008**, *1130*, 305-313.

(12) De Napoli, M.; Nardis, S.; Paolesse, R.; Vicente, M. G. H.; Lauceri, R.; Purrello, R. Hierarchical Porphyrin Self-Assembly in Aqueous Solution. *J. Am. Chem. Soc.* **2004**, *126*, 5934-5935.

(13) Eisfeld, A.; Briggs, J. S. The J- and H-bands of organic dye aggregates. *Chem. Phys.* **2006**, *324*, 376-384.

(14) Hosomizu, K.; Oodoi, M.; Umeyama, T.; Matano, Y.; Yoshida, K.; Isoda, S.; Isosomppi, M.; Tkachenko, N. V.; Lemmetyinen, H.; Imahori, H. Substituent Effects of Porphyrins on Structures and Photophysical Properties of Amphiphilic Porphyrin Aggregates. *J. Phys. Chem. B* **2008**, *112*, 16517-16524.

(15) Drain, C. M.; Varotto, A.; Radivojevic, I. Self-Organized Porphyrinic Materials. *Chem. Rev.* **2009**, *109*, 1630-1658.

(16) Castriciano, M. A.; Donato, M. G.; Villari, V.; Micali, N.; Romeo, A.; Scolaro, L. M. Surfactant-like Behavior of Short-Chain Alcohols in Porphyrin Aggregation. *J. Phys. Chem. B* **2009**, *113*, 11173-11178.

(17) Castriciano, M. A.; Romeo, A.; Villari, V.; Micali, N.; Scolaro, L. M. Nanosized Porphyrin J-Aggregates in Water/AOT/Decane Microemulsions. *J. Phys. Chem. B* **2004**, *108*, 9054-9059.

(18) Gao, Y.; Zhang, X.; Ma, C.; Li, X.; Jiang, J. Morphology-Controlled Self-Assembled Nanostructures of 5,15-Di[4-(5-acetylsulfanylpentyloxy)phenyl]porphyrin Derivatives. Effect of Metal−Ligand Coordination Bonding on Tuning the Intermolecular Interaction. *J. Am. Chem. Soc.* **2008**, *130*, 17044-17052.

(19) Medforth, C. J.; Wang, Z.; Martin, K. E.; Song, Y.; Jacobsen, J. L.; Shelnutt, J. A. Self-assembled porphyrin nanostructures. *Chem. Commun.* **2009**, 7261-7277.

(20) Ogawa, T.; Tokunaga, E.; Kobayashi, T. Giant electrooptic response of excitons in porphyrin J-aggregates. *Chem. Phys. Lett.* **2005**, *408*, 186-191.

(21) Wasielewski, M. R. Energy, Charge, and Spin Transport in Molecules and Self-Assembled Nanostructures Inspired by Photosynthesis. *J. Org. Chem.* **2006**, *71*, 5051-5066.

(22) Carvalho, V. C. M.; Melo, C. A. S.; Bagnato, V. S.; Perussi, J. R. Comparison of the Effects of Cationic and Anionic Porphyrins in Tumor Cells under Illumination of Argon Ion Laser. *Laser Physics* **2002**, *12*, 1314-1319.

(23) Kuciauskas, D.; Caputo, G. A. Self-Assembly of Peptide−Porphyrin Complexes Leads to pH-dependent Excitonic Coupling. *J. Phys. Chem. B* **2009**, *113*, 14439-14447.

(24) Andrade, S.; Costa, S.; Borst, J.; van Hoek, A.; Visser, A. Translational and Rotational Motions of Albumin Sensed by a Non-Covalent Associated Porphyrin Under Physiological and Acidic Conditions: A Fluorescence Correlation Spectroscopy and Time Resolved Anisotropy Study. *J. Fluoresc.* **2008**, *18*, 601-610.

(25) Pasternack, R. F.; Gibbs, E. J.; Bruzewicz, D.; Stewart, D.; Engstrom, K. S. Kinetics of Disassembly of a DNA-Bound Porphyrin Supramolecular Array. *J. Am. Chem. Soc.* **2002**, *124*, 3533-3539.

(26) Maiti, N. C.; Mazumdar, S.; Periasamy, N. J- and H-Aggregates of Porphyrin−Surfactant Complexes: Time-Resolved Fluorescence and Other Spectroscopic Studies†. *J. Phys. Chem. B* **1998**, *102*, 1528-1538.

(27) Paulo, P. M. R.; Gronheid, R.; De Schryver, F. C.; Costa, S. M. B. Porphyrin−Dendrimer Assemblies Studied by Electronic Absorption Spectra and Time-Resolved Fluorescence. *Macromolecules* **2003**, *36*, 9135-9144.

(28) Wu, J.-J.; Ma, H.-L.; Mao, H.-S.; Wang, Y.; Jin, W.-J. Investigation on disassociation of porphyrin J-aggregates induced by [beta]-cyclodextrins using absorption and fluorescence spectroscopy. *J. Photochem. Photobiol. A* **2005**, *173*, 296-300.

(29) Hasobe, T.; Fukuzumi, S.; Kamat, P. V. Ordered Assembly of Protonated Porphyrin Driven by Single-Wall Carbon Nanotubes. J- and H-Aggregates to Nanorods. *J. Am. Chem. Soc.* **2005**, *127*, 11884-11885.

(30) De Luca, G.; Romeo, A.; Villari, V.; Micali, N.; Foltran, I.; Foresti, E.; Lesci, I. G.; Roveri, N.; Zuccheri, T.; Scolaro, L. M. Self-Organizing Functional Materials via Ionic Self Assembly: Porphyrins H- and J-Aggregates on Synthetic Chrysotile Nanotubes. *J. Am. Chem. Soc.* **2009**, *131*, 6920-6921.

(31) Wu, J.-J.; Li, N.; Li, K.-A.; Liu, F. J-Aggregates of Diprotonated Tetrakis(4-sulfonatophenyl)porphyrin Induced by Ionic Liquid 1-Butyl-3-Methylimidazolium Tetrafluoroborate. *J. Phys. Chem. B* **2008**, *112*, 8134-8138.

(32) Jiang, S.; Zhang, L.; Liu, M. Photo-triggered J-aggregation and chiral symmetry breaking of an anionic porphyrin (TPPS) in mixed organic solvent. *Chem. Commun.* **2009**, 6252-6254.

(33) Gelfuso, G. M.; Figueiredo, F. V.; Gratieri, T.; Lopez, R. F. V. The effects of pH and ionic strength on topical delivery of a negatively charged porphyrin (TPPS4). *J. Pharm. Sci.* **2008**, *97*, 4249-4257.

(34) Franke, D.; Svergun, D. I. DAMMIF, a program for rapid ab-initio shape determination in small-angle scattering. *J. Appl. Crystallogr.* **2009**, *42*, 342-346.

(35) Joubert, A. M.; Byrd, A. S.; LiCata, V. J. Global Conformations, Hydrodynamics, and X-ray Scattering Properties of Taq and Escherichia coli DNA Polymerases in Solution. *J. Biol. Chem.* **2003**, *278*, 25341-25347.

(36) Jamison, J. A.; Krueger, K. M.; Mayo, J. T.; Yavuz, C. T.; Redden, J. J.; Colvin, V. L. Applying analytical ultracentrifugation to nanocrystal suspensions. *Nanotechnology* **2009**, *20*, 1-10.

(37) Kovaric, B. C.; Kokona, B.; Schwab, A. D.; Twomey, M. A.; de Paula, J. C.; Fairman, R. Self-Assembly of Peptide Porphyrin Complexes: Toward the Development of Smart Biomaterials. *J. Am. Chem. Soc.* **2006**, *128*, 4166-4167.

(38) Satake, A.; Kobuke, Y. Dynamic supramolecular porphyrin systems. *Tetrahedron* **2005**, *61*, 13-41.

(39) Durchschlag H; Zipper P Calculation of the partial volume of organic compounds and polymers. *Prog. Colloid Polym. Sci.* **1994**, *94*, 20-39.

(40) Ilavsky, J.; Jemian, P. R. Irena: tool suite for modeling and analysis of small-angle scattering. *J. Appl. Crystallogr.* **2009**, *42*, 347-353.

(41) Konarev, P. V.; Volkov, V. V.; Sokolova, A. V.; Koch, M. H. J.; Svergun, D. I. PRIMUS: a Windows PC-based system for small-angle scattering data analysis. *J. Appl. Crystallogr.* **2003**, *36*, 1277-1282.

(42) Volkov, V. V.; Svergun, D. I. Uniqueness of ab initio shape determination in small-angle scattering. *J. Appl. Crystallogr.* **2003**, *36*, 860-864.

(43) Ribo, J. M.; Crusats, J.; Farrera, J.-A.; Valero, M. L. Aggregation in water solutions of tetrasodium diprotonated meso-tetrakis(4-sulfonatophenyl)porphyrin. *J. Chem. Soc., Chem. Commun.* **1994**, 681-682.

(44) Castriciano, M. A.; Romeo, A.; Villari, V.; Angelini, N.; Micali, N.; Scolaro, L. M. Aggregation Behavior of Tetrakis(4-sulfonatophenyl)porphyrin in AOT/Water/Decane Microemulsions. *J. Phys. Chem. B* **2005**, *109*, 12086-12092.

(45) Ohno, O.; Kaizu, Y.; Kobayashi, H. J-aggregate formation of a water-soluble porphyrin in acidic aqueous media. *J. Chem. Phys.* **1993**, *99*, 4128-4139.

(46) Aggarwal, L. P. F.; Baptista, M. S.; Borissevitch, I. E. Effects of NaCl upon TPPS4 triplet state characteristics and singlet oxygen formation. *J. Photochem. Photobiol. A* **2007**, *186*, 187-193.

(47) Micali, N.; Mallamace, F.; Romeo, A.; Purrello, R.; Monsù Scolaro, L. Mesoscopic Structure of meso-Tetrakis(4-sulfonatophenyl)porphine J-Aggregates. *J. Phys. Chem. B* **2000**, *104*, 5897-5904.

(48) Aggarwal, L. P. F.; Borissevitch, I. E. On the dynamics of the TPPS4 aggregation in aqueous solutions: Successive formation of H and J aggregates. *Spectrochimica Acta Part A* **2006**, *63*, 227-233.

(49) Ma, H.-L.; Jin, W.-J. Studies on the effects of metal ions and counter anions on the aggregate behaviors of meso-tetrakis(p-sulfonatophenyl)porphyrin by absorption and fluorescence spectroscopy. *Spectrochimica Acta Part A* **2008**, *71*, 153-160.

(50) Pasternack, R. F.; Schaefer, K. F.; Hambright, P. Resonance light-scattering studies of porphyrin diacid aggregates. *Inorg. Chem.* **1994**, *33*, 2062-2065.

(51) Parkash, J.; Robblee, J. H.; Agnew, J.; Gibbs, E.; Collings, P.; Pasternack, R. F.; de Paula, J. C. Depolarized Resonance Light Scattering by Porphyrin and Chlorophyll a Aggregates. *Biophys. J.* **1998**, *74*, 2089-2099.

(52) Gandini, S. C. M.; Gelamo, E. L.; Itri, R.; Tabak, M. Small Angle X-Ray Scattering Study of Meso-Tetrakis (4-Sulfonatophenyl) Porphyrin in Aqueous Solution: A Self-Aggregation Model. *Biophys. J.* **2003**, *85*, 1259-1268.

(53) Rubires, R.; Crusats, J.; El-Hachemi, Z.; Jaramillo, T.; Lopez, M.; Valls, E.; Farrera, J.-A.; M. Ribo, J. Self-assembly in water of the sodium salts of meso-sulfonatophenyl substituted porphyrins. *New J. Chem.* **1999**, *23*, 189-198.

(54) Pasternack, R. F.; Bustamante, C.; Collings, P. J.; Giannetto, A.; Gibbs, E. J. Porphyrin assemblies on DNA as studied by a resonance light-scattering technique. *J. Am. Chem. Soc.* **1993**, *115*, 5393-5399.

(55) Lauceri, R.; Purrello, R.; Shetty, S. J.; Vicente, M. G. H. Interactions of Anionic Carboranylated Porphyrins with DNA. *J. Am. Chem. Soc.* **2001**, *123*, 5835-5836.

(56) Tracy, M. A.; Pecora, R. Dynamics of Rigid and Semirigid Rodlike Polymers. *Annu. Rev. Phys. Chem.* **1992**, *43*, 525-557.

(57) Sullivan, M. C.; Sprafke, J. K.; Kondratuk, D. V.; Rinfray, C.; Claridge, T. D. W.; Saywell, A.; Blunt, M. O.; Shea, J. N.; Beton, P. H.; Malfois, M.; Anderson, H. L. Vernier templating and synthesis of a 12-porphyrin nano-ring. *Nature* **2011**, *469*, 72-75.

(58) Terech, P.; Gebel, G.; Ramasseul, R. Molecular Rods in a Zinc(II) Porphyrin/Cyclohexane Physical Gel: Neutron and X-ray Scattering Characterizations. *Langmuir* **1996**, *12*, 4321-4323.

(59) Sasaki, K.; Nakagawa, H.; Zhang, X.; Sakurai, S.; Kano, K.; Kuroda, Y. Construction of porphyrin-cyclodextrin self-assembly with molecular wedge. *Chem. Commun.* **2004**, 408-409.

(60) Monsù Scolaro, L.; Castriciano, M.; Romeo, A.; Mazzaglia, A.; Mallamace, F.; Micali, N. Nucleation effects in the aggregation of water-soluble porphyrin aqueous solutions. *Physica A* **2002**, *304*, 158-169.

(61) Cohen, Y.; Talmon, Y.; Thomas, E. L. In Physical Networks. In *Physical Networks: Polymers and Gels*; Burchard, W., Ross-Murphy, S. B., Eds.; Elsevier: London and New York, 1990, p 147-159.

(62) Casassa, E. F. Light Scattering from Very Long Rod-Like Particles and an Application to Polymerized Fibrinogen. *J. Chem. Phys.* **1955**, *23*, 596-597.

(63) Holtzer, A. Interpretation of the angular distribution of the light scattered by a polydisperse system of rods. *J. Polym. Sci.* **1955**, *17*, 432-434.

(64) Guérin, G.; Wang, H.; Manners, I.; Winnik, M. A. Fragmentation of Fiberlike Structures: Sonication Studies of Cylindrical Block Copolymer Micelles and Behavioral Comparisons to Biological Fibrils. *J. Am. Chem. Soc.* **2008**, *130*, 14763-14771.

(65) Klug, A. The tobacco mosaic virus particle: structure and assembly. *Phil. Trans. R. Soc. B* **1999**, *354*, 531-535.

(66) Hao, E.; Sibrian-Vazquez, M.; Serem, W.; Garno, J. C.; Fronczek, F. R.; Vicente, M. G. H. Synthesis, Aggregation and Cellular Investigations of Porphyrin–Cobaltacarborane Conjugates. *Chem. Eur. J.* **2007**, *13*, 9035-9042.

(67) Vlaming, S. M.; Augulis, R.; Stuart, M. C. A.; Knoester, J.; van Loosdrecht, P. H. M. Exciton Spectra and the Microscopic Structure of Self-Assembled Porphyrin Nanotubes. *J. Phys. Chem. B* **2009**, *113*, 2273-2283.

CHAPTER 4 SYNTHESIS AND CHARACTERIZATION OF PORPHYRINS CONJUGATED TO SILICA-COATED SUPERPARAMAGNETIC IRON OXIDE NANOPARTICLES

4.1 Introduction

Porphyrins and some of their derivatives are often used as photosensitizers in photodynamic therapy (PDT), which is a well-established noninvasive antitumor treatment. Since the clinical debut of Photofrin®, a vast number of porphyrin-based photosensitizers have been reported, but there are still ongoing challenges to overcome. One major challenge involves improving the tumor selectivity and specificity of photosensitizers because tumor cells have nonspecific affinity to porphyrins. In an effort to address this issue, researchers have tried to direct photosensitizers to cellular targets by conjugation to ligands that are tumor-specific.[1-4] Another recent approach includes nanotechnology, which is an interdisciplinary field with applications in chemistry, material science, electronics, defense, energy and medicine.[5] The use of platforms, such as nanoparticles, offers several significant benefits for PDT: (1) large payloads of photosensitizer can be added to the nanoparticles, and the particle surface can be modified to achieve the desired hydrophilicity for optimal plasma pharmacokinetics. (2) The attachment of targeting moieties onto the nanoparticle surface may permit increased selective delivery of the photosensitizers. (3) High levels of imaging agents can easily be combined with photosensitizers in the nanoparticles, providing an enhanced "see and treat" approach, where the placement of optical fibers is fluorescence image-guided to direct photoactivating light to subsurface tumors or to early nonclinically evident diseased tissue.[1] Moreover, the development of nanoparticles engineered for PDT can overcome many of the shortcomings of conventional photosensitizers.[6-8]

Overall, the photochemical process for PDT involves exciting a photosensitizing agent with visible light, which induces cytotoxicity in the presence of tissue oxygen as a result of producing

reactive oxygen species (ROS). The ROS are the responsible components for invoking cell death and destruction of tumors.[9] Efficiency of these species depends on the photosensitizer undergoing intersystem crossing to the excited triplet state upon activation. When intracellular porphyrin aggregation occurs, the efficiency of the aforementioned process is limited due to self-quenching effects. On the other hand, aggregation facilitates the collective transport of photosensitizers to local tumor sites, minimizing incidental destruction of healthy cells. The development of a controllable "on/off" switch for aggregation would simultaneously optimize the transport and efficacy of porphyrins under both, extra- and intracellular conditions, respectively. Using polypeptide-functionalized silica particles as platforms may offer the necessary features to promote the aforementioned research goal. The inclusion of a magnetic moiety (i.e. iron oxide, which is FDA-approved) within the silica core provides an additional dimension for controlling drug transportation. In the presence of a remotely controlled high frequency magnetic field, superparamagnetic colloidal particles assemble.[10] Upon removal of the magnetic field, the particles are capable of readily dispersing.[11] Exploiting these features may increase the reactivity of photosensitizers and minimize the required dosage.[12]

In this chapter, hybrid nanocomposites composed of superparamagnetic silica-coated magnetite (Fe_3O_4@SiO_2) are covalently attached to polypeptide-porphyrin conjugates using Cu(I)-catalyzed Huisgen 1,3-dipolar cycloaddition, also known as click chemistry. This grafting mechanism is a rapid chemoselective approach that takes advantage of the alkyne/azide functional groups by forming a very stable 1,2,3-triazole between the alkyne-terminated PCBL and azido-functionalized Fe_3@SiO_2 composite. In general, the grafted homopolypeptide, alkyne-terminated poly(N_ε-carbobenzyoxy-L-lysine) (PCBL), inherently provides a hydrophilic poly-L-lysine shell after undergoing debenzylation. Such practical features constitute the

biocompatibility and versatility of these potential drug delivery systems.[13] serve as drug delivery systems and biomedical devices A few other potential applications for this composite include: responsive materials, chiral separations,[14] colloidal crystallization,[15] catalysis,[16] and biomimetic membrane supports.[17] Depending on the properties of the attached polypeptide, the particles can exhibit solubility in water or organic solvents. In addition, the polypeptide coil⇔helix transition is a useful characteristic for modifying the surface configuration and particle-particle interactions.

The present work also introduces an approach for efficiently attaching porphyrins directly to Fe_3O_4@SiO_2 nanoparticles without the mediated assistance of an alkyne-terminated polypeptide conjugate. In a similar report, Liu et al.[18] described a procedure for preparing magnetic nanocomposite-bonded metalloporphyrins for biomimetic catalysis. In their approach, metalloporphyrins were synthesized via a silanation reaction between 3-aminopropyltriethoxysilane (APTES) functionalized metalloporphyrins and Fe_3O_4@SiO_2 nanoparticles. The target porphyrin species was prepared by amidation of its acyl chloride group with APTES. In contrast, the studies herein demonstrate the attachment of alkyne-functionalized porphyrin to azido-functionalized Fe_3O_4@SiO_2 by click chemistry.

4.2 Experimental

4.2.1 Materials

N_ε-carbobenzyoxy-L-lysine (CBL) (99%), *tert*-butanol (99.5%), triethylamine (99.5%), triphosgene (98%), anhydrous dichloromethane, propargylamine (98%), dimethylformamide (DMF), dimethyl sulfoxide (DMSO), hydrogen bromide (HBr, 33% solution on acetic acid), trifluoroacetic acid (TFA), trisodium citrate, tetraethylorthosilicate (TEOS), benzotriazol-1-yl-oxytripyrrolidinophosphonium hexafluorophosphate (PyBOP), CuBr (99%), *N*,*N*-

diisopropylethylamine (DIEA), *N*,*N'*,*N'*,*N''*-pentamethyldiethylenetriamine (PMDETA) (99%), dry tetrahydrofuran (THF). 1,2-hexadecanediol (97%), oleic acid (90%), oleylamine (>70%), and polyethylenimine (anhydrous, average *M*w ca. 25,000) were purchased from Aldrich. Iron(III) acetylacetonate was purchased from Strem Chemicals, Inc. (3-bromopropyl)trichlorosilane was purchased from Gelest. All other reagent grade chemicals were used as is without further purification.

4.2.2 Sample Preparation

Two distinct methods were used for the preparation and silica-coating of Fe_3O_4 nanoparticles to determine the ideal procedure for the targeted biomedical application. These methods include the traditional coprecipitation of Fe^{2+}/Fe^{3+} salts and thermal decomposition. In general, the resulting Fe_3O_4 particles were also coated with silica by two different approaches. The first approach involved the well-established Stöber method, which consist of hydrolysis and polycondensation of tetraethoxysilane under alkaline conditions in ethanol. The second approach is based on microemulsion synthesis, where micelles (or reverse micelles) are used as nanoreactors to control the particles size and silica coating of the Fe_3O_4 nanoparticles. The surface modifications for each set of particles were the same.

4.2.3 Synthesis of Fe_3O_4 Nanoparticles

4.2.3.1 Coprecipitation Method

To prepare the Fe_3O_4 nanoparticles, ammonium hydroxide was added to a solution of $FeCl_3 \cdot 6H_2O$ and $FeCl_2 \cdot 4H_2O$ at a molar ratio of 2:1. In a 500 mL 3-neck round-bottom flask, 7.05 g of $FeCl_3 \cdot 6H_2O$ and 2.58 g of $FeCl_2 \cdot 4H_2O$ were dissolved in 120 mL of degassed deionized water. The round-bottom flask was equipped with a mechanical overhead stirrer, water condenser, and nitrogen inlet. Inside an oil bath, the reaction mixture was stirred vigorously and

heated to 80˚C. A syringe was used to inject 15 mL of NH_4OH to the solution, followed by 30 minutes of further heating. Next, 50 mL of 0.3 M trisodium citrate was added and the temperature was increased to 90 ˚C. After an additional 90 min of stirring, the solution was allowed to cool to room temperature and the Fe_3O_4 nanoparticles were precipitated in a large amount of acetone. Precipitation of the particles in acetone was repeated twice, and then a strong permanent magnet was used to recover the particles. The recovered Fe_3O_4 nanoparticles were washed with degassed deionized H_2O several times. Lastly, the particles were dialyzed using a 12-14 KD molecular weight cutoff membrane inside of degassed deionized H_2O.

4.2.3.2 Thermal Decomposition Method

A mixture of $Fe(acac)_3$ (2 mmol), 1,2-hexadecanediol (10 mmol), oleic acid (6 mmol), oleylamine (6 mmol), and phenyl ether (20 mL) was prepared and magnetically stirred under argon. This solution was heated to 200 ℃ for 2 h, followed by reflux (~260 °C) for 1 h. The resulting black mixture was allowed to cool to room temperature. While under ambient conditions, ethanol (40 mL) was added to the reaction mixture, forming a black precipitate which was separated via centrifugation. The precipitate was dissolved in a mixture of hexane, oleic acid (0.05 mL), and oleylamine (0.05 mL). Next, centrifugation (6000 rpm, 10 min) was used for removal of any non-dispersed material. Lastly, the product was precipitated with ethanol, centrifuged (6000 rpm, 10 min) to remove the supernatant, and then redispersed in hexane. A black-brown hexane dispersion of Fe_3O_4 nanoparticles was obtained.

4.2.4 Preparation of Silica-Coated Fe_3O_4 Nanoparticles (Fe_3O_4@SiO_2)

4.2.4.1 Stöber Method

The Fe_3O_4@SiO_2 nanoparticles were prepared from the synthesized Fe_3O_4 nanoparticles. In a 500 mL 3-neck round-bottom flask, a solution of Fe_3O_4 nanoparticles (5 g, 3.2 wt%) was added.

To this solution, H_2O (40 mL) and ethanol (160 mL) were also added under nitrogen and was then vigorously stirred. Aqueous ammonium hydroxide (30 wt%, 0.5 mL) and 0.5 mL of tetraethyl orthosilicate (TEOS) were injected into the flask and the reaction was allowed to continue overnight. The final product was collected via magnetic extraction and was cleaned by centrifugation using H_2O and EtOH.

4.2.4.2 Microemulsion Method

As an alternative procedure, $Fe_3O_4@SiO_2$ nanoparticles were prepared using a microemulsion synthesis. Polyoxyethylene(5)nonylphenyl ether (Igepal CO-520, 1 mmol) was added to cyclohexane (9 mL), and was probe sonicated for 10 min. A dispersion of oleic acid-stabilized Fe_3O_4 nanoparticles in cyclohexane (1 mg/mL) was added to a 3-neck round-bottom flask, along with the Igepal CO-520 mixture. An overhead stirrer was used to stir this brown transparent mixture for 2 h, followed by the addition of ammonium hydroxide (35%, 80 μL). After adding tetraethyl orthosilicate (60 μL), the reaction was allowed to continue for 48 h at room temperature. The resulting $Fe_3O_4@SiO_2$ nanoparticles were collected by magnetic separation and centrifugation after the surfactant was removed with methanol. The particles were then washed for times with ethanol. Lastly, the prepared particles were re-dispersed in ethanol.

4.2.5 Azido-Functionalized Silica-Coated Fe_3O_4 Nanoparticles (Azido- $Fe_3O_4@SiO_2$)

A dispersion of $Fe_3O_4@SiO_2$ nanoparticles (0.25 g) in toluene was bromofunctionalized using (3-bromopropyl)trichlorosilane. The nanoparticles were then isolated with a strong permanent magnet and redispersed in toluene twice. Following a third isolation, the particles were redispersed in DMF, then NaN_3 (0.16 g) and tetrabutylammonium iodide (4.2 mg) were added to the solution. This mixture was heated to 80 ˚C and was allowed 24 h to react while stirring. With a strong permanent magnet, the azido-$Fe_3O_4@SiO_2$ nanoparticles were isolated and redispersed in ethanol.

4.2.6 Synthesis of *N*-Carboxyanhydride (NCA)

Using the procedure of Daly and Poché[19], N_ε-carbobenzyloxy-L-lysine *N*-carboxyanhydride (CBL-NCA) was prepared. In general, 5 g of the respective protected amino acid was dissolved in 150 mL of anhydrous ethyl acetate inside a flame-dried 250 mL round-bottom flask. The flask included a magnetic stir bar, condenser, and nitrogen bubbler in-line to maintain an inert atmosphere. Using a silicon oil bath, the reaction flask was heated to 60 ˚C and then 1.26 g (0.00425 mol) of triphosgene was added. This mixture was allowed 1 h to stir, where completion was indicated by the solution exhibiting a clear appearance. The clear solution was concentrated to 1/3 of its volume and a white precipitate was formed after adding 100 mL of cold hexane. To promote crystallization, the reaction flask was placed in the freezer overnight. The final product was filtered via vacuum filtration and washed with cold hexane. Note: *Triphosgene is toxic and should be handled and weighed inside a hood. In addition, the reaction should be conducted in a hood, where the HCl/triphosgene from the nitrogen bubbler is allowed to pass through a solution of ammonium hydroxide.* All filtrations were done inside a glovebag, under nitrogen. Final yield of 85%.

4.2.7 Synthesis of Polypeptides

4.2.7.1 Alkyne-Terminated Poly(N_ε-carbobenzyloxy-L-lysine) (Alkyne-PCBL)

With propargylamine as an initiator, the ring-opening polymerization of N_ε-carbobenzyloxy-L-lysine *N*-carboxyanhydride (CBL-NCA) yielded alkyne-terminated poly(N_ε-carbobenzyloxy-L-lysine) (Alkyne-PCBL). CBL-NCA (1.7 g, 0.0055 mol) was weighed inside a flame-dried 50 mL round-bottom flask, which was capped with a rubber septum connected to an argon line with a syringe needle. Dry THF (25 mL) was injected into the reaction mixture, and the solution was stirred and heated to 30 ˚C. After propargylamine (38 μL, 0.0221 mol) in dichloromethane was added via injection, the reaction was continued for 3 days. Once complete, the solution was

concentrated and the polypeptides were precipitated in acetone. The final product was filtered and dried in a vacuum oven, with a yield of 75%.

4.2.8 Porphyrin Synthesis

4.2.8.1 Porphyrin 4-2

A solution composed of tetra(4-hydroxyphenyl)porphyrin **4-1 (**0.17 g, 0.25 mmol) and Cs_2CO_3 (0.650 g, 2 mmol) in 40 mL of anhydrous DMSO was prepared and heated to 50 ˚C in an oil bath. While under argon, the solution was stirred for 1 h with a magnetic stir bar. Next, *tert*-butyl bromoacetate (38.4 μL, 0.26 mmol) was added to the solution and was refluxed overnight. The mixture was allowed to cool to room temperature and was then poured into 200 mL of brine. After purifying the product by extraction with ethyl acetate, it was dried over anhydrous Na_2SO_4. The solvent was evaporated under vacuum and the target compound was isolated via flash chromatography on silica gel column, using ethyl acetate/chloroform (50:50) as the eluent. The product was dried under vacuum, with a final yield of 30%. MALDI-TOF-MS for $C_{46}H_{32}N_4O_6$, calculated 736.77 [$M+H^+$].

4.2.8.2 Porphyrin 4-4

Porphyrin **4-3** (0.1 g, 0.159 mmol) was reacted with a solution of glutaric anhydride (0.54 g, 0.477 mmol) in 2 mL of dry DMF for 48 h at room temperature. Upon completion, distilled water (10 mL) was added 10 mL of EtOAc. After separation of the two phases, the organic phase was washed with distilled water (3 × 10 mL) and dried with anhydrous Na_2SO_4. The prepared tert-butyl protected porphyrin (0.120 g, 0.102 mmol) was dissolved in a 4 mL mixture composed of glacial acetic acid and ethanol (3:1). Pd/C (10%, 0.12 mg) was added after the solution was flushed with H_2 using a balloon. The flushing process was repeated while the solution stirred at room temperature for 4 h. To remove the Pd catalyst, the reaction mixture was filtered through

Celite. The resulting solid residue was washed with a mixture of chloroform and methanol (2:1). Under vacuum, the filtrate was evaporated and the remaining residue was dissolved in chloroform (50 mL), and then washed with distilled H_2O (3×50 mL) to remove any traces of acid. Lastly, the organic phase was dried over anhydrous Na_2SO_4, and the solvent was evaporated under vacuum. The target porphyrin was purified via flash chromatography on a silica gel using a chloroform/methanol (9:1) solvent system for elution. ^{1}H-NMR (d6-DMSO, 400 MHz): δ 8.8 (s, 7H), 8.43 (s, 7H), 7.71 (S, 2H), 7.60 (s, 10H), 2.63 (t, 4H, CH_2), 2.21 (p, 2H), -2.79 (s, 2H). ^{13}C-NMR (d6-DMSO, 62.5 MHz): δ171.93, 168.38, 156.13, 141.22, 138.42, 136.28, 134.69, 134.22, 131.41, 131.01, 128.09, 127.10, 119.99, 117.94, 70.69, 68.30. MALDI-TOF MS *m*/*z* 744.33 ($M + H^+$), calculated for $C_{49}H_{38}N_5O_3$ 744.2896.

The above compound was dissolved in DCM (5 ml), and $Zn(OAc)_2$ (5 ml) was added and stirred at room temperature for 24 hours. The mixture is poured into 100 ml water and extracted with ethyl acetate. The organic layer is evaporated to give quantitative yield 96%. MALDI-TOF MS *m*/*z* 805.252 [$M + H^+$], calculated for $C_{49}H_{35}N_5O_3Zn$ 805.203.

4.2.8.3 Porphyrin 4-6

A solution of commercially available tetra (4-hyroxyphenyl) porphyrin **4-1** (340 mg, 0.5 mmol) in DMSO (60 ml) was mixed with K_2CO_3 (560 mg, 4 mmol) and the reaction mixture was heated at 50 ˚C for 15 min under argon. Propargyl bromide (0.046 ml, 0.52 mmol) was then added and heating was continued at 50 ˚C overnight. The mixture was allowed to cool to room temperature and was then poured into 200 mL of brine. After purifying the product by extraction with ethyl acetate, it was dried over anhydrous Na_2SO_4. The solvent was evaporated under vacuum and the target compound was isolated via flash chromatography on a silica gel column, using ethyl acetate/dichloromethane (30:70) as the eluent. The product was dried under vacuum,

with a final yield of 32%. ^{1}H-NMR (Acetone-d6, 400 MHz): δ 8.93 (s, 6H, β-H), 8.83 (s, 2H, β-H), 8.02-8.06 (m, 8H), 7.26-7.28 (m, 8H), 4.93 (s, 2H, CH_2), 3.19 (s, 1H, CH), -2.64 (s, 2H, NH). ^{13}C-NMR ($CDCl_3$, 62.5 MHz): δ157.78, 157.49, 150.80, 150.75, 150.53, 136.92, 135.84, 135.66, 134.93, 131.90, 131.83, 131.60, 121.02, 120.94, 120.11, 114.25, 113.83, 113.22, 79.50, 76.80, 56.15, 13.97. MALDI-TOF-MS m/z 717.182 [M+H$^+$] for $C_{47}H_{32}N_4O_4$, calculated 717.251 [M+H$^+$].

To the above compound in acetone (5 ml), saturated $Zn(OAc)_2$/MeOH (5 ml) was added and mixed at room temperature for 24 h. The mixture was poured into water (100 ml) and extracted with ethyl acetate. The organic layer was evaporated to give quantitative yield 98%. ^{1}H-NMR (Acetone-d6, 400 MHz): δ 8.93 (s, 6H, β-H), 8.88 (s, 2H, β-H), 8.11 (d, J= 8.4, 2H), 8.03 (d, J= 8.12, 6H) 7.35 (d, J=8.44,2H), 7.25 (d, J=8.04, 6H), 5.02 (s, 2H, CH_2), 3.21 (s, 1H, CH). MALDI-TOF-MS 778.188 [M] for $C_{47}H_{30}N_4O_4Zn$, calculated 778.168 [M].

4.2.9 General Porphyrin-Polypeptide Conjugation

A solution of Zn-porphyrin (53 mg, 0.0658 mmol) in DMF (0.5 ml) was mixed with DIEA (0.102 ml, 0.0987 mmol) and stirred at room temperature under argon for 30 min. PyBOP (51.36 mg, 0.0987 mmol) was then added and the reaction continued stirring for an additional 30 min. Finally, PCBL-Alkyne (217.14 mg, 0.0658 mmol) was added and was allowed to stir for 4 days.

4.2.10 General Grafting of Alkyne-Moieties to Azido-Functionalized Fe_3O_4@SiO_2 Nanoparticles via Click Reaction

Azido-functionalized Fe_3O_4@SiO_2 (.005 g) was dispersed in dry toluene (2 mL) inside a 3-neck round-bottom flask, which was connected to a condenser and nitrogen inlet. The prepared dispersion was degassed for 10 min, and then a degassed solution of alkyne-terminated Zn-porphyrin moiety (0.1 g) in toluene (2 mL) was added to the mixture. In a different vial, CuBr (0.0092 g) was weighed and dissolved in toluene (2 mL), and was capped with a rubber septum.

PMDETA (0.03 mL) was injected into the CuBr solution with a syringe. After stirring and degassing this solution for 10 min, it was injected into the 3-neck reaction which contained the azido-functionalized Fe_3O_4@SiO_2 composites and alkyne-porphyrin moiety. First, this mixture was heated at 60 ˚C while stirring for 1 h, and then heated at 40 ˚C for 24 h. Once the reaction mixture was cooled to room temperature, the nanocomposite particles were recovered by magnet and centrifugation. To remove any unreacted porphyrins, the particles were redispersed in toluene and recovered three more times. After the final purification, the particles were dispersed in chloroform and extracted with distilled H_2O, then repeated with a solution of the sodium salt of EDTA, and again with H_2O to remove traces of copper. The composites were recovered with a magnet and centrifuged, and redispersed in chloroform three times. TFA was used to remove the zinc from the final Fe_3O_4@SiO_2-*click*-porphyrins, yielding the free-base form.

4.2.11 Characterization Methods

Gel permeation chromatography (GPC) was used to determine the molecular weight of the alkyne-terminated polypeptides. The measurements were conducted using an Agilent 1200 system (Agilent 1200 series solvent degasser, isocratic pump, auto sampler and column heater), which was equipped with three Phenomenex 5 μm, 300 × 7.8 mm guard columns. For detection, a Wyatt DAWN EOS multiangle light scattering (MALS) detector, with a GaAs 30 mW laser (λ = 690 nm), Wyatt ViscoStar viscosity (VISC) detector, and Wyatt Optilab rEX differential refractive index (DRI) detector with a 690 nm light source were used. The eluent was DMF which contained 0.1 M LiBr with a flow rate of 0.5 $mL \cdot min^{-1}$. Data analyses were performed using Astra V 5.3 software (Wyatt). All matrix-assisted laser desorption/ionization-time-of-flight (MALDI-TOF) spectra were recorded on a Bruker PROFLEX III MALDI-TOF mass spectrometer. Fourier transform infrared (FTIR) spectra were collected using a Bruker Tensor 27

FT-IR spectrometer with a Pike Miracle single-bounce attenuated total reflectance (ATR) cell equipped with a ZnSe single crystal. Thermogravimetric analysis (TGA) was conducted using a TA Instruments TGA Q50 under nitrogen flow with a heating rate of 10 ˚C min^{-1}. To monitor the surface composition of the nanoparticles upon chemical modification, a Kratos Analytical Axis 165 X-ray photoelectron spectrometer (XPS) with Al Kα X-ray radiation 1486.6 eV and 90˚ takeoff angle. Particle size distribution analyses were conducted using a custom-built dynamic light scattering (DLS) apparatus, equipped with a Coherent Innova 90 argon (400-800 nm) laser. The device also has a Pacific Precision Instruments (Irvine, California) wide-range photometer/preamplifier/discriminator which drives an ALV pulse shaper, and is responsible for feeding an ALV-5000 digital autocorrelator. The nanoparticles were transferred into clean cells with 0.22 μm Durapore membrane filters (Millipore Co., Billerica, Massachusetts). To control the temperature, a circulating water bath was used at a setting of 25 ˚C. Each sample was measured three times at several scattering angle with durations of 180 s. The apparent hydrodynamic diameter, D_h, was determined by analyses of the averaged data using one-exponential and third-order cumulant algorithms.

4.3 Results and Discussion

4.3.1 Synthesis and Characterization of Fe_3O_4

Magnetite (Fe_3O_4) nanoparticles were prepared by two distinct methods. The first approach involved coprecipitation of ferric chloride ($FeCl_3$) and ferrous chloride ($FeCl_2$) with a molecular ratio of 1:2, respectively, in aqueous solution. Overall, the reaction may be expressed as follows:

$$Fe^{2+} + 2Fe^{3+} + 8\ OH^- \rightarrow Fe_3O_4 + 4H_2O \qquad \text{Equation 4-1}$$

The size of the Fe_3O_4 particles was controlled by varying the concentration and amount of NaOH in the reaction mixture. Due to the inherent agglomeration of the Fe_3O_4 nanoparticles, it was

difficult to accurately determine their average diameter and size distribution using DLS. Figure 4-1 shows a TEM image of these bare particles, depicting the exhibited aggregation. Generally, the coprecipitation method was suitable for mass production of Fe_3O_4 nanoparticles. However, the particles were highly polydispersed in size and shape according to TEM images. These irregularities are attributed to the nucleation and subsequent growth of Fe_3O_4 particles in an uncontrolled manner while in the bulk aqueous phase. Such features make this method unfavorable for the preparation of nanoparticles where size homogeneity and stability are important. An alternative approach was explored to address each of these concerns.

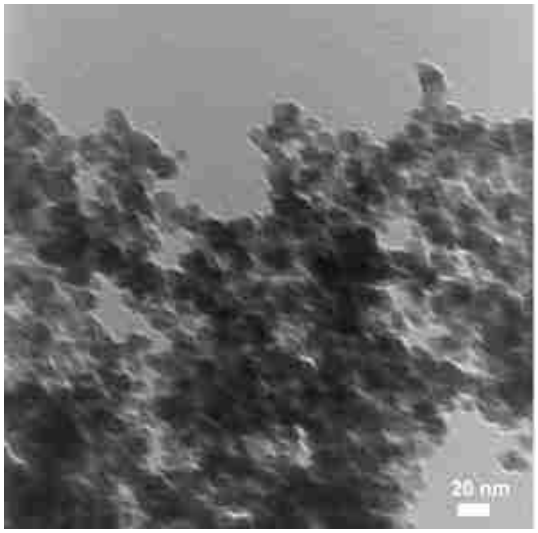

Figure 4-1 TEM image of Fe_3O_4 nanoparticles prepared via the coprecipitation method.

Monodisperse Fe_3O_4 nanoparticles were synthesized using the thermal decomposition method (see Scheme 4-1). The reaction of ferric acetylacetonate precursor, Fe-$(acac)_3$, with surfactants at high temperature produced stable nanoparticles, which were easily separated from reaction byproducts. Phenyl ether was the chosen solvent because of its high boiling point (259 ˚C). In a previous comparative study[20], the use of phenyl ether as the solvent typically resulted in 4 nm Fe_3O_4 nanoparticles, whereas benzyl ether (b.p., 298 °C) led to 6 nm Fe_3O_4. Although this

trend indicates that high reaction temperatures contribute to the production of larger particles, monodispersity is only achieved when the reaction mixture is heated to 200 °C for 2h prior to refluxing. Initiating reflux directly from room temperature broadens the particle size distribution (4-15 nm). This phenomenon suggests the Fe_3O_4 nucleation and nuclei growth process is slow under these reaction conditions.[21]

The reducing agent, 1,2-hexadecanediol, reacted well with the $Fe(acac)_3$ precursor to produce high quality Fe_3O_4 nanocrystals. However, particle quality, as well as the final yield, tends to diminish when long-chain monoalcohols (e.g., stearyl alcohol) are utilized as reductants. The combination of oleic acid and oleylamine was also essential for high yields of particles. The presence of these ligands enhances the solubility of complexes in organic solvents (e.g., hexane and chloroform).[20] In general, oleylamine stabilizes maghemite, γ-Fe_2O_3, nanocrystals via the coordination of $-NH_2$ with Fe^{3+} on the particle surface (see scheme 4-1). However, solely using oleylamine in the reaction provides a low yield of Fe_3O_4 nanoparticles.[20,22] In contrast, the exclusive use of oleic acid in the reaction results in a viscous product that is difficult to purify and characterize.

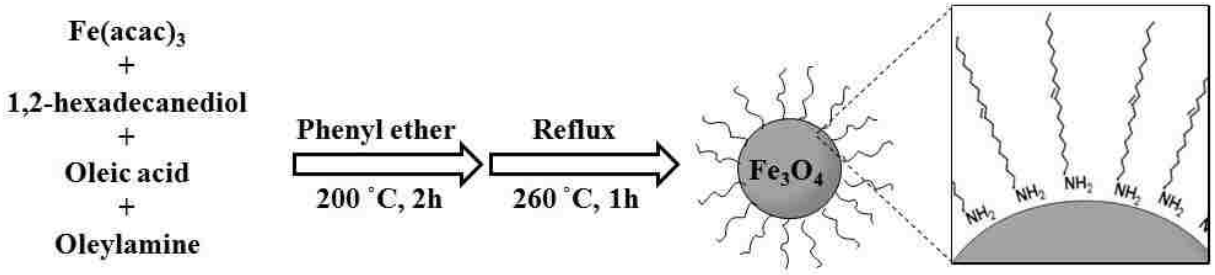

Scheme 4-1 Illustration of the thermal decomposition method.

A TEM image of monodisperse Fe_3O_4 nanoparticles prepared by thermal decomposition is shown in Figure 4-2. Unlike the coprecipitation method, agglomeration was prevented due to the presence of surfactants at the interface. Also, the obtained particles have a narrow size-

distribution and appear in a self-ordered arrangement. According to DLS data, the average diameter of the Fe_3O_4 was found to be 7.8 ±1.3 nm. Magnetic materials of this size are considered to be within the superparamagnetic regime (1-10 nm).

Generally, X-ray diffraction (XRD) is useful for acquiring information about the crystallinity of nanoparticles. Figure 4-3 shows XRD measurements which confirmed the synthesis of magnetite. The XRD spectra of Fe_3O_4 prepared by coprecipitation and thermal decomposition exhibited patterns which were in agreement with those of standard Fe_3O_4 particles. The known standard Fe_3O_4 diffraction are indexed to (220), (311), (400), (422), (511) and (440) planes of a cubic unit cell, corresponding to the reflections of the inverse spinel structure of magnetite (JCPDS card no. 19-0629). It should be noted that the standard XRD patterns of magnetite and maghemite (γ-Fe_2O_3; JCPDS no. 39-1346) are practically identical. Complementary techniques, such as X-ray photoelectron spectroscopy (XPS), were performed to reaffirm the XRD results (see Section 4.3.2).

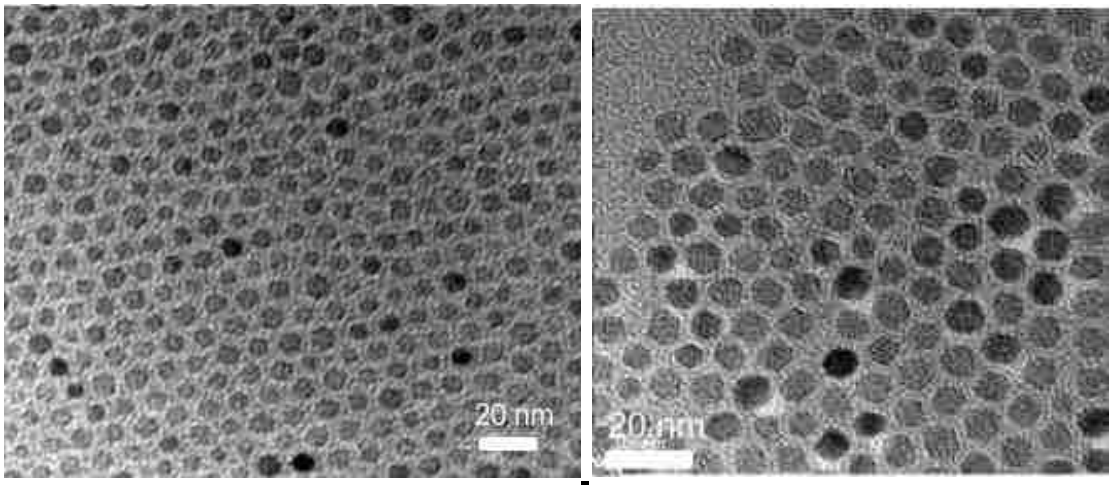

Figure 4-2 TEM images of a monolayer of Fe_3O_4 nanoparticles prepared via the thermal decomposition method.

The superparamagnetism of the Fe_3O_4 nanocrystals was measured using a superconducting quantum interference device (SQUID). Figure 4-4 shows the hysteresis loop of the particles at room temperature. Characteristic of superparamagnetic nanocrystals, the Fe_3O_4 particles exhibited no hysteresis; both, the remanence and coercivity were zero. These properties are pertinent to the "on/off" response of the particles for controlled assembly and transport in the targeted therapeutic application.

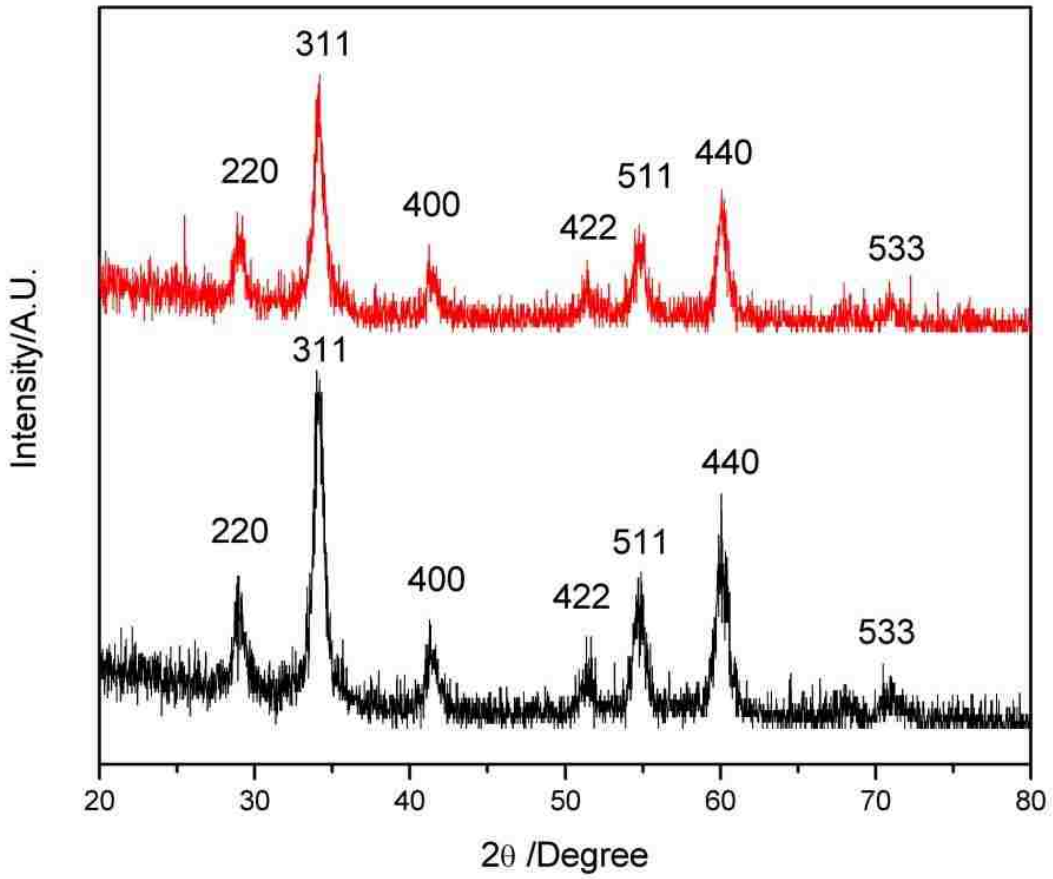

Figure 4-3 XRD pattern of Fe_3O_4 nanoparticles prepared by coprecipitation (—) and thermal decomposition (—).

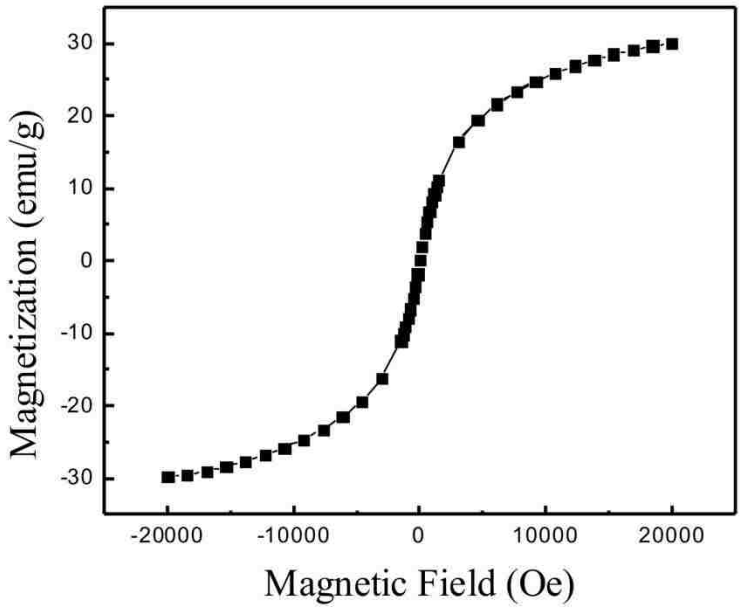

Figure 4-4 Hystersis loop of Fe_3O_4 nanoparticles at room temperature. The magnetization (M) vs applied field (H) of Fe_3O_4 shows no remanence magnetization.

4.3.2 Synthesis and Characterization of Silica-Coated Fe_3O_4 Nanoparticles

Superparamagnetic Fe_3O_4 nanoparticles were coated with a layer of silica by two different strategies. The first approach was the Stöber method, which involved the hydrolysis and polycondensation of tetraethoxysilane (TEOS) under alkaline conditions in ethanol. The second method was based on microemulsion synthesis, where reverse-micelles were exploited as nanoreactors to control the size and monodispersity of the core-shell particles (see Scheme 4-2).

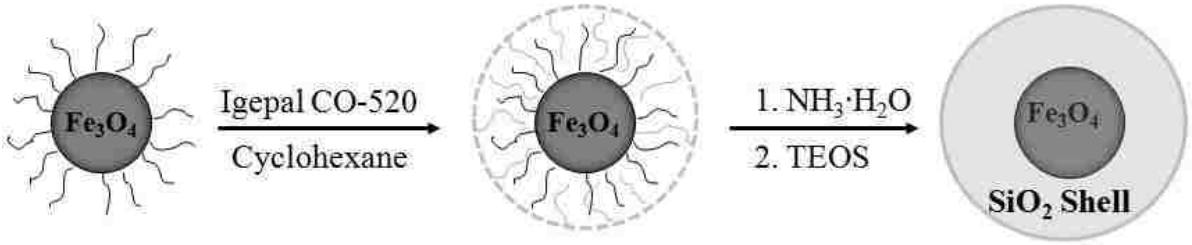

Scheme 4-2 Synthesis of silica-coated Fe_3O_4 nanoparticles via the microemulsion procedure.

These micellar aggregates were composed of surfactants (Igepal CO-520) dispersed in cyclohexane, which was important for connecting oleic acid-stabilized Fe_3O_4 and the aqueous

solution from NH_4OH. Consequently, a shell of water forms along the interface of the Fe_3O_4-Igepal CO-520 composites.[23] In these water regions of the reverse micelles, silica shells were formed on the surfaces of the Fe_3O_4 nanoparticles by hydrolysis and polymerization of TEOS.

Varying the concentration of NH_4OH and TEOS provided control of the silica shell thickness for both methods (i.e., shell thickness decreases when the concentration of these reagents are decreased). In the microemulsion process, the ratio of of Igepal CO-520 to NH_4OH was used to control the micelle size. This feature was essential for limiting the number of embedded Fe_3O_4 particles strictly to one per micelle. However, the probability of encapsulating multiple magnetic cores in a single composite increased as a function of silica shell thickness. Shells that are too thick also tend to dissipate the magnetic properties of the particles. As a simple test for this occurrence, a strong permanent magnet was held next to the prepared $Fe_3O_4@SiO_2$ nanoparticles to observe their response to an external field (see Figure 4-5). The displayed particle behavior indicated the preservation of the magnetic properties.

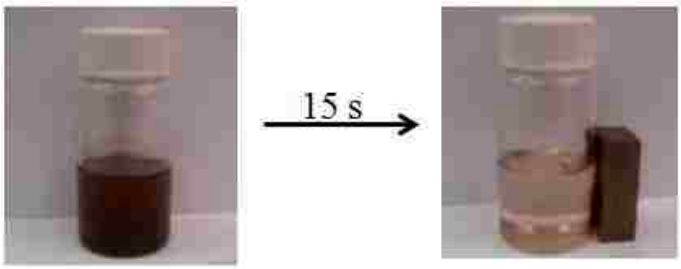

Figure 4-5 Demonstration of the magnetic response of the prepared $Fe_3O_4@SiO_2$ nanocomposites in the absence (left) and presence (right) of a strong permanent magnet.

TEM images of the synthesized $Fe_3O_4@SiO_2$ nanoparticles are shown in Figure 4-6. In comparison to the Stöber method, the microemulsion approach produced smaller and more uniform composites. Figure 4-6a shows a TEM image of Stöber prepared nanoparticles, which is representative of the potential irregularities in particle size and shape when using this approach.

Composites prepared via the microemulsion synthesis had a narrow size distribution (20-25 nm). The average composite diameter was 23 ± 1.8 nm and the silica shell thickness was ~6 nm.

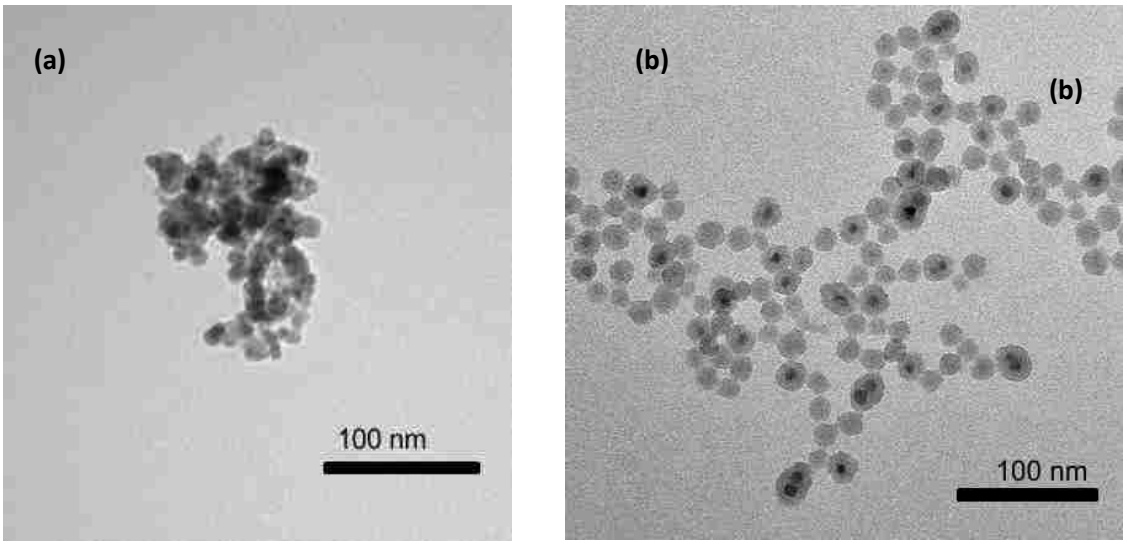

Figure 4-6 TEM of Fe_3O_4@SiO_2 nanoparticles prepared using the (a) Stöber method and (b) microemulsion method.

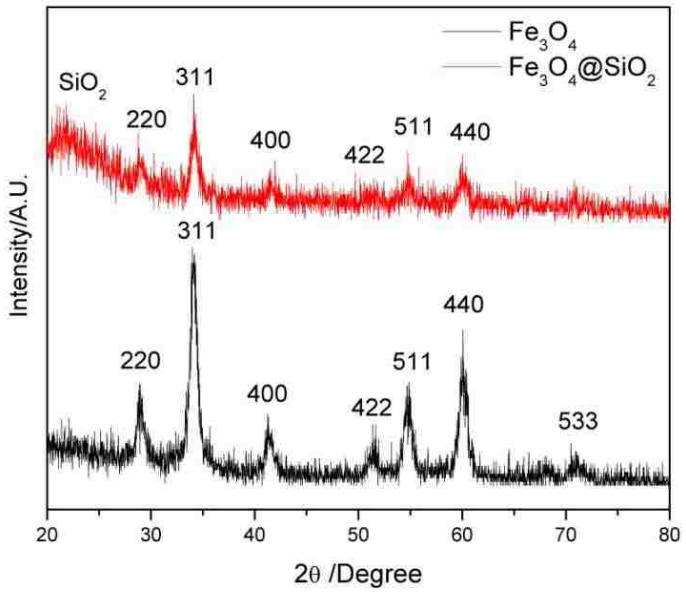

Figure 4-7 XRD spectra of bare Fe_3O_4 (—) and Fe_3O_4@SiO_2 (—) nanoparticles.

Although the silica shell was clearly visible in the TEM images, it was confirmed using XRD. The measured diffraction peaks of the Fe_3O_4@SiO_2 nanocomposites agreed with those of standard Fe_3O_4. However, unlike the XRD pattern of bare Fe_3O_4, the spectrum of Fe_3O_4@SiO_2 has a distinct broad peak that indicates the presence of the silica shell (see Figure 4-7).

4.3.3 Superparamagnetic Azido-Functionalized Fe_3O_4@SiO_2 Nanoparticles

In the preparation of azido-functionalized silica-coated superparamagnetic iron oxide nanoparticles (SPIONs), a series of surface modifications were performed (see Scheme 4-3). Prior to functionalizing the Fe_3O_4@SiO_2 particles with azide groups, the particles were bromo-functionalized via condensation of (3-bromopropyl)trichlorosilane onto the nanocomposites. Bromo-functionalization of the particle surface was confirmed using XPS (see Figure 4-8). In combination with peaks corresponding to silica-coated Fe_3O_4 (i.e., Si 2s, Si 2p, C 1s, O 1s, and Fe2p), the presence of bromine groups was indicated by a Br 3p peak at 188 eV and a less intense Br 3d peak at 70 eV.[24]

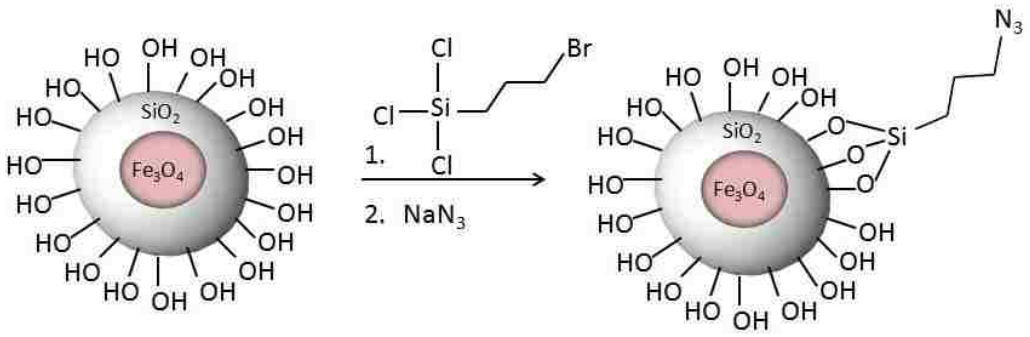

Scheme 4-3 Schematic representation of the preparation and azido-funtionalization of Fe_3O_4@SiO_2 nanoparticles.

The bromo-functionalized nanoparticles were azido-functionalized via nucleophilic substitution of the bromine groups using NaN_3 in DMF. In this reaction, tetrabutylammonium iodide was used as a catalyst. Following the reaction, XPS was used to confirm the presence of azide groups on the particle surface. The disappearance of the Br 3d peak and emergence of a N

1s peak at ~400 eV suggest the bromine/azide substitution occurred (see expanded spectra in Figure 4-8b). However, the Br 3p peak was still slightly visible, which was evidence that perhaps traces of bromine remained. In such a case, the concentration of NaN_3 should be increased to ensure optimal substitution.

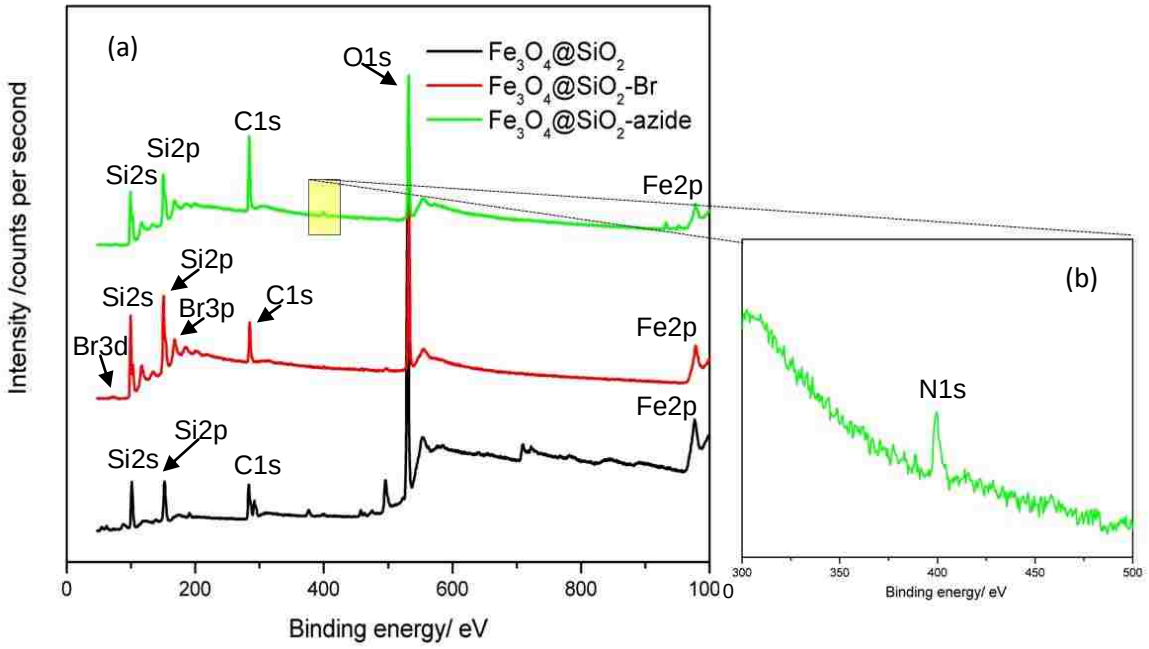

Figure 4-8 XPS survey scans of (a) $Fe_3O_4@SiO_2$ (—), bromo-functionalized $Fe_3O_4@SiO_2$ (—), and azide-functionalized $Fe_3O_4@SiO_2$ (—) nanocomposites, where the (b) expanded region shows the N 1s peak at ~400 eV, indicating the presence of azide groups. Spectra are offset for clarity.

In effort to better resolve the XPS results, additional information was obtained from the FTIR spectra of azide-functionalized $Fe_3O_4@SiO_2$ versus unmodified $Fe_3O_4@SiO_2$ nanoparticles (see Figure 4-9). The characteristic absorption peaks at 441, 585, and 632 cm^{-1} are attributed to the Fe-O structure. For the silica shell, absorption peaks corresponding to Si-O-Si stretching, Si-OH stretching, Si-O bending, and Si-O-Si bending, are displayed at 1095, 945, 802, and 461 cm^{-1}, respectively.[25] The spectrum of the azide-functionalized $Fe_3O_4@SiO_2$ composites showed a

distinct absorption peak at 2100 cm^{-1} corresponding to the presence of azide groups.[24] Further evidence of azide-functionalization was revealed by the disappearance of the Si-OH peak at 945 cm^{-1}.

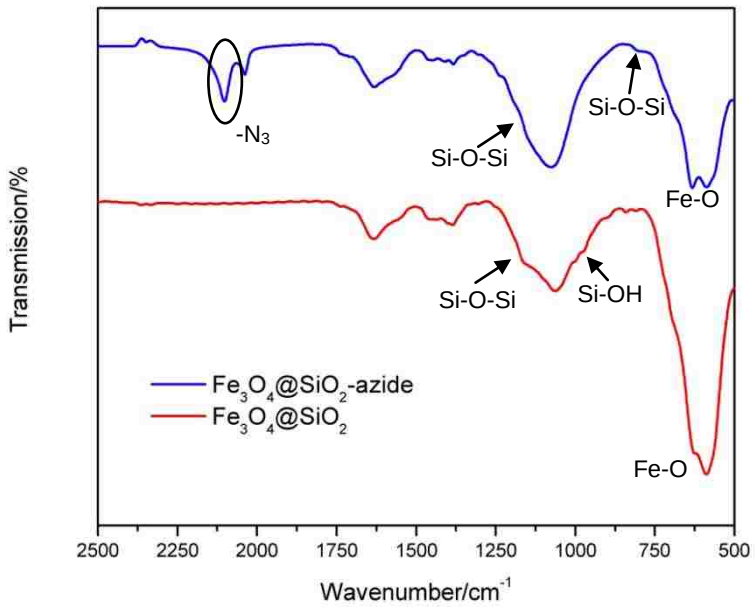

Figure 4-9 FTIR spectra of Fe_3O_4@SiO_2 (—) and Fe_3O_4@SiO_2-azide (—) nanoparticles. Spectra are offset for clarity.

4.3.4 Preparation of Alkyne-Terminated PCBL

Alkyne-terminated PCBL (Alkyne-PCBL) was synthesized by the ring-opening polymerization of ε-carbobenzoxy-L-lysine *N*-carboxyanhydride (CBL-NCA) monomers in anhydrous DCM with propargylamine as the initiator. The CBL-NCA monomers were prepared by the procedure of Daly and Poché[19], which exploits the cyclization of amino acids with triphosgene. To confirm the cyclization occurred, an FTIR spectrum of CBL-NCA was obtained (see Figure 4-10). It shows the characteristic NCA carbonyl peaks of the anhydride at 1786 cm^{-1} and 1857 cm^{-1}, suggesting the target compound was achieved.

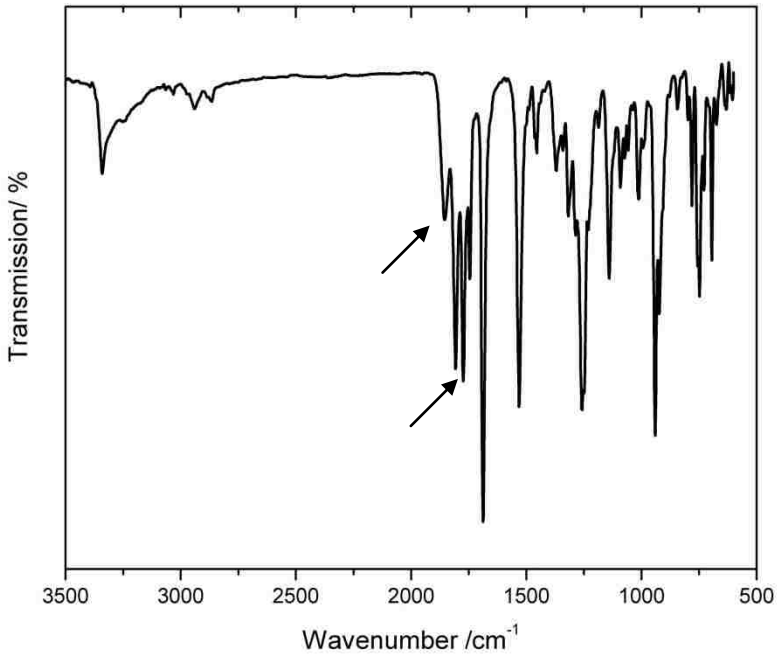

Figure 4-10 FTIR spectrum of CBL-NCA. The arrows indicate the NCA carbonyl peaks of the anhydride at 1786 cm^{-1} and 1857 cm^{-1}.

The primary amine of propargylamine effectively activated the ring-opening of the cyclized CBL-NCA monomers via the mechanism shown in Scheme 4-4. Initially, a degree of polymerization (DP) of 10 was chosen for the reaction. Based on this DP, the expected M_w of the resulting alkyne-PCBL was ~3 kDa. GPC analysis of the PCBL in THF (.1% solution) indicated a bimodal distribution corresponding to weight-average molecular weights of 3.3 kDa and 110 kDa (see Figure 4-11). These data suggest that the expected alkyne-PCBL M_w was obtained, however, a second larger species was also present. A plausible explanation for this behavior takes aggregation of the alkyne-PCBL into account. Another possible suggestion is that some initiators were inactive or quickly led to dead chains.[24] Several attempts were also made in preparing shorter alkyne-terminated PCBL with a DP <10 by decreasing the monomer-to-initiator ratio. In each attempt, the measured M_w exceeded the expected values, which demonstrated the limitations of the polymerization.

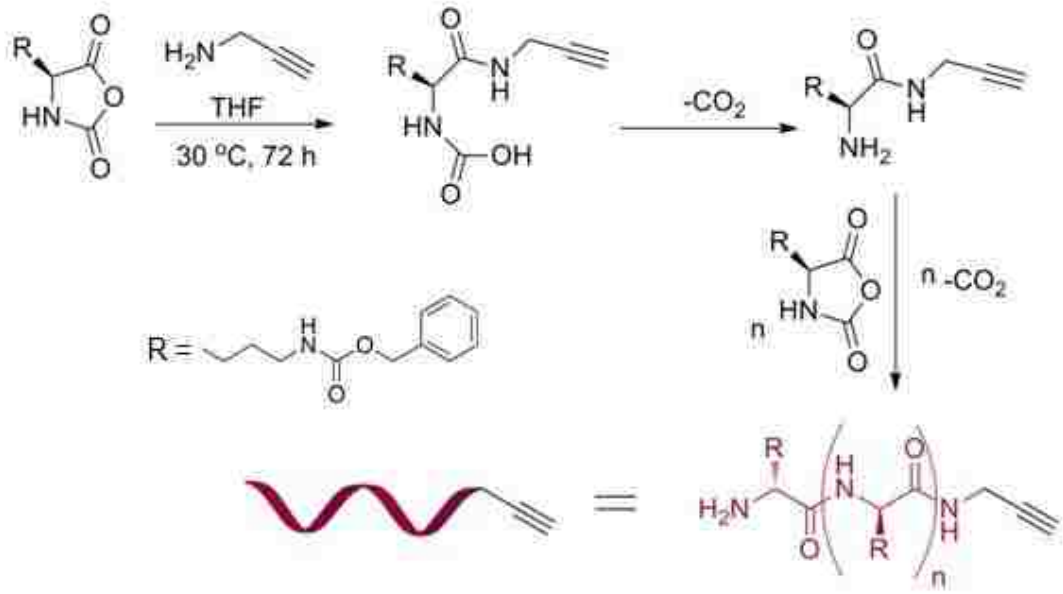

Scheme 4-4 Reaction scheme of the ring-opening polymerization of CBL-NCA to form alkyne-terminated PCBL.

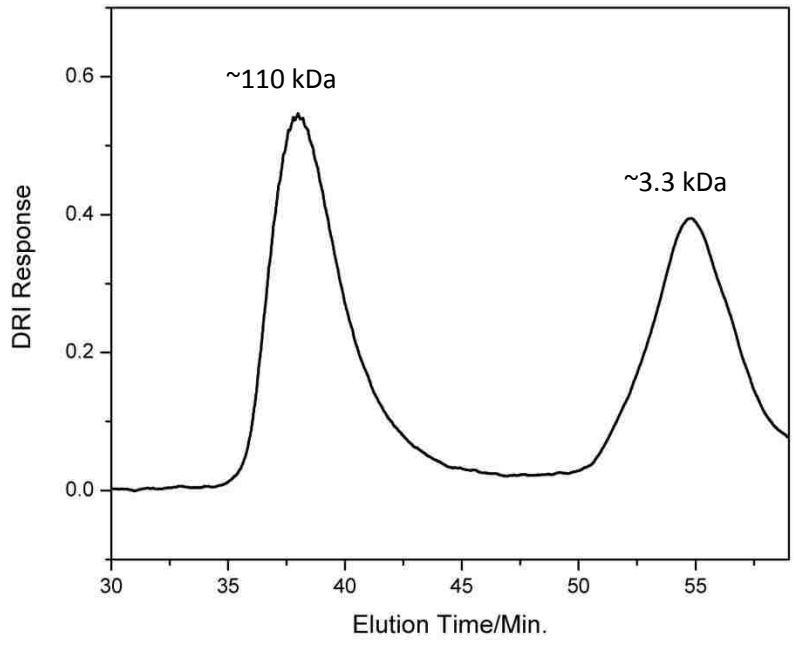

Figure 4-11 GPC chromatogram of alkyne-terminated PCBL [LiBr (0.1 M)/DMF].

4.3.5 Porphyrin Functionalization

The target mono-carboxylic acid porphyrins were designed specifically for covalent linkage to the amine end-group of alkyne-terminated PCBL. These compounds were synthesized using two different approaches. The first approach used tetra(4-hydroxyphenyl)porphyrin **4-1** as the starting material (see Scheme 4-5). One of the four hydroxyl groups of this porphyrin derivative was protected with *tert*-butyl bromoacetate via the Williamson alkylation reaction. Due to the inevitable substitution of multiple hydroxyl groups, it was important to systematically optimize the reaction conditions. The specific ratio of tetra(4-hydroxyphenyl)porphyrin **4-1**, Cs_2CO_3, and *tert*-butyl bromoacetate was 1:2:2, respectively. This mixture was heated to 60 ˚C and was then allowed 24 h to react. After the isolated mono-ether porphyrin was obtained in 30% yield, its benzyl protecting group was removed by catalytic hydrogenation using TFA to give carboxylic acid porphyrin **4-2**. Although the yields from this reaction were relatively low (~30%), the advantage of this method was the commercial availability of the starting compound **4-1**.

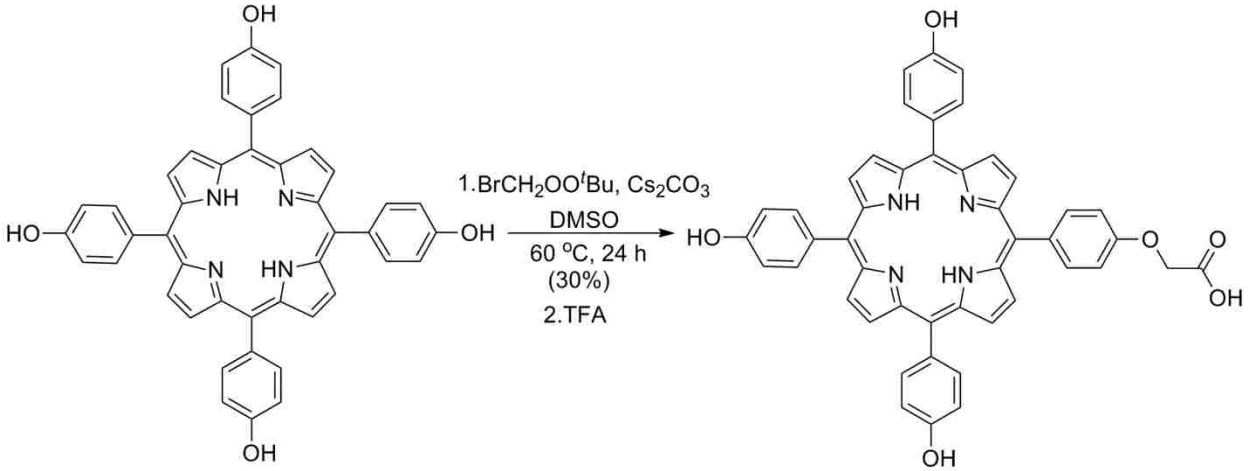

4-1 **4-2**

Scheme 4-5 Reaction conditions for the synthesis of carboxylic acid porphyrin **4-2** from tetra(4-hydroxyphenyl)porphyrin **4-1**.

Scheme 4-6 shows an alternative synthetic route which provided quantitative yields by using mono-amino TPP **4-3** as the starting material. The reaction mechanism converts the amino group

into the carboxylic acid functionality via ring-opening of glutaric anhydride in DMF. The final porphyrin product **4-4** was confirmed by the molecular ion peak at 744.3 in the MALDI-TOF spectrum shown in Figure 4-12. Compared to the previous procedure, the obtained percent yield was a significant improvement. However, the drawbacks of this reaction are that the starting compound **4-3** is not commercially available and its synthesis presents many challenges.

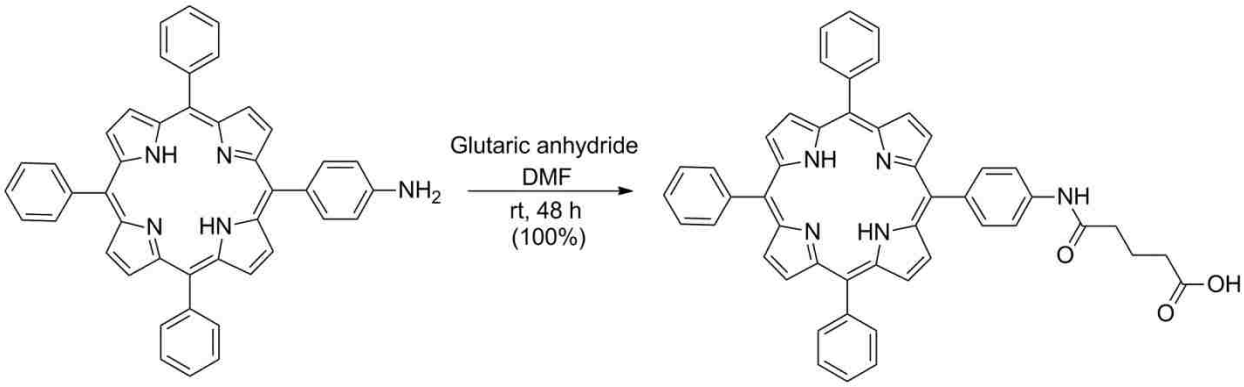

4-3 **4-4**

Scheme 4-6 Reaction conditions for the synthesis of carboxylic acid functionalized porphyrin **4-4** derived from mono-amino TPP **4-3**.

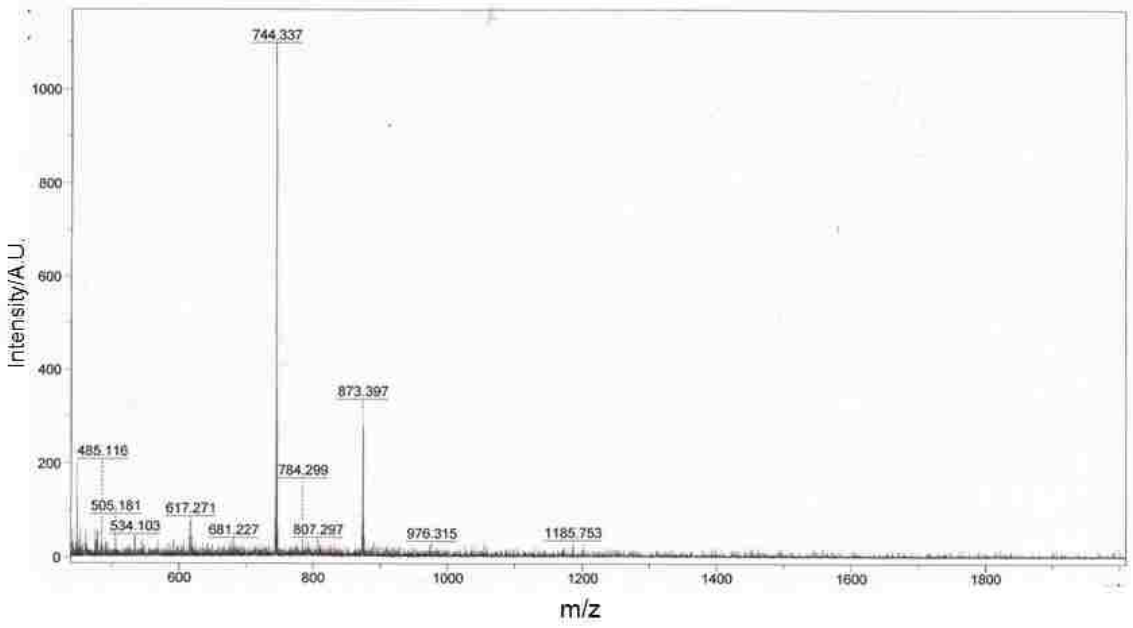

Figure 4-12 MALDI-TOF MS spectrum of carboxylic acid porphyrin **4-4**.

In general, the conjugation of the carboxylic acid-functionalized porphyrins to the of alkyne-PCBL involved the use of peptide-coupling reagents PyBOP and DIEA. The intermediate porphyrin derivative, as the hydroxybenzotriazole ester, was coupled to the free amino terminus of alkyne-PCBL. As a result of this linkage, an amide bond was formed between the porphyrin and polypeptide, as shown in Scheme 4-7.

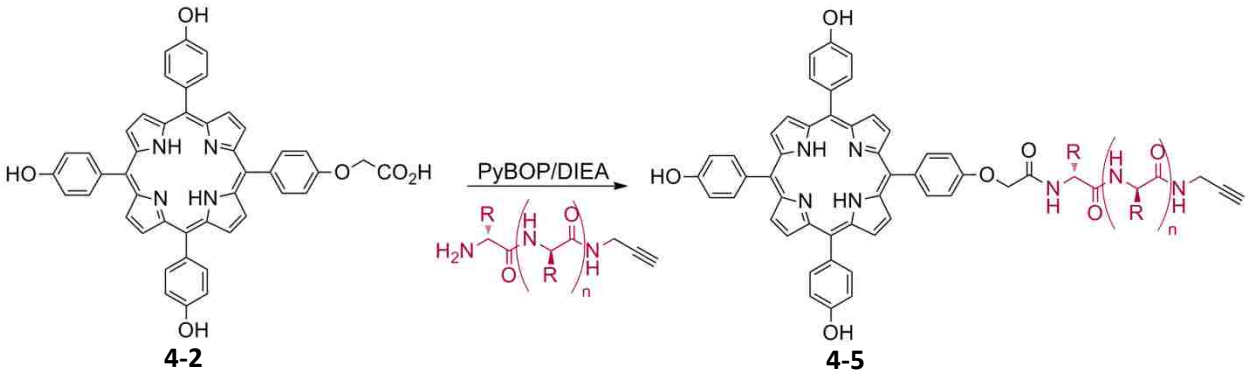

Scheme 4-7 General coupling reaction conditions for the conjugation of alkyne-polypeptides to carboxylic acid porphyrin **4-2**.

The previously discussed porphyrin derivatives were indirectly designed for "click chemistry" reactions via their conjugation to alkyne-terminated polypeptides. However, to avoid the need for an alkyne-functionalized polypeptide, porphyrin **4-6** was directly prepared to bear an alkyne group (see Figure 4-13); this compound was synthesized by N.V.S. Dinesh Bhupathiraju. The reaction involved the mono-alkylation of commercially available porphyrin **4-1** using K_2CO_3 as the base in DMSO, followed by o-alkylation with propargyl bromide. In addition to being a useful tool for a novel approach for preparing superparamagnetic silica-porphyrin nanocomposites, porphyrin **4-6** is also important for elucidating the effects and benefits of porphyrin-polypeptide conjugation.

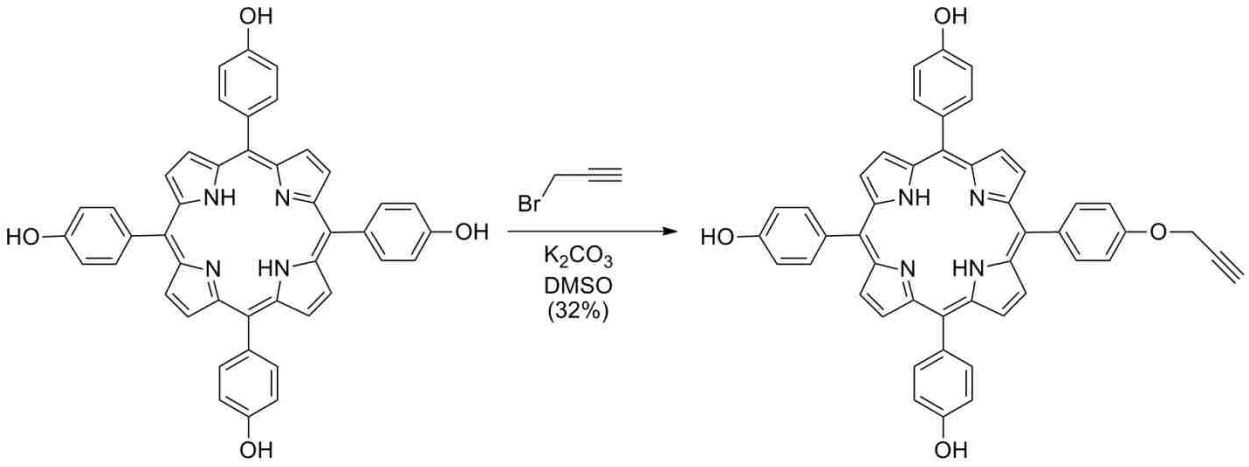

Figure 4-13 Reaction conditions for the synthesis of propargyl-terminated porphyrin **4-6**.

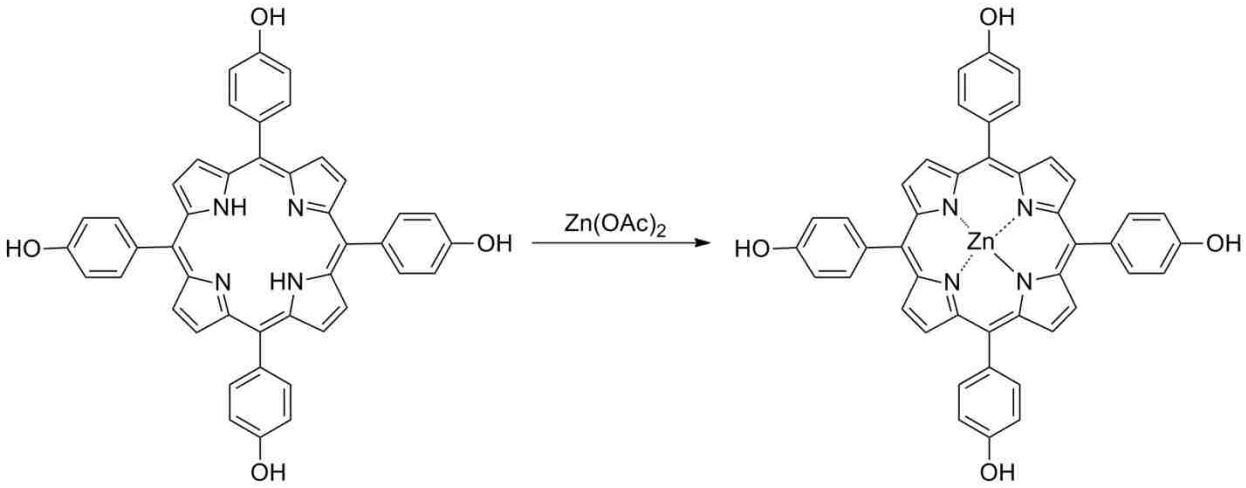

Scheme 4-8 General reaction conditions for zinc insertion into free base porphyrin.

In preparation for the click reaction, it was important to take precautionary steps with each of the previously prepared porphyrins. A former research colleague[26] noticed the failure of copper-catalyzed Huisgen 1,3-dipolar cycloaddition with free base porphyrin derivatives, which was assumed to be due to copper insertion. Inherently, free base porphyrins are capable of binding to metal ions to form metalloporphyrin complexes (e.g., heme and chlorophyll). The preventative strategy involved metalating the porphyrins with zinc prior to performing the alkyne-azide

reaction (see Scheme 4-8). This approach has been shown to enhance the reactivity of the click porphyrin click chemistry and inhibit copper insertion. Upon completion of the azide-alkyne coupling, the zinc ions are easily removed from the porphyrins using TFA.

4.4 Conclusions

Hybrid nanoparticles composed of porphyrins conjugated to polypeptide-coated Fe_3O_4@SiO_2 composites were successfully prepared using a new click chemistry-based approach. The thermal decomposition method produce monodisperse, oleic-acid stabilized Fe_3O_4 nanoparticles, which exhibit superparamagnetic properties. This method can also be extended to the synthesis of other MFe_2O_4 nanoparticles (i.e., M = Co, Ni, Mn, Mg, etc.) by simply adding a different metal acetylacetonate precursor to the reaction mixture. The magnetic particles can be silica-coated in a controlled fashion with the microemulsion synthesis, which produces monodisperse core-shell nanoparticles. The propargylamine-initiated polymerization of CBL-NCA yields alkyne-terminated PCBL and is useful for other amino-acid NCAs. The resulting M_w of the polypeptide can be pre-determined by adjusting the monomer-to-initiator ratio, however, control is loss for DPs <10.

4.5 Future Work and Directions

Attachment of the Zn-porphyrin derivatives to superparamagnetic composites was performed by reacting azido-functionalized Fe_3O_4@SiO_2 with alkyne-conjugated porphyrins using copper-catalyzed Huisgen 1,3-dipolar cycloaddition ("click") (see Scheme 4-9). CuBr/PMDETA constituted the catalyst system, where PMDETA served as a ligand to increase the rate of copper-catalyzed azide-alkyne cycloaddition in organic media.[24] Upon completion, all traces of copper were removed via extraction using an aqueous solution of the sodium salt of EDTA. The resulting Fe_3O_4@SiO_2-*click*-Zn-porphyrin nanoparticles were reacted with TFA to yield

Fe_3O_4@SiO_2-*click*-porphyrin. Characterization techniques, such as FTIR, XPS, TEM, TGA and DLS will be used to confirm that the final product was indeed achieved.

Currently, the coupling of alkyne-PCBL-porphyin to azido-Fe_3O_4@SiO_2 is underway and follows the same procedure as the previously mentioned nanoparticles. In contrast, an additional step must be taken to obtain the target composite. For the purposes of enhancing the water-solubility of the system, PCBL will be debenzylated to achieve hydrophilic poly-L-lysine, which is necessary for the anticipated PDT application.

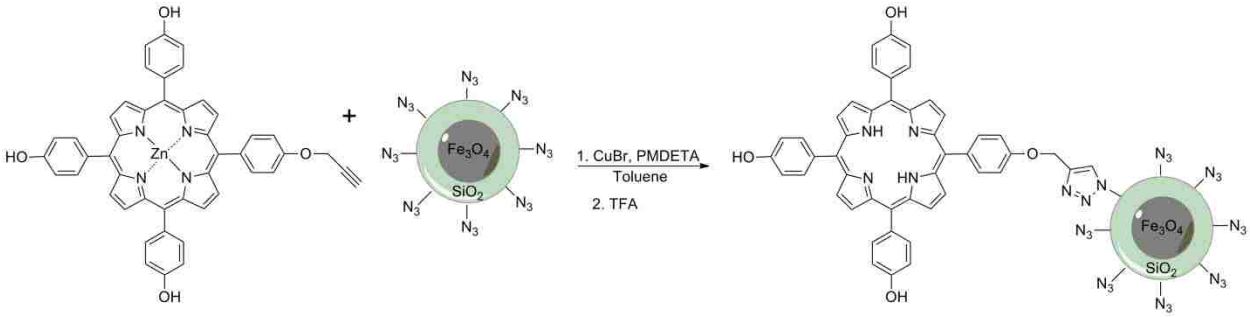

Scheme 4-9 Schematic representation of the click reaction between azido-Fe_3O_4@SiO_2 and alkyne-porphyrin.

A key challenge of PDT involves the delivery of therapeutic amounts of photosensitizers to targeted tumor sites and minimizing their toxic effects on healthy tissue. The use of magnetic particles is a promising strategy for addressing these concerns. However, the hybrid composites presented in this work may introduce a new avenue for enhanced PDT. In addition to controlled transport to tumor sites within the body, this response feature may also afford control over the assembly and disassembly of particles. Such a capability would be useful for minimizing self-quenching, which occurs due to the aggregation of the photosensitizers. Although these hybrid composites possess many promising characteristics, their effectiveness in enhancing PDT remains unknown. A series of *in vitro* biological evaluations will provide insight about the phototoxicity and cellular uptake of the porphyrin-conjugated nanocomposites. Depending on the

outcome of these studies, the necessary particle modifications can be made in route to ideal conditions. For instance, developing a library of polypeptides or peptide sequences may lead to the discovery of nanocomposites with optimal solubility. Beyond the envisioned PDT application, these particles are also feasible candidates for other clinical devices. Simply attaching a different photosensitizer (e.g., phthalocyanine, BODIPY, etc.) may provide new modes for early-stage cancer detection.

4.6 References

(1) Ethirajan, M.; Chen, Y.; Joshi, P.; Pandey, R. K. The role of porphyrin chemistry in tumor imaging and photodynamic therapy. *Chem. Soc. Rev.* **2011**, *40*, 340-362.

(2) Sibrian-Vazquez, M.; Jensen, T. J.; Hammer, R. P.; Vicente, M. G. H. Peptide-Mediated Cell Transport of Water Soluble Porphyrin Conjugates. *J. Med. Chem.* **2006**, *49*, 1364-1372.

(3) Manoharan, M. Oligonucleotide Conjugates as Potential Antisense Drugs with Improved Uptake, Biodistribution, Targeted Delivery, and Mechanism of Action. *Antisense Nucleic Acid Drug Dev.* **2002**, *12*, 103-128.

(4) Staneloudi, C.; Smith, K. A.; Hudson, R.; Malatesti, N.; Savoie, H.; Boyle, R. W.; Greenman, J. Development and characterization of novel photosensitizer : scFv conjugates for use in photodynamic therapy of cancer. *Immunology* **2007**, *120*, 512-517.

(5) Hornyak, G. L.; Tibbals, H. F.; Dutta, J.; Moore, J. J. *Introduction to nanoscience and nanotechnology*; CRC Press: Boca Raton, FL, 2009, 1574.

(6) Roy, I.; Ohulchanskyy, T. Y.; Pudavar, H. E.; Bergey, E. J.; Oseroff, A. R.; Morgan, J.; Dougherty, T. J.; Prasad, P. N. Ceramic-Based Nanoparticles Entrapping Water-Insoluble Photosensitizing Anticancer Drugs: A Novel Drug−Carrier System for Photodynamic Therapy. *J. Am. Chem. Soc.* **2003**, *125*, 7860-7865.

(7) Wieder, M. E.; Hone, D. C.; Cook, M. J.; Handsley, M. M.; Gavrilovic, J.; Russell, D. A. Intracellular photodynamic therapy with photosensitizer-nanoparticle conjugates: cancer therapy using a 'Trojan horse'. *Photochem. Photobiol. Sci.* **2006**, *5*, 727-734.

(8) Bechet, D.; Couleaud, P.; Frochot, C.; Viriot, M.-L.; Guillemin, F.; Barberi-Heyob, M. Nanoparticles as vehicles for delivery of photodynamic therapy agents. *Trends Biotechnol.* **2008**, *26*, 612-621.

(9) Moan, J.; Peng, Q. An outline of the hundred-year history of PDT. *Anticancer Res.* **2003**, *23*, 3591-3600.

(10) Zhang, F.; Wang, C.-C. Fabrication of One-Dimensional Iron Oxide/Silica Nanostructures with High Magnetic Sensitivity by Dipole-Directed Self-Assembly. *J. Phys. Chem. C* **2008**, *112*, 15151-15156.

(11) Liberti, P. A.; Rao, G. C.; Terstappen, L. W. M. M. In *PCT Int. Appl.* ; G01N 1/00 ed.; Organization, W. I. P., Ed.; Immunivest Corporation: USA, 2002; Vol. A1, p 66.

(12) Häfeli, U. O.; Riffle, J. S.; Harris-Shekhawat, L.; Carmichael-Baranauskas, A.; Mark, F.; Dailey, J. P.; Bardenstein, D. Cell Uptake and in Vitro Toxicity of Magnetic Nanoparticles Suitable for Drug Delivery. *Mol. Pharm.* **2009**, *6*, 1417-1428.

(13) Hu, S.-H.; Liu, T.-Y.; Huang, H.-Y.; Liu, D.-M.; Chen, S.-Y. Magnetic-Sensitive Silica Nanospheres for Controlled Drug Release. *Langmuir* **2007**, *24*, 239-244.

(14) Edmondson, S.; Osborne, V. L.; Huck, W. T. S. Polymer brushes via surface-initiated polymerizations. *Chem. Soc. Rev.* **2004**, *33*, 14-22.

(15) Fong, B.; Turksen, S.; Russo, P. S.; Stryjewski, W. Colloidal Crystals of Silica−Homopolypeptide Composite Particles. *Langmuir* **2003**, *20*, 266-269.

(16) Zhong, C. J.; Maye, M. M. Core–Shell Assembled Nanoparticles as Catalysts. *Adv. Mater.* **2001**, *13*, 1507-1511.

(17) Troutier, A.-L.; Ladavière, C. An overview of lipid membrane supported by colloidal particles. *Adv. Colloid Interface Sci.* **2007**, *133*, 1-21.

(18) Liu, C.-X.; Liu, Q.; Guo, C.-C.; Tan, Z. Preparation and characterization of novel magnetic nanocomposite-bonded metalloporphyrins as biomimetic nanocatalysts. *J. Porphyrins Phthalocyanines* **2010**, *14*, 825-831.

(19) Daly, W. H.; Poché, D. The preparation of N-carboxyanhydrides of α-amino acids using bis(trichloromethyl)carbonate. *Tetrahedron Lett.* **1988**, *29*, 5859-5862.

(20) Sun, S.; Zeng, H.; Robinson, D. B.; Raoux, S.; Rice, P. M.; Wang, S. X.; Li, G. Monodisperse MFe2O4 (M = Fe, Co, Mn) Nanoparticles. *J. Am. Chem. Soc.* **2003**, *126*, 273-279.

(21) Watzky, M. A.; Finke, R. G. Transition Metal Nanocluster Formation Kinetic and Mechanistic Studies. A New Mechanism When Hydrogen Is the Reductant: Slow, Continuous Nucleation and Fast Autocatalytic Surface Growth. *J. Am. Chem. Soc.* **1997**, *119*, 10382-10400.

(22) Rajamathi, M.; Ghosh, M.; Seshadri, R. Hydrolysis and amine-capping in a glycol solvent as a route to soluble maghemite [gamma]-Fe2O3 nanoparticles. *Chem. Commun.* **2002**, 1152-1153.

(23) Zhang;, M.; Cushing;, B. L.; O'Connor, C. J. Synthesis and Characterization of Monodisperse Ultra-Thin Silica-Coated Magnetic Nanoparticles. *Nanotechnology* **2008**, *19*, 085601.

(24) Balamurugan, S. S.; Soto-Cantu, E.; Cueto, R.; Russo, P. S. Preparation of Organosoluble Silica−Polypeptide Particles by "Click" Chemistry. *Macromolecules* **2009**, *43*, 62-70.

(25) Lien, Y.-H.; Wu, T.-M. Preparation and characterization of thermosensitive polymers grafted onto silica-coated iron oxide nanoparticles. *J. Colloid Interface Sci.* **2008**, *326*, 517-521.

(26) Hao, E. Syntheses and Evaluation of Porphyrin Derivatives for Applications in Medicine and in Material Science Dissertation, Louisiana State University, 2007.

To view this email as a web page, go here.

Do Not Reply Directly to This Email

To ensure that you continue to receive our emails,
please add rightslink@marketing.copyright.com to your address book.

RightsLink | Copyright Clearance Center

Thank You For Your Order!

Dear Mr. Javoris Hollingsworth,

Thank you for placing your order through Copyright Clearance Center's RightsLink service. John Wiley and Sons has partnered with RightsLink to license its content. This notice is a confirmation that your order was successful.

Your order details and publisher terms and conditions are available by clicking the link below:
http://s100.copyright.com/CustomerAdmin/PLF.jsp?lID=2012101_1350578164615

Order Details
Licensee: Javoris Hollingsworth
License Date: Oct 18, 2012
License Number: 3012010652615
Publication: Journal of Pharmaceutical Sciences
Title: A novel solubility-enhanced curcumin formulation showing stability and maintenance of anticancer activity
Type Of Use: Dissertation/Thesis
Total: 0.00 USD

To access your account, please visit https://myaccount.copyright.com.

Please note: Online payments are charged immediately after order confirmation; invoices are issued daily and are payable immediately upon receipt.

To ensure we are continuously improving our services, please take a moment to complete our customer satisfaction survey.

B.1:v4.2

+1-877-622-5543 / Tel: +1-978-646-2777
customercare@copyright.com
http://www.copyright.com

This email was sent to: **jholl15@lsu.edu**

Please visit Copyright Clearance Center for more information.

This email was sent by Copyright Clearance Center
222 Rosewood Drive Danvers, MA 01923 USA

To view the privacy policy, please go here.

Title:	Phase transitions in the assembly of multivalent signalling proteins
Author:	Pilong Li, Sudeep Banjade, Hui-Chun Cheng, Soyeon Kim, Baoyu Chen, Liang Guo
Publication:	Nature
Publisher:	Nature Publishing Group
Date:	Mar 7, 2012

Author Request

If you are the author of this content (or his/her designated agent) please read the following. If you are not the author of this content, please click the Back button and select an alternative Requestor Type to obtain a quick price or to place an order.

Ownership of copyright in the article remains with the Authors, and provided that, when reproducing the Contribution or extracts from it, the Authors acknowledge first and reference publication in the Journal, the Authors retain the following non-exclusive rights:

a) To reproduce the Contribution in whole or in part in any printed volume (book or thesis) of which they are the author(s).

b) They and any academic institution where they work at the time may reproduce the Contribution for the purpose of course teaching.

c) To reuse figures or tables created by them and contained in the Contribution in other works created by them.

d) To post a copy of the Contribution as accepted for publication after peer review (in Word or Text format) on the Author's own web site, or the Author's institutional repository, or the Author's funding body's archive, six months after publication of the printed or online edition of the Journal, provided that they also link to the Journal article on NPG's web site (eg through the DOI).

NPG encourages the self-archiving of the accepted version of your manuscript in your funding agency's or institution's repository, six months after publication. This policy complements the recently announced policies of the US National Institutes of Health, Wellcome Trust and other research funding bodies around the world. NPG recognises the efforts of funding bodies to increase access to the research they fund, and we strongly encourage authors to participate in such efforts.

Authors wishing to use the published version of their article for promotional use or on a web site must request in the normal way.

If you require further assistance please read NPG's online author reuse guidelines.

For full paper portion: Authors of original research papers published by NPG are encouraged to submit the author's version of the accepted, peer-reviewed manuscript to their relevant funding body's archive, for release six months after publication. In addition, authors are encouraged to archive their version of the manuscript in their institution's repositories (as well as their personal Web sites), also six months after original publication.

v2.0

BACK CLOSE WINDOW

Quick Price Estimate

Permission for this particular request is granted for print and electronic formats, and translations, at no charge. Figures and tables may be modified. Appropriate credit should be given. Please print this page for your records and provide a copy to your publisher. Requests for up to 4 figures require only this record. Five or more figures will generate a printout of additional terms and conditions. Appropriate credit should read: "Reprinted with permission from {COMPLETE REFERENCE CITATION}. Copyright {YEAR} American Chemical Society." Insert appropriate information in place of the capitalized words.

I would like to... reuse in a Thesis/Dissertation

Requestor Type Author (original work)

Portion Full article

Format Print and Electronic

Will you be translating? No

Select your currency USD - $

Quick Price Click Quick Price

This service provides permission for reuse only. If you do not have a copy of the article you are using, you may copy and paste the content and reuse according to the terms of your agreement. Please be advised that obtaining the content you license is a separate transaction not involving Rightslink.

To request permission for a type of use not listed, please contact the publisher directly.

LSU
LOUISIANA STATE UNIVERSITY

Department of Chemistry

November 19, 2012

Gary Bylerly, Ph.D.
Dean of the Graduate School
Louisiana State University
Baton Rouge, LA 70803

Dear Dean Byerly:

I have been asked to comment on the intellectual ownership of certain portions of the Ph.D. dissertation of Javoris Hollingsworth that have appeared already in the open literature as co-authored papers. It is convenient to refer to the relevant sections by the figures. Figures for which primary data were generated and analyzed by Javoris Hollingsworth include: 2-16, 2-17, 2-19, 2-20 and all figures in Chapter 3. Figure 2.18 was not generated by Javoris Hollingsworth but another author; however, its use clarifies the dissertation.

Sincerely,

Paul Sloan

Roy Paul Daniels Professor of Chemistry

242 Choppin Hall • Baton Rouge, LA • 70803 • P 225-578-3361 • F 225-578-3458

VITA

Javoris Hollingsworth was born in Jeffersonville, Georgia, to Sandra and Garry. As a Gates Millennium Scholar, he received his Bachelor of Science in chemistry from Georgia Southern University in May 2007. He went on to pursue graduate school and received his Master of Science degree from Louisiana State University on August 7, 2009. Javoris will graduate with the degree of Doctor of Philosophy in chemistry from Louisiana State University in December 2012.